Anal. Methods Environ. Chem. J. 6 (4) (2023) 5-18

AMECJ

Research Article, Issue 4
Analytical Methods in Environmental Chemistry Journal
Journal home page: www.amecj.com/ir

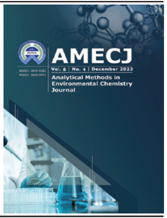

Surface-engineered TiO_2 nanoparticles incorporated Chitosan polymer membrane for seawater desalination: Fabrication, characterization, and performance evaluation

Muhammad Nurdin [a,*], **Mike Delvinasari** [a], **La Ode Ahmad** [a], **Maulidiyah Maulidiyah** [a], **Dwiprayogo Wibowo**[b,c], **Faizal Mustapa** [d], **Amir Mahmud** [e], **Muhammad Idris** [f], **and Muh. Ramli** [h]

[a] *Department of Chemistry, Faculty of Mathematics and Natural Sciences, Universitas Halu Oleo, Kendari 93231, Southeast Sulawesi, Indonesia.*
[b] *Department of Environmental Science, School of Environmental Science, Universitas Indonesia, Jakarta 10430, Indonesia.*
[c] *Department of Environmental Engineering, Faculty of Engineering, Universitas Muhammadiyah Kendari, Kendari 93231, Southeast Sulawesi, Indonesia.*
[d] *Department of Marine Sciences, Institut Teknologi dan Bisnis Muhammadiyah Kolaka, Kolaka 93511, Southeast Sulawesi, Indonesia.*
[e] *Department of Fishery Resources, Faculty of Marine, Universitas Muhammadiyah Kendari, Kendari 93231, Southeast Sulawesi, Indonesia.*
[f] *Department of Agriculture Sciences, Faculty of Agriculture, Universitas Halu Oleo, Kendari 93231, Southeast Sulawesi, Indonesia.*
[h] *Department of Marine Sciences, Faculty of Marine, Universitas Halu Oleo, Kendari 93231,Southeast Sulawesi, Indonesia.*

ARTICLE INFO:

Received 17 Jul 2023
Revised form 23 Sep 2023
Accepted 10 Nov 2023
Available online 28 Dec 2023

Keywords:
Desalination,
Membrane,
TiO_2,
Polymer structure,
Reverse Osmosis,
Seawater,

ABSTRACT

The effect of surface coating over titanium dioxide nanoparticles (TiO_2-NPs) incorporated with chitosan (TiO_2-NPs/chitosan) was evaluated as a reverse osmosis membrane (RO) for enhanced performance on seawater desalination. The impact of surface coating on the chitosan membrane performance in seawater reverse osmosis (SWRO) was investigated by altering the mass of TiO_2-NPs (0.25 g and 0.5 g) used for the surface coating RO membrane. TiO_2-NPs were applied to the membranes using a surface coating technique and dried to create a sturdy polymer structure. The characteristic of fabricated membranes shows the function group reflects on organic compounds from /chitosan membranes polymer (–OH, -CH, C=O, C-O-C, $-CH_3$, C-O, and NH_2). In addition, TiO_2-NPs are expressed in the wavenumber range of 850-500 cm^{-1}, which characterizes the presence of Ti-O-Ti bonds. Morphological and crystal analyses of TiO_2-NPs incorporated in chitosan membrane show significantly smaller pores formed because TiO_2-NPs are essential in the high permeability performance under the amorphous phase structure. Also, the high performance of fabricated membranes was evaluated against water flux and salt. Adding TiO_2-NPs can decrease the water flux value by 23 L m^{-2} h^{-1} and increase salt rejection by 52.94%. In optimized pH, the seawater desalination had efficient recovery.

1. Introduction

Indonesia's marine waters cover 70% of its total land area, making it an excellent opportunity to increase the utilization of seawater as raw water as a source of clean water that can be used to meet the needs of the people in Indonesia [1, 2]. Therefore, seawater treatment is needed to remove or reduce its salt content using RO desalination techniques to become clean water. Pure water is a vital element

---

*Corresponding Author: Muhammad Nurdin
Email: mnurdin06@gmail.com
https://doi.org/10.24200/amecj.v6.i04.246

within the ecosystem, playing a crucial role in the advancement and well-being of humans and various other forms of life [3,4]. The increase in population has led to a situation where not every segment of society can access uncontaminated water. [5]. As a result, many people utilize groundwater and river water for domestic purposes, even though the water is not necessarily suitable for consumption [6]. However, even though the potential availability of water is relatively abundant, people often experience difficulties accessing and fulfilling their water needs for daily life. These problems have led to a lot of research on seawater purification processes. One of the most widely used methods is using semipermeable membranes in RO desalination, which separates low molecular weight solutes such as inorganic salts or small organic molecules such as glucose and sucrose from the solution [7]. RO membranes are widely utilized in various filtration processes, such as groundwater filtration, seawater, and brackish water desalination [8]. The RO process requires membranes to filter out salt molecules to produce ready-to-use fresh water [9]. Transporting specific ions and removing different ions use porous media or membranes. These semi-porous membranes serve as barriers that divide molecules by their respective sizes in a solution. Among the various methods involving membranes for separation, there's the ultrafiltration technique, which relies on pressure differentials for the separation process. The elements isolated within a liquid are contingent on the size and composition of the dissolved substances. [10,11]. Ultrafiltration membranes are principally used to retain colloids and macromolecules but pass salt particles. Separation using membranes was chosen due to its simple, energy-efficient, and environmentally friendly process. Ultrafiltration membranes are usually made of polymeric materials; one of the most commonly used is cellulose acetate (CA) compound [12,13]. RO membranes can be made from various materials; one uses CA compound, which has advantages as an easy-to-produce and renewable raw material source. The disadvantages of the CA membrane are that it is susceptible to acidic and base solutions and is easy for natural microbes [14,15]. The selection of polymers as membrane materials is based on structural factors that will affect the intrinsic properties of the polymer, namely perm selectivity [16]. However, it seems that the CA compound has a full role in the basic ingredients of polymer membrane formation. It dissolves easily with acetone solution and has high capabilities in the ultrafiltration process and high selectivity to filter small materials [17]. The CA compound cannot stand alone as a polymer membrane component; it requires a reinforcing additive compound to improve the membrane's resistant characteristics under stressed conditions. In addition, the function of additive compounds has a role in influencing the formation of membrane morphology, both physicochemical to produce high-performance material properties. PEG is one of the organic compound additives that can reliably improve polymer membrane properties such as surface porosity and membrane pore distribution [18,19]. In some studies, adding PEG as an additive improves membrane performance, like enlarging membrane pores while maintaining membrane resistance to external factors. Besides, the basic membrane organic using CA and PEG is a potential material when combined with chitosan [20]. It has an excellent ability as a coagulant material because it contains many amine groups ($-NH_2$) that are beneficial in the polymetric system of membrane manufacturing. The presence of amine and hydroxyl groups in chitosan makes it have polycationic properties to increase the coagulant in membrane formation, thus strengthening membrane stiffness and high durability in water treatment [21]. These groups can be evaluated with instruments such as Fourier-transform infrared spectroscopy (FTIR) to identify the infrared spectrum of the absorption or emission of the synthesized RO membrane. This characterizes the chemical groups that play a role in membrane formation and influence the adsorption performance. Amine groups in the membrane play a role in various adsorption reaction mechanisms with metal ions. In addition, the amine groups on chitosan are easily modified to improve the adsorption ability and sorbent to handle metal ions in wastewater. In addition, the synthesized membrane observed the crystallinity and morphology to describe the properties of the membranes analyzed using XRD and SEM instrumentation. They are commonly used in material analysis to observe the porosity and stiffness of the membrane.

In this study, we varied the addition of TiO_2 material as a photocatalyst and antifouling agent because it is believed to be a bioceramic material that is resistant in various conditions with non-toxic, antimicrobial, and environmentally friendly properties, making it safe to use as a base material for making membranes with high strength [22,23]. Amazingly, it is widely used as a water purifier under photocatalyst performance for demineralizing organic, inorganic, and microorganisms dissolved in wastewater. In some of our recent research, TiO_2 is applied as an antibacterial material in inhibiting bacterial growth [24], a photocatalyst material for treating organic pollutants in wastewater, and an electrochemical sensor for detecting organic pollution in wastewater because it has high photoactivity and chemical stability, making it resistant to photo corrosion under neutral solution conditions [25,26]. In addition, it also has redox properties that can oxidize organic pollutants and reduce the number of metal ions in water. This study discovered the unique effect of chitosan semipermeable membrane incorporating TiO_2-NPs. The mass variation of TiO_2 was shown to significantly influence the characterization and performance test of the fabricated membranes under RO desalination. The seawater observed comes from the Southeast Sulawesi Province, Indonesia, which has a good sea salt level, and the surrounding community still has difficulty obtaining clean water for daily use.

2. Material and Methods

2.1. Chemicals and materials

Cellulose acetate (CA, purity, 99%), Polyethylene glycol (PEG 400, purity, 99%), TiO_2 Degussa P25 (Purity: 99%), and 2-Amino-2-deoxy-(1,4)-β-D-glucopyranose, Poly-(1,4-β-D-glucopyranosamine) (chitosan, purity: 70%) were purchased from Sigma-Aldrich. The acetone solution (Purity: 99%) was purchased from Merck & Co., Inc.

2.2. Feed water collection

Seawater samples for testing were collected from Toronipa Beach in Konawe Regency, Southeast Sulawesi Province, Indonesia. This location was chosen due to its popularity as a tourist destination and the ongoing challenges coastal communities face in accessing freshwater [27]. The sampling process was conducted approximately 10 meters from the shoreline. We collected 5 gallons of seawater (equivalent to 5 × 3.78 Liters) and passed it through a filter cloth to eliminate impurities, such as seagrass and sand. The filtered samples were then stored in a sample container at room temperature to maintain their integrity for further laboratory analysis.

2.3. Synthesis of TiO_2-NPs–incorporated Chitosan membranes

In this study, 2 grams of CA and 0.5 grams of PEG were mixed in a 50 mL beaker and followed by adding 2 mL of chitosan and 17 mL of an acetone solvent. The media was stirred constantly at 130°C until homogeneous for 24 h. After obtaining a homogeneous solution, it was printed on a flat glass plate for 15 minutes. The membrane layer dries slightly, followed by TiO_2-NPs colloidal coating according to the coating variation by coating evenly on the membrane surface. The media was allowed to dry for 64 hours in a sterile room. After that, to release the membrane that has dried on the surface of the glass plate, the method is to soak the media in cold water for 15 minutes. The membrane is ready for use in the reverse osmosis method design tool with UV light emission.

2.4. Membrane material characterization

The TiO_2 incorporated in chitosan membranes was characterized to confirm the presence of TiO2 in chitosan membranes. The functional group was confirmed using FTIR spectra (Shimadzu, IR Prestige 21) to identify inorganic materials (Ti-O-Ti). Morphological analysis was also conducted using Scanning Electron Microscopy (SEM) (FEI, Inspect-S50) to observe the porosity of synthesized membranes, and crystallinity was investigated using X-ray diffraction (XRD, PAN anlytical X'Pert PRO) to determine the crystallinity of a material.

2.5. Reverse osmosis test

The synthesized membranes were assessed for their performance in a desalination process utilizing the reverse osmosis (RO) technique. The portable design of the reverse osmosis pilot instrument (Fig. 1) involves introducing feed water into a storage tank, which is then pumped into a pretreatment system incorporating filtering materials such as sand, palm fibre, stone, and charcoal. Subsequently, seawater is directed into a horizontal tank equipped with vertically positioned synthetic membranes and subjected to UV light exposure. Excess water is returned to the pretreatment process, while the remainder passes through the membranes and is collected in a permeate container. The permeate was subsequently tested to evaluate membrane performance parameters, including salt rejection, water flux, pH, and salinity.

3. Results and Discussion

This study aims to overview the effect of the surface coating method on TiO_2-NPs incorporated chitosan membrane. In Figure 1, we modelled desalination technology engineering to observe the performance of TiO_2-NPs-chitosan membrane in reverse osmosis (RO) system. Schematically, the feed water is flowed and passed through a pretreatment material consisting of activated carbon. A pressurized pump passes the feed water from the pretreatment through the membrane with UV light to see the photocatalyst performance of the membrane containing TiO_2-NPs. The membrane fabrication, characterization, and performance tests were identified to determine the well-oriented performance membrane, such as identifying flux and salinity values.

The synthesized membrane has been fabricated with a coating process using TiO_2-NPs of 0.25 g and 0.50 g. The simple membrane fabrication was conducted by inverse technique, in which the mixed solution was evaporated on a glass plate for 64 h. The organic solution also plays an essential role in accelerating the evaporation process to obtain a high permeability and resistance to hydrophilic properties, making it easily soluble in water [27]. The organic solvent (acetone) was chosen in this study because it is environmentally friendly for plastic, pharmaceutical, and paper fabrication. Moreover, acetone can reduce the boiling point so the membranes can quickly be dried. In this study, the fabricated membranes have been printed with a diameter size of 8 cm, which

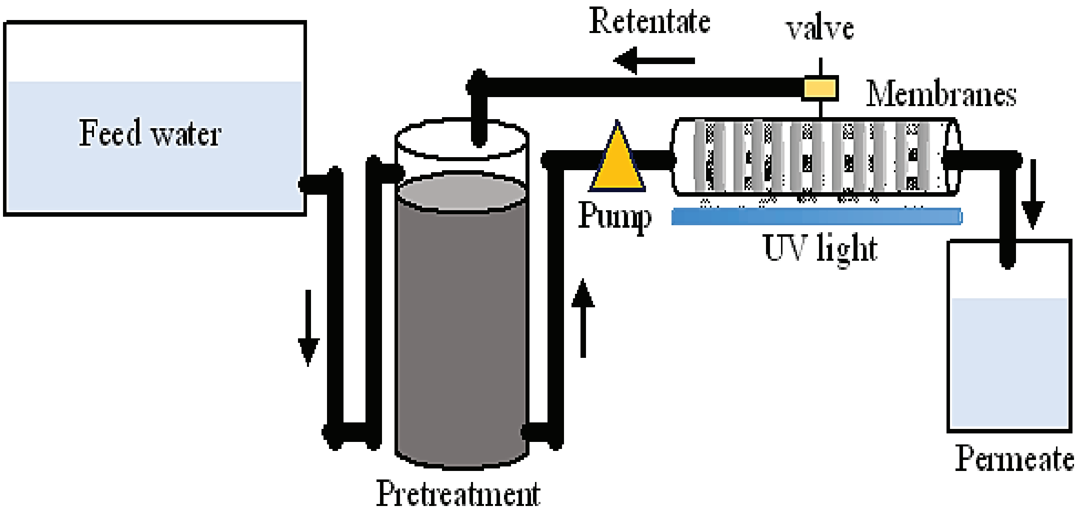

Fig. 1. Schematic of reverse osmosis desalination

helps determine the membrane's performance for water flux. Several studies have also reported that the addition of TiO_2-NPs to organic membranes that have been developed can improve the hydrophilicity and selectivity properties expected for high membrane permeability flux. Herein, we present the fabrication of the chitosan membrane by showing the unique characterization membranes incorporated into TiO_2-NPs using FTIR, SEM, and XRD. They are the basics for material characterization for an overview of a functional group of Ti-O-Ti bonds, morphological analysis of fabricated membranes incorporated TiO_2-NPs and crystallinity. Besides that, performance tests over fabricated membranes were also reported, including salt rejection, water flux, pH, and salinity. All tests will be explained in detail below.

3.1. Membranes characterization

3.1.1.Fourier transform infrared spectroscopy (FTIR)

The identification of functional groups has been applied using FTIR analysis to identify the chemical compound groups presented in the fabricated membranes. Raw material based on CA, PEG, as basic membranes, and chitosan contains organic compounds that are easily identified using FTIR. Meanwhile, the TiO_2-NPs are also placed in fingerprint regions under 750-400 nm [28]. The organic functional group is bonded with -OH stretching affected by water, alcohol specimens, and acidic conditions or organic oxidation. The presence of the -OH group in membranes characterizes the hydrophilicity value over membranes. The polarization functional group from OH attracts the attention of polar groups that bind together in several chemical positions [29]. The hydrophilicity value can be calculated using the peak area from -OH groups in the FTIR graph using the origin application.

Based on Figure 2, the FTIR spectra for each fabricated membrane are shown by varying composition and without adding TiO_2-NPs. The specific absorption on wavenumber of 3479-3549 cm^{-1} is presented of -OH groups from cellulose acetate that have -OH bonds outside the aromatic ring. The C=O (ester) group was presented under the wavenumber of 1755-1757 cm^{-1}, and the -CH group was marked on 2887-2889 cm^{-1}. In addition, the $-CH_3$ group is also shown on 1433-1436 cm^{-1} and the $-NH_2$ group on wavenumber of 1527-1544 cm^{-1}. The Ti-O-Ti group was identified in the specific wavenumber range of 850-500 cm^{-1}, identified with widened absorption.

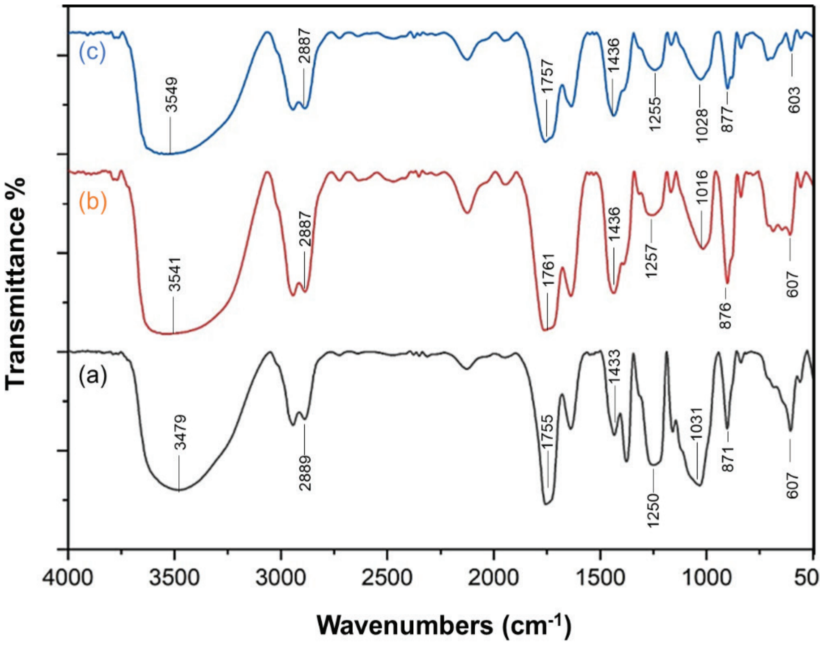

Fig. 2. FTIR spectra of the fabricated membranes, (a) Chitosan polymer membrane, (b) Chitosan–TiO2-NPs (I: 0.25 g), and (c) Chitosan–TiO2-NPs (II: 0.50 g)

Meanwhile, 871-877 cm^{-1} wavenumber indicated a pyranose ring (CA), and 1250-1257 cm^{-1} presented C-O-C stretching from cellulose acetate. Referring to Figure 2, the fabricated membranes have chemically shown -OH, C=O, C-O, -CH -CH$_3$, NH$_2$, and C-O-C groups. The functional groups -OH, C-O, C=O, and C-O-C are the main functional groups of CA. Particularly, the wavenumber characteristics could be identified, such that the peak area of the -OH group was increased along with the addition of TiO$_2$-NPs. This condition indicates an increase in hydrophilicity in the fabricated membrane. The highly increased number of hydroxyl groups also plays a role in photocatalyst and hydrophilicity performances. Based on Figure 1, the principle of RO performance against the fabricated membrane is irradiating under UV light for 30 minutes to activate the performance of TiO$_2$-NPs attached to the membrane surface. In addition, the atomic mass effect of TiO$_2$-NPs is expressed using Hooke's law equation, where the more significant the mass of interacting atoms indicates, the lower the vibrational frequency to a smaller wavenumber.

3.1.2.Scanning Electron Microscopy (SEM)

SEM identification is frequently used as an analytical method to determine the morphological structure of fabricated membranes. The typical structure on the membrane area illustrates the difference of membrane surface against incorporated TiO$_2$-NPs. Based on SEM analysis,

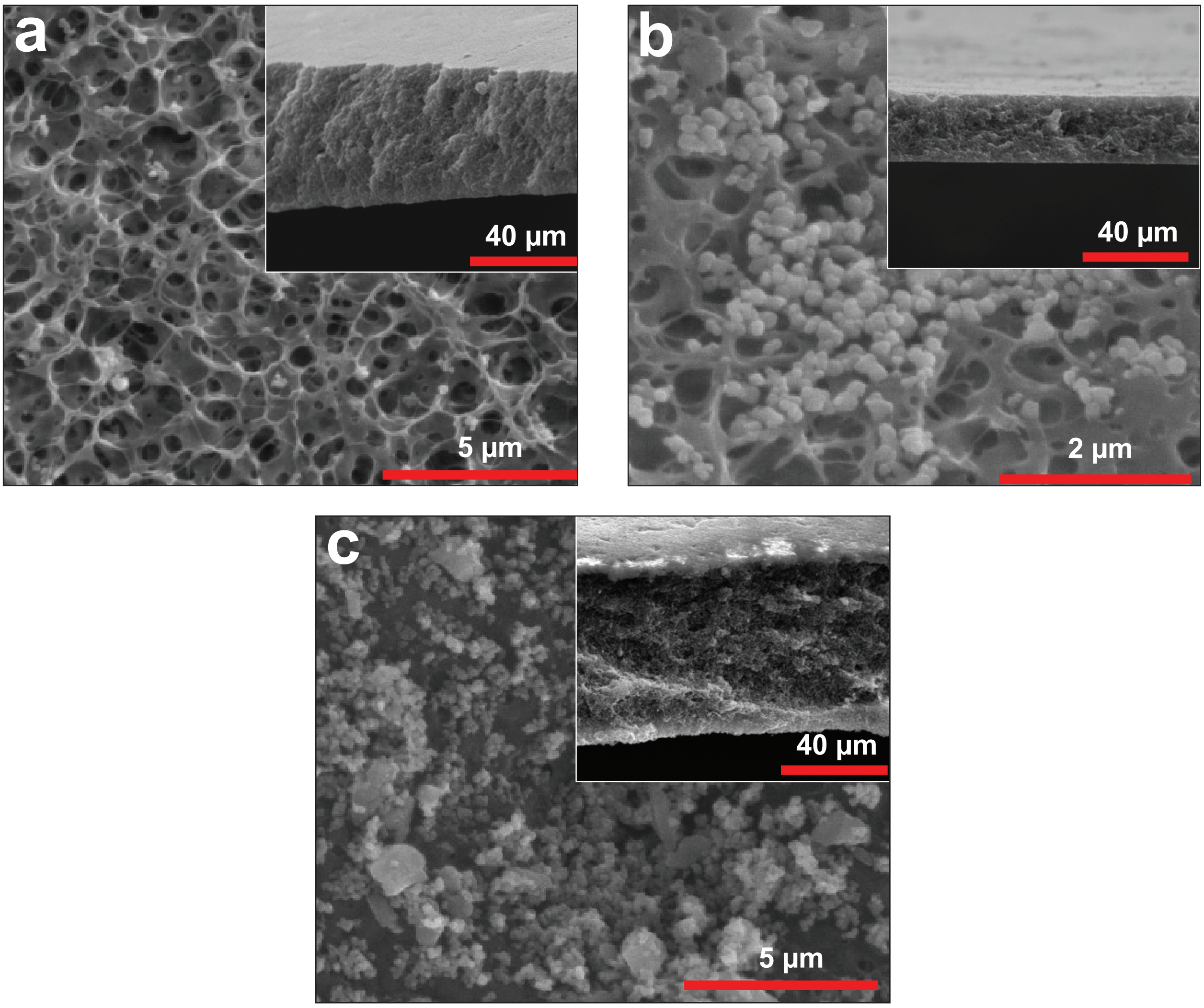

Fig. 3. Morphological analysis of fabricated membranes;
(a) Chitosan polymer membrane [27], (b) Chitosan-TiO$_2$ (I) (0.25 g), and (c) Chitosan-TiO$_2$ (II) (0.5 g)

indentations and protrusions of the fracture surface were also generated, and the enlargement of the pores in the fabricated membrane was observed.

Figure 3 shows a typical morphological analysis of the fabricated membrane; it shows the difference in morphological structure between without and the addition of TiO_2-NPs. Figure 3a shows that the variable chitosan polymer membrane without TiO_2-NPs has irregular pores compared to Figures 3b and 3c. The inclusion of TiO_2-NPs is reflected in a reduction in pore size, particularly at higher TiO_2 concentrations. The solvent exchange process influences the formation of membrane pores during membrane synthesis, which facilitates the entry of TiO_2-NPs into the lattice of membrane pores. Additionally, the incorporation of TiO_2-NPs results in a decrease in pore size due to the small particle size of TiO_2, which attracts particles into the membrane pores. PEG also plays a crucial role in standardizing and increasing the number of membrane pores. Using acetone as a solvent leads to a delayed demixing mechanism, creating tighter pores. To assess the pore size distribution of the fabricated membranes, Figure 4 presents our calculations. In Figure 4a, the average pore size is approximately 800 nm; in Figure 4b, it is around 500 nm, and in Figure 4c, it is roughly 200 nm. These peaks represent the average pore size of each membrane. The largest peaks are observed when TiO_2-NPs are not added, while the smallest pore size is seen when 0.5 grams of TiO_2-NPs are added. This aligns with the morphological

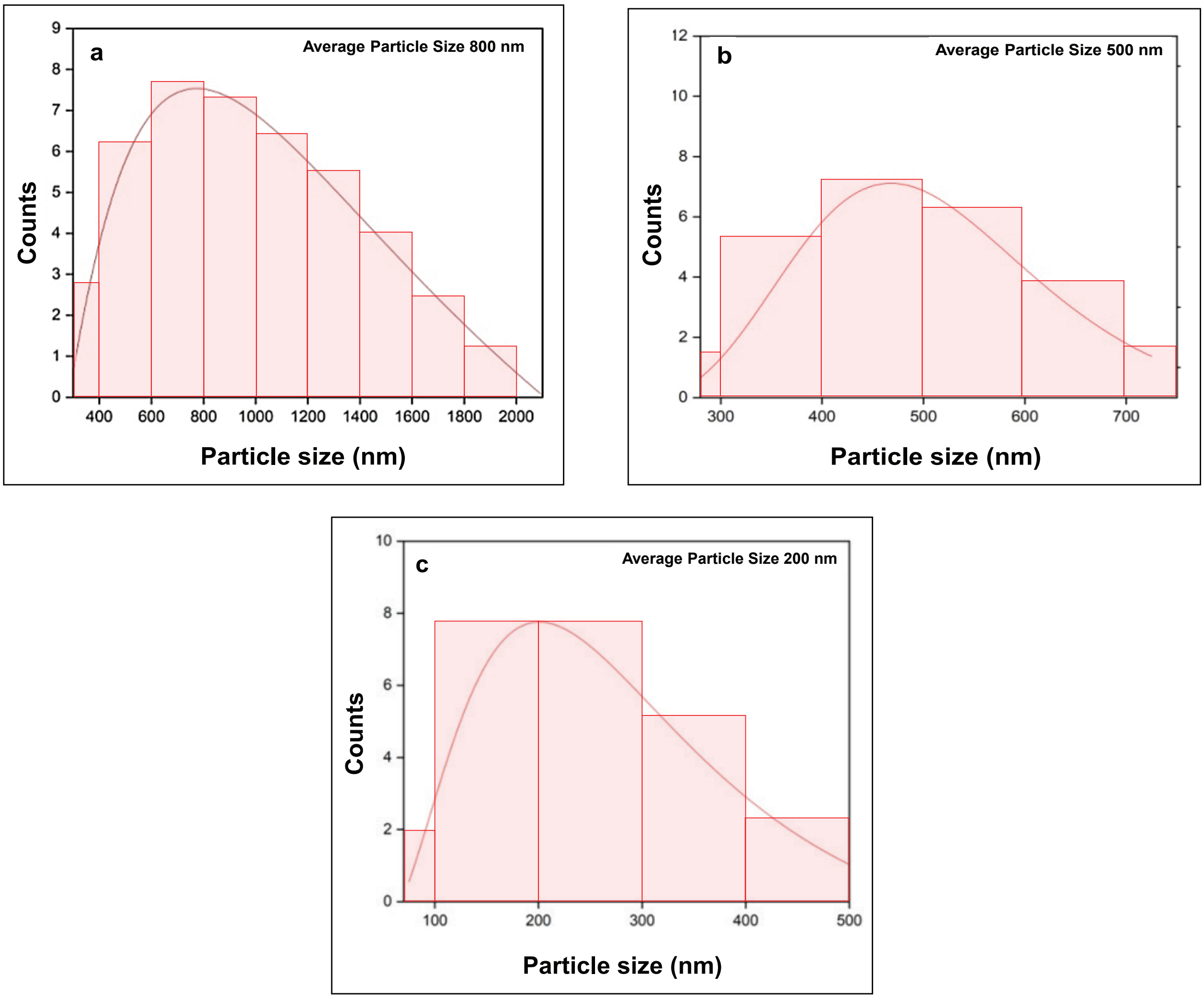

Fig. 4. Histogram of the particle size distribution of fabricated membranes, (a) Chitosan polymer membrane, (b) Chitosan–TiO_2-NPs (I), (c) Chitosan–TiO_2-NPs (II).

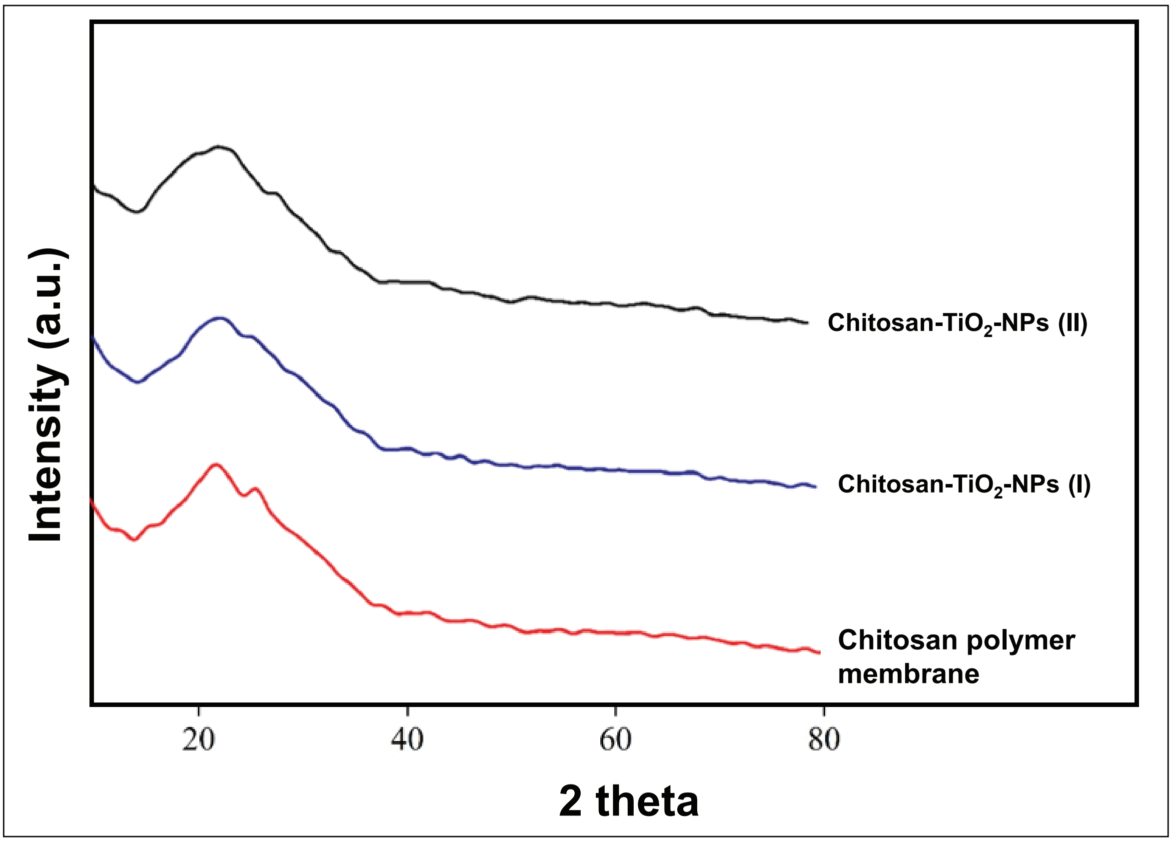

Fig. 5. XRD pattern of fabricated membranes

analysis, indicating that adding TiO_2 further reduces membrane pore size. As per Dietz et al., the typical range of membrane pore sizes formed falls within 100 nm to 10,000 nm, categorizing them as microfiltration membranes [30].

3.1.3. X-ray diffraction (XRD)

The crystallinity phase is also identified to analyze the fabricated membrane, including the composition or type of crystals formed, such as amorphous, semicrystalline, or crystalline. Generally, the TiO_2 phase has three crystals formed: anatase, rutile, and brookite types. In Figure 5, the fabricated membrane includes an amorphous phase with no sharp peaks. High absorption peaks at two theta 25.49° (type I: 0.25 g TiO_2) and 25.84° (type II: 0.50 g TiO_2) correspond to the peaks belonging to the anatase phase based on JCPDS No. 21-1276. The same peak was also shown without adding TiO_2 at two theta of 22.95°. This was identified from the crystallinity of the chitosan polymer membrane. Based on particle size analysis, the average particle size of TiO_2 in chitosan-TiO_2-NPs (I) and chitosan-TiO_2-NPs (II) were 2.92 nm and 2.97 nm, respectively These conditions were expressed that the TiO_2 was quickly inserted into the membrane pore lattice to strengthen the structure and reduce the membrane pores. In addition, a lower crystalline nature or higher amorphous structure coincides with the decrease of polymer chain packing and will result in higher permeability performance.

3.2. Reverse osmosis test

3.2.1.Determination of water flux and salt rejection

Before the analysis of water flux, the water compaction in the RO system was conducted to achieve a uniform structure with steady water flux. This condition has been performed using a high-pressure pump in the RO system to remove the air trapped inside the installation. The compaction of water pressure results in changes in the membrane position. However, the water pressure in this study was 68 bar above an osmosis pressure for

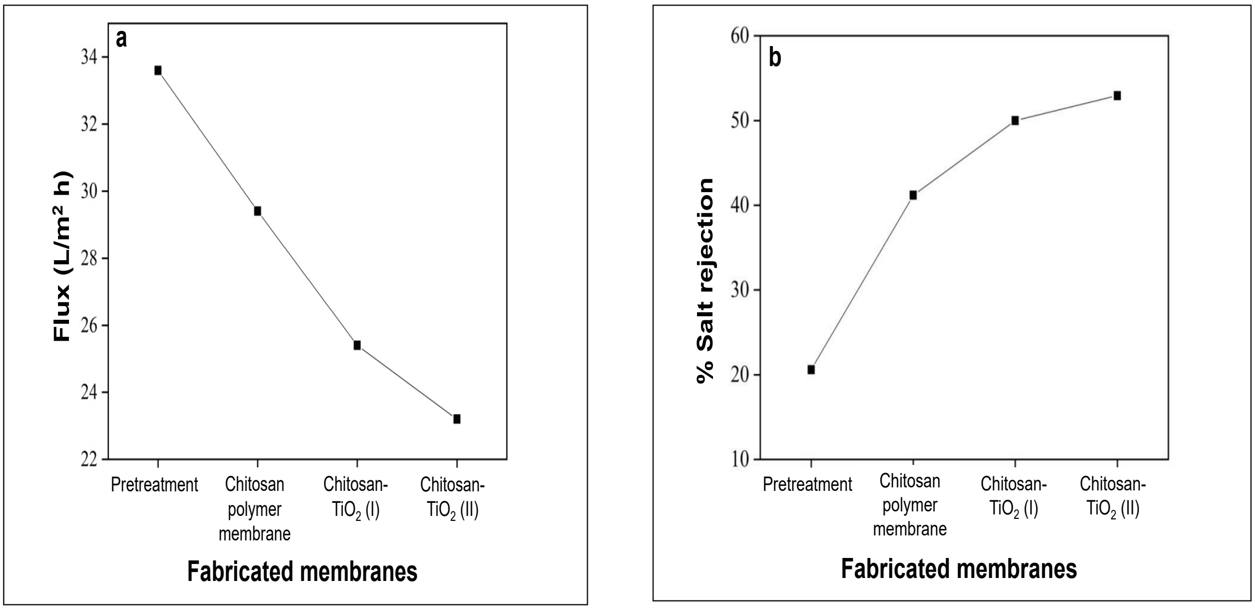

Fig. 6. Membranes performance tests, (a) water flux and (b) salt rejection

60 minutes. The fabricated membrane showed an almost constant decrease with the addition of TiO_2-NPs, and RO testing for 60 min of operation has confirmed that the permeate production is very minimal due to the tiny membrane pores (Fig. 6a). The TiO_2 plays an essential role in the porosity and selectivity of the fabricated membranes, this condition makes the membrane pores tighter. The slow flux reduction can be associated with the porosity and strength of the membrane. The compaction results in a denser membrane structure, which minimizes the water flux.

Salt rejection was also identified to determine the salt content in the permeate. A desalination test was carried out with the RO system by comparing salt concentration results to permeate water with feed water whose units refer to the percentage of salt rejected. Based on the analytical results in Figure 6b, salt rejection increases with the addition of TiO_2-NPs. This graph is inversely proportional to the water flux. It has been discovered that such fine-regulation of the polymer microporous structure leads to a crucial increase in the salt rejection of the chitosan-TiO_2 (II) membrane towards high-performance RO desalination [16]. Based on the salt rejection results, adding 0.5 grams of TiO_2 can increase salt rejection with a value of 52.94% following the morphological analysis that the membrane pore size affects salt rejection in RO desalination.

3.2.2. Determination of pH and salt contents

Water quality (pH) based on chemical properties is also analyzed using a pH meter to determine acidity or alkaline salt content. In general, the pH of seawater varies depending on the location of the collection area, with a range of pH conditions between 6.0 and 8.5. The feed water comes from Southeast Sulawesi Province, Indonesia, with a pH of 7.7. We determined the pH level to observe if the RO desalination process of seawater influences changes in pH value. Fluctuations also affect the high and low pH of the feed water in terms of the levels of O_2 and CO_2 dissolved in the feed water. Based on the analysis results (Figure 7a), the pH measurement results decrease along with the increase in TiO_2 addition to the membrane; although this condition is not too significant, it shows there is little change.

Furthermore, the surface potentials of the membranes produced exhibit negativity when the pH is above 7 and 6. This negativity signifies a substantial electrostatic repulsion between the negatively charged membrane surface and the Cl^- ions at higher pH levels [31]. As a result, the desalination process led to a reduction in salt levels of over 53%. These findings are consistent with earlier studies that have reported similar data regarding the incorporation of TiO_2 into CA-PEG membranes [31]. The results of salt content by three RO membranes at different TiO2-NP concentrations are shown in Figure 7b. The experiment was conducted using a refractometer instrument to identify the measured salt concentration of the feed water. This was calculated based on the percentage of salt content before and after the RO desalination process. Generally, salinity is defined as the salt content at which the salt level in aqueous solutions and some seawater have unequal salinity values. In this case, the salinity of pure seawater on Southeast Sulawesi beach ranges from 34 ppt. Based on Figure 7b, there is a decrease in salt content in permeate water that passes through each fabricated membrane. The feed water passed the pretreatment process and decreased the salt content to 27 ppt. This indicates that the pretreatment process containing sand, palm fibre, activated charcoal, and filter paper contributes to a decrease in salt content by 20.5%. This was followed by a membrane without TiO_2 addition, which reduced 26% (20 ppt) from the pretreatment process. Furthermore, the performance comparison of the membrane with the addition of TiO_2 0.25 g and 0.5 g showed a decrease in the percentage of salt content by 37% (17 ppt) and 41% (16 ppt), respectively. From the results of this study, it can be concluded that increasing the composition of TiO_2 as an agent of permeability and selectivity of chitosan membrane has a high effect in changing the salt content in seawater.

Numerous research studies imply that TiO_2-NPs alter water flux and rejection performance, as shown in Table 1[27,32-35]. All studies using the phase inversion method (NIPS) and solution casting to fabricate RO membranes incorporated with TiO_2-NPs have produced different flux and salt rejection results. The addition of TiO_2 resulted in an increase in total salt rejection followed by flux values. This condition implies that the TiO_2-modified membrane affects the porosity of the membrane, which also acts the performance. When the average pore size increases, the CA-TiO_2 membrane becomes more porous.

4. Conclusion

The proposed method introduced TiO_2-NPs into chitosan membranes to enhance permeability and selectivity performance for reverse osmosis (RO) desalination. It was incorporated into

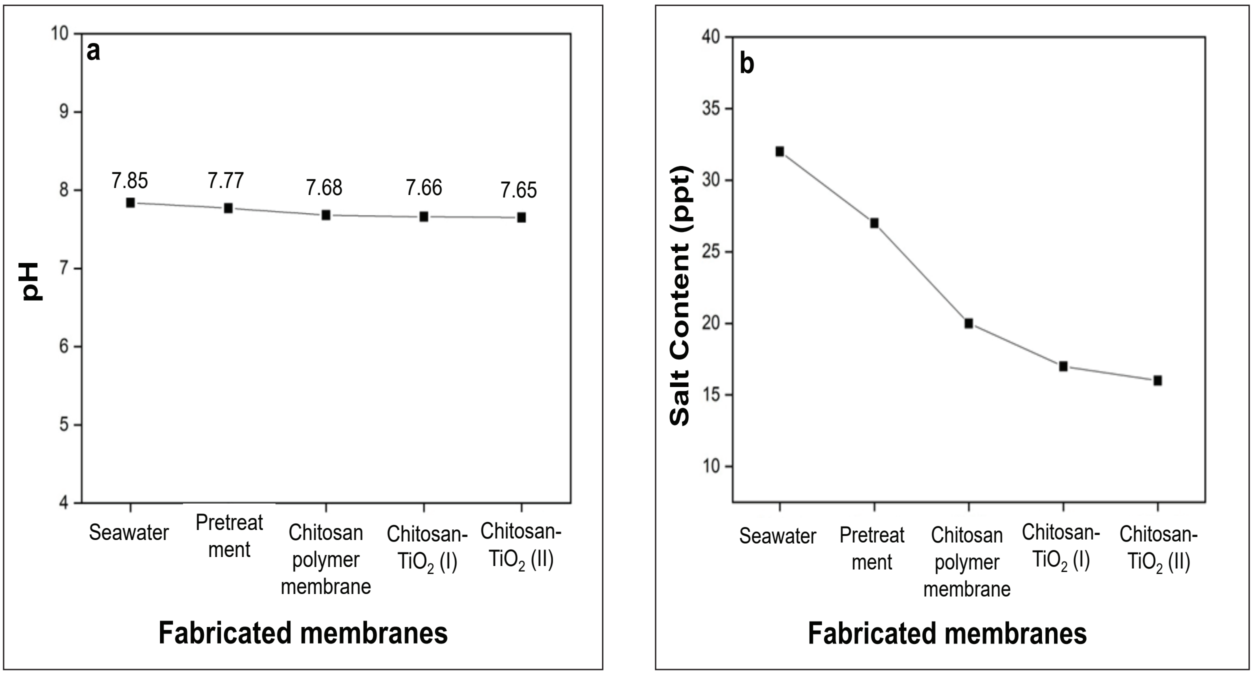

Fig. 7. Membranes performance tests, (a) pH and (b) salt content

Table 1. Comparison between previous and current studies

Polymer composition	NPs	Methods	Flux (LMH)	Pollutant	Rejection %	Ref.
Cellulose acetate / polyethylene-glycol / chitosan	TiO_2	Phase inversion method (NIPS) and casting solution	50.00	Salt	61.76	[27]
Polyvinyl alcohol / cellulose acetate	TiO_2	Phase inversion method (NIPS) and casting solution	15.50	Salt	92	[32]
Cellulose acetate	TiO_2	Phase inversion method (NIPS) and casting solution	58.21	Salt	92.6	[33]
Polyvinylpyrrolidone / N-methyl pyrrolidone	TiO_2	Phase inversion method (NIPS) and casting solution	34.3	Salt	-	[34]
Polyamide/carbon dots	TiO_2	Phase inversion method (NIPS) and casting solution	54.6	Salt	99.2	[35]
Chitosan/cellulose acetate / polyethylene-glycol	TiO_2	Phase inversion method (NIPS) and casting solution	23	Salt	52.94	This work

chitosan membranes using the surface coating method, with varying TiO_2 mass fractions of 0.25 grams and 0.50 grams. The physical characterization of the fabricated membranes revealed functional groups representing organic and inorganic compounds. Additionally, TiO_2-NPs were identified within the wavenumber range of 850-500 cm^{-1}, indicating the presence of Ti-O-Ti bonds. Morphological analysis exhibits the TiO_2-NPs led to significantly smaller pores in chitosan membranes due to their contribution to the amorphous phase structure. During the RO desalination process, the performance of the fabricated membranes was assessed in terms of water flux and salt rejection. The addition of TiO_2-NPs resulted in a 23 Lm^{-2} h^{-1} decrease in water flux and a 52.94% increase in salt rejection. Furthermore, the pH and salt content values were measured, indicating a reduction under favourable conditions. TiO_2 played a crucial role as a permeability and selectivity enhancer within the TiO_2-chitosan membranes, significantly reducing salt content in seawater.

5. Acknowledgments

Financial support from the Ministry of Education, Culture, Research, and Technology, Republic of Indonesia, is gratefully acknowledged for basic research grant no. 51/UN29.20/PG/2023 and World Class Professor research grant no. 3252/E4/DT.04.03/2023. Department of Chemistry, Faculty of Mathematics and Natural Sciences, Halu Oleo University, and Photocatalysis Laboratory for facilitating this research.

6. References

[1] P.H. Nienhuis, J. Coosen, W. Kiswara, Community structure and biomass distribution of seagrasses and macrofauna in the Flores Sea, Indonesia, Netherlands J. Sea Res., 23 (1989) 197–214. https://doi.org/10.1016/0077-7579(89)90014-8.

[2] E. Hastuti, M.W. Wardiha, A study of brackish water membrane with ultrafiltration pretreatment in indonesia's coastal area, J. Urban Environ. Eng., 6 (2012) 10–17. https://doi.org/10.4090/juee.2012.v6n1.010017.

[3] S. Han, Y.-W. Rhee, S.-P. Kang, Investigation of salt removal using cyclopentane hydrate formation and washing treatment for seawater desalination, Desalination, 404 (2017) 132–137. https://doi.org/10.1016/j.desal.2016.11.016.

[4] S. Timoori, Environmental Health: Evaluation of heavy metals pollution in Isfahan industrial zone from soils, well/eluent waters and waste water by microwave-electro-thermal atomic absorption spectrometry, Anal. Methods Environ. Chem. J., 2 (2019) 55–62. https://doi.org/10.24200/amecj.v2.i01.44.

[5] B. Suhartawan, J. Haurissa, S.A. Rumawak, Lake Sentani water quality index based on NSF-WQI as raw water for drinking water for Lake Sentani Coastal communities, Jayapura Regency, J. Syntax Admiration, 3 (2022) 1189–1204. https://doi.org/10.46799/jsa.v3i9.481.

[6] K. Katsanou, H.K. Karapanagioti, Surface water and groundwater sources for drinking water, Appl. Adv. Oxid. Process. Drink. Water Treat., (2019) 1–19. https://doi.org/10.1007/698_2017_140.

[7] S.H. Mutasher, H.S. Al-Lami, Preparation of chitosan films plasticized by lauric and maleic acids, Anal. Methods Environ. Chem. J., 5 (2022) 43–54. https://doi.org/10.24200/amecj.v5.i04.209.

[8] Y. Cai, J. Wu, S.Q. Shi, J. Li, K.-H. Kim, Advances in desalination technology and its environmental and economic assessment, J. Clean. Prod., 397 (2023) 136498. https://doi.org/10.1016/j.jclepro.2023.136498.

[9] A.M. Ghaithan, A. Mohammed, L. Hadidi, Assessment of integrating solar energy with reverse osmosis desalination, Sustain. Energy Technol. Assessments, 53 (2022) 102740. https://doi.org/10.1016/j.seta.2022.102740.

[10] A. Hassanzadeh, B. Amirheidari, A. Salarifar, A. Asadipour, Y. Pourshojaei, Synthesis and identification of meta-(4-bromobenzyloxy) benzaldehyde thiosemicarbazone (MBBOTSC) as novel ligand for cadmium extraction by ultrasound assisted-dispersive-ionic liquid-liquid micro extraction method, Anal. Methods Environ. Chem. J., 4 (2021) 92–106. https://doi.org/10.24200/amecj.v4.i04.161.

[11] A.B.D.N. Kurnia, R. Ismiati, A. Annisa, F. Finandia, N.N.A. Nissa, R.C. Dewi, Economic evaluation analysis of nano-silica ultrafiltration membrane production from sand, Int. J. Energ., 3 (2018) 6–9. https://doi.org/10.47238/ijeca.v3i1.59.

[12] A. Knebel, J. Caro, Metal–organic frameworks and covalent organic frameworks as disruptive membrane materials for energy-efficient gas separation, Nat. Nanotechnol., 17 (2022) 911–923. https://doi.org/10.1038/s41565-022-01168-3.

[13] V. Vatanpour, M.E. Pasaoglu, H. Barzegar, O.O. Teber, R. Kaya, M. Bastug, A. Khataee, I. Koyuncu, Cellulose acetate in fabrication of polymeric membranes: A review, Chemosphere, 295 (2022) 133914. https://doi.org/10.1016/j.chemosphere.2022.133914.

[14] I. Ounifi, Y. Guesmi, C. Ursino, R. Castro-Muñoz, H. Agougui, M. Jabli, A. Hafiane, A. Figoli, E. Ferjani, Synthesis and characterization of a thin-film composite nanofiltration membrane based on polyamide-cellulose acetate: application for water purification, J. Polym. Environ., 30 (2022) 707–718. https://doi.org/10.1007/s10924-021-02233-z

[15] Y. Yamashita, T. Endo, Deterioration behavior of cellulose acetate films in acidic or basic aqueous solutions, J. Appl. Polym. Sci., 91 (2004) 3354–3361. https://doi.org/10.1002/app.13547.

[16] Y. Yang, Z. Wang, Z. Song, D. Liu, J. Zhang, L. Guo, W. Fang, J. Jin, Thermal treated amidoxime modified polymer of intrinsic microporosity (AOPIM-1) membranes for high permselectivity reverse osmosis desalination, Desalination, 551 (2023) 116413. https://doi.org/10.1016/j.desal.2023.116413.

[17] S. Yang, R. Tang, Y. Dai, T. Wang, Z. Zeng,

L. Zhang, Fabrication of cellulose acetate membrane with advanced ultrafiltration performances and antibacterial properties by blending with HKUSt-1@ LCNFs, Sep. Purif. Technol., 279 (2021) 119524. https://doi.org/10.1016/j.seppur.2021.119524.

[18] S. Hasheminasab, J. Barzin, R. Dehghan, High-performance hemodialysis membrane: Influence of polyethylene glycol and polyvinylpyrrolidone in the polyethersulfone membrane, J. Membr. Sci. Res., 6 (2020) 438–448. https://doi.org/10.22079/JMSR.2020.128323.1391.

[19] L. Qi, R. Liang, T. Jiang, W. Qin, Anti-fouling polymeric membrane ion-selective electrodes, TrAC Trends Anal. Chem., 150 (2022) 116572. https://doi.org/10.1016/j.trac.2022.116572.

[20] M. Chaudhary, A. Maiti, Fe–Al–Mn@ chitosan based metal oxides blended cellulose acetate mixed matrix membrane for fluoride decontamination from water: removal mechanisms and antibacterial behavior, J. Memb. Sci., 611 (2020) 118372. https://doi.org/10.1016/j.memsci.2020.118372.

[21] P.S. Bakshi, D. Selvakumar, K. Kadirvelu, N.S. Kumar, Chitosan as an environment friendly biomaterial–a review on recent modifications and applications, Int. J. Biol. Macromol., 150 (2020) 1072–1083. https://doi.org/10.1016/j.ijbiomac.2019.10.113.

[22] M. Nurdin, D. Wibowo, T. Azis, R.A. Safitri, M. Maulidiyah, A. Mahmud, F. Mustapa, R. Ruslan, A. Salim, L. Ode, Photoelectrocatalysis response with synthetic Mn–N–TiO2/Ti electrode for removal of rhodamine B dye, Surf. Eng. Appl. Electrochem., 58 (2022) 125–134. https://doi.org/10.3103/S1068375522020077.

[23] D. Wibowo, M.Z. Muzakkar, M. Maulidiyah, M. Nurdin, S.K.M. Saad, A.A. Umar, Morphological analysis of Ag doped on TiO2/Ti prepared via anodizing and thermal oxidation methods, Biointerface Res. Appl. Chem., 12 (2022) 1421–1437. https://doi.org/10.33263/BRIAC122.14211427.

[24] M. Natsir, M. Maulidiyah, A. Ansharullah, Z. Arham, D. Wibowo, M. Nurdin, Natural biopesticide preparation as antimicrobial material based on lignin photodegradation using mineral ilmenite (FeoTio2), Int. Res. J. Pharm., 9 (2018) 170–174. https://doi.org/10.7897/2230-8407.096111.

[25] M. Nurdin, N. Dali, I. Irwan, M. Maulidiyah, Z. Arham, R. Ruslan, B. Hamzah, S. Sarjuna, D. Wibowo, Selectivity determination of Pb2+ Ion based on TiO2-Ionophores BEK6 as carbon paste electrode composite, Anal. Bioanal. Electrochem., 10 (2018) 1538–1547. https://doi.org/-.

[26] D. Wibowo, M.Z. Muzakkar, S.K.M. Saad, F. Mustapa, M. Maulidiyah, M. Nurdin, A.A. Umar, Enhanced visible light-driven photocatalytic degradation supported by Au-TiO<inf>2</inf> coral-needle nanoparticles, J. Photochem. Photobiol. A Chem., 398 (2020) 112589. https://doi.org/10.1016/j.jphotochem.2020.112589.

[27] D. Wibowo, F. Mustapa, S. Selviantori, M. Idris, A. Mahmud, M. Maulidiyah, M.Z. Muzakkar, A.A. Umar, M. Nurdin, CA/PEG/Chitosan membrane incorporated with TiO2 nanoparticles for strengthening and permselectivity membrane for reverse osmosis desalination, Environ. Nanotechnol. Monit. Manag., 20 (2023) 100848. https://doi.org/10.1016/j.enmm.2023.100848.

[28] S. Chelbi, D. Djouadi, A. Chelouche, L. Hammiche, T. Touam, A. Doghmane, Effects of Ti-precursor concentration and annealing temperature on structural and morphological properties of TiO 2 nano-aerogels synthesized in supercritical ethanol, SN Appl. Sci., 2 (2020) 1–10. https://doi.org/10.1007/s42452-020-2633-3.

[29] Y.-H. Chiao, A. Sengupta, S.-T. Chen, S.-H. Huang, C.-C. Hu, W.-S. Hung, Y. Chang, X. Qian, S.R. Wickramasinghe, K.-R. Lee, Zwitterion augmented polyamide membrane for improved forward osmosis performance with significant antifouling characteristics,

Sep. Purif. Technol., 212 (2019) 316–325. https://doi.org/10.1016/j.seppur.2018.09.079.

[30] P. Dietz, P.K. Hansma, O. Inacker, H.-D. Lehmann, K.-H. Herrmann, Surface pore structures of micro-and ultrafiltration membranes imaged with the atomic force microscope, J. Memb. Sci., 65 (1992) 101–111. https://doi.org/10.1016/0376-7388(92)87057-5.

[31] M.H. Oo, L. Song, Effect of pH and ionic strength on boron removal by RO membranes, Desalination, 246 (2009) 605–612. https://doi.org/10.1016/j.desal.2008.06.025.

[32] E.S. Mansor, H. Abdallah, A.M. Shaban, Development of TiO2/polyvinyl alcohol-cellulose acetate nanocomposite reverse osmosis membrane for groundwater-surface water interfaces purification, Mater. Sci. Eng. B, 289 (2023) 116222. https://doi.org/10.1016/j.mseb.2022.116222.

[33] H. Jain, A.K. Verma, R. Dhupper, S. Wadhwa, M.C. Garg, Development of CA-TiO2-incorporated thin-film nanocomposite forward osmosis membrane for enhanced water flux and salt rejection, Int. J. Environ. Sci. Technol., 19 (2022) 5387–5400. https://doi.org/10.1007/s13762-021-03415-x.

[34] A.H. Konsowa, H.Z. AbdAllah, S. Nosier, M.G. Eloffy, Thin-film nanocomposite forward osmosis membrane for water desalination: synthesis, characterization and performance improvement, Water Qual. Res. J., 57 (2022) 72–90. https://doi.org/10.2166/wqrj.2022.034.

[35] V. Vatanpour, S. Paziresh, S.A.N. Mehrabani, S. Feizpoor, A. Habibi-Yangjeh, I. Koyuncu, TiO2/CDs modified thin-film nanocomposite polyamide membrane for simultaneous enhancement of antifouling and chlorine-resistance performance, Desalination, 525 (2022) 115506. https://doi.org/10.1016/j.desal.2021.115506.

Anal. Methods Environ. Chem. J. 6 (4) (2023) 19-36

Research Article, Issue 4
Analytical Methods in Environmental Chemistry Journal
Journal home page: www.amecj.com/ir

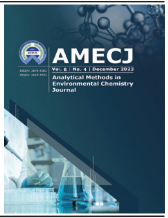

Rapid extraction and separation of mercury in water and food samples based on micelles and azo-thiazoles complexation before determination by UV-Vis spectrophotometry

Hesham H. El-Feky[a,*], **Talaat Y. Mohammed**[a], **Alaa S. Amin**[a] **and Mohammed A. Kassem**[a, b]
[a] *Chemistry Department, Faculty of Science, Benha University, Benha 13518, Egypt.*
[b] *Chemistry Department, Faculty of Applied Science, Umm Al-Qura University, Makkah, Saudi Arabia*

ARTICLE INFO:

Received 15 Aug 2023
Revised form 13 Oct 2023
Accepted 11 Nov 2023
Available online 29 Dec 2023

Keywords:
Mercury,
UV-Vis spectrophotometry,
Ligand,
Azo-thiazoles,
Complexation,
Water and Food samples

ABSTRACT

A simple and sensitive procedure has been established for analyzing mercury (II) ions spectrophotometrically in the presence of micellar medium using three azo-thiazoles complexing reagents: 2-amino-6-(thiazole-2-yldiazenyl)-3-pyridinol ($C_8H_7N_5OS$), 8-hydroxy-7-(thiazole-2-yldiazenyl) quinoline-5-sulfonic acid ($C_{12}H_8N_4O_4S_2$), and 1-hydroxy-4-(thiazole-2-yldiazenyl)-2-naphthoic acid ($C_{14}H_9N_3O_3S$). H1 NMR spectra validated the three azo thiazoles synthesized material. Tween 80 (polysorbate 80) and cetyltrimethylammonium bromide ($C_{19}H_{42}BrN$ as molecular biology) are micellar mediums to enhance sensitivity. Absorbances were measured for Hg (II) complexation with R_1, R_2, and R_3 at λ_{max} of 617, 633, and 554 nm, respectively. The UV-Vis spectrophotometer showed calibration curves in the 0.2-15 mg L^{-1}. The molar absorptivity, Sandell's sensitivity, detection, and quantification limits (LOD, LOQ) were determined. The interferences of various ions were investigated, and a statistical assessment of the results was performed. The methods have been applied for trace determination of mercury (II) in food and environmental water samples. For food samples, all samples were digested before complexation with the azo-thiazoles material at optimized pH before determination by UV-Vis spectrophotometry.

1. Introduction

Environmental monitoring is a subject that requires the development of novel analytical methods. The speciation of potentially hazardous metal ions is essential for comprehending their eco-toxicological and biological properties, which depend on the chemical species. Extensive research has been devoted to developing sensitive, relatively simple, accurate, rapid, and cost-effective methods for determining industrially pertinent metals that may harm human health [1]. Mercury is a problematic natural pollutant because it can hurt almost all living things [2]. As a result of human environmental achievements, mercury compounds can exist in various settings [3]. They frequently exist in trace amounts in natural water types [4]. Mercury pollution is a significant problem in the lakes and rivers near industrial zones. Therefore, it is essential to develop new, selective, efficient, and cost-effective monitoring procedures for mercury ions [5]. Low Hg (II) concentrations in the target species pose a significant challenge in mercury determination. In naturally occurring water samples, the predominant forms of mercury are inorganic

---

*Corresponding Author: Hesham H. El-Feky
Email: hesham.elfeky@fsc.bu.edu.eg
https://doi.org/10.24200/amecj.v6.i04.258

mercury (mercurous and mercuric) and organic mercury (CH_3Hg^+). Modern records indicate that the total (Hg^{2+}, MHg^+) concentrations range from 0.2-100 ng L^{-1} and the organic mercury (CH_3Hg^+) has a a concentration of 0.05 ng L^{-1} in water [6]. Many analytical techniques, such as inductively coupled plasma (ICP) [7], cold vapour atomic absorption spectrometry (CV-AAS) [8], neutron activation analysis (NAA) [9], x-ray fluorescence [10], atomic fluorescence spectrometry (AFS) [11], and spectrophotometric technique [12] had been advanced to monitor mercury ion at a micro level. Each of the above methods has some advantages; however, they may have disadvantages, such as low reproducibility and limited sample flexibility. Without pre-concentration, the inductively coupled plasma method was suitable for determining trace amounts of Hg (II). However, this instrument is quite expensive to purchase and maintain. Additionally, this technique has some significant interference [11]. Due to its simplicity, atomic absorption spectrometry was a suitable and widely utilised technique for accurate Hg(II) determination. In the meantime, its application is limited due to its limited linear range and significant spectral interference from volatile substances [13]. Due to the low Hg (II) concentration, these practises are not directly applicable to environmental and biological models and/or frequently require pre-concentration steps to enhance selectivity. Several photometric reagents have been used for spectrophotometric mercury ion determination. Dithizone was the most common reagent used for this purpose [14]. Before photometric analysis, the Hg(II)-dithizone complex is taken out with either CCl_4 or $CHCl_3$ [15]. Based on the absorbance measurements of the formed complexes in the presence of surfactants, we report for the first time the direct spectrophotometric determination of the Hg(II) ion with three novel azo dyes. Also, many methods based on nanotechnology were used for mercury extraction/removal from different water, air, human and food (vegetable and nut) samples. Mousavi et al used Tetraethyl thiuram disulfide [$(C_2H_5)_2$-$NCSS_2CSN$-$(C_2H_5)_2$; TET] mixed with ionic liquids for extraction/speciation mercury in human samples by dispersive liquid-liquid microextraction (DLLME) coupled to CV-AAS [16]. Osanloo et al used silver nanoparticles coating on micro glassy balls for removal mercury from air and Rouhollahi et al can be determined mercury in air and human samples [17-19]. Golbabaei, Bagheri and hassani showed that mercury can be determined in biological human samples based on adsorbent by the CV-AAS. In addition, they used the nano-palladium functionalized on the silica nanoparticles for mercury removal from air by the GFSC method [20-22]. Moreover, some methods based on adsorbents such as MWCNTs, pyrrolic and pyridinic nitrogen doped porous graphene nanostructure(N-D-PNG) extracted mercury from water, food, and air samples [23-25].

In this study, we prepared the azo dyes based on new synthesis include, 2-amino-6-(thiazole-2-yldiazenyl)-3-pyridinol (C8H7N5OS) [R_1], 8-hydroxy-7-(thiazole-2-yldiazenyl) quinoline-5-sulfonic acid ($C_{12}H_8N_4O_4S_2$) [R_2], and 1-hydroxy-4-(thiazole-2-yldiazenyl)-2-naphthoic acid ($C_{14}H_9N_3O_3S$) [R_3] (Fig. 1). The H1 NMR spectra of all synthesized azo dyes. Herein, Hg(II) was successfully measured at the micro level in different water and food samples using the proposed methodologies by UV-Vis spectrometry after complexation with azo dyes. The food samples were digested before the complexation and determination procedure. The approach has several advantages, including its low cost, ability to be applied to real samples, and broad linear range.

2. Experimental

2.1. Instrumentation

All absorption measurements are taken with a Jasco UV-Vis spectrophotometer (model V530, Jasco, Tokyo, Japan) with a scanning speed of 400 nm/min, a bandwidth of 2.0 nm, and 1.0 cm pair-matched quartz cells. A pH meter (HI 8014, HANNA Instruments, Woonsocket, RI, USA) was used to adjust the pH of all solutions. We used a Fluoromax-4 (Horbiba Scientific, Kyoto, Japan) for the spectrofluorimetric observations. Both the excitation and emission slit widths were 9 nm.

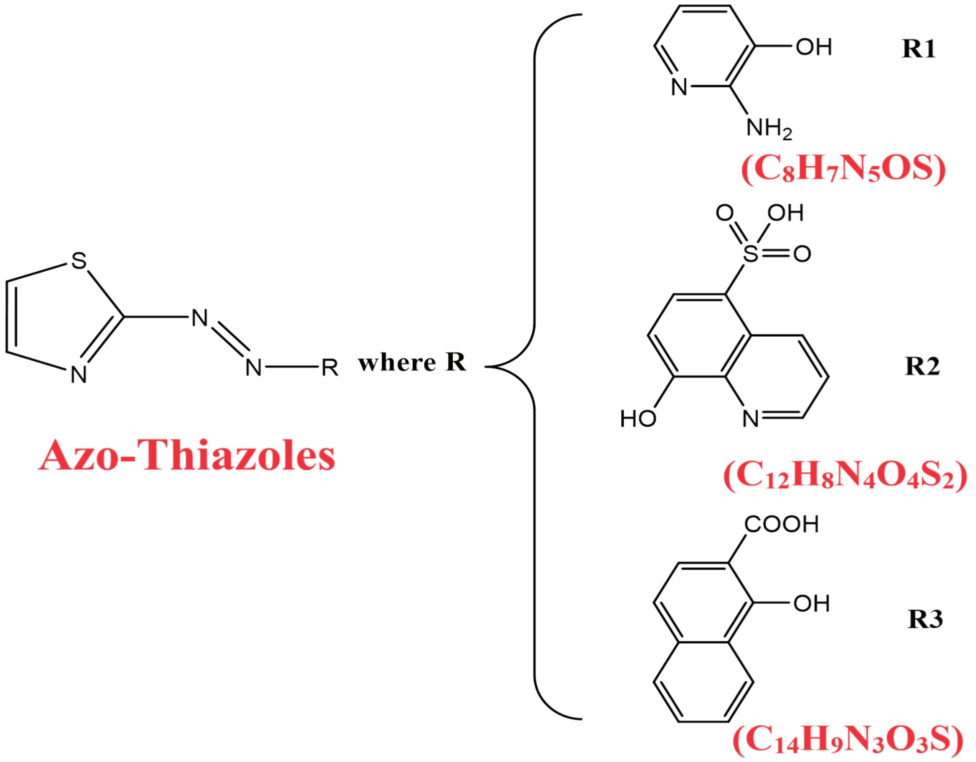

Fig.1. Synthesis of azo dyes include, 2-amino-6-(thiazole-2-yldiazenyl)-3-pyridinol (C8H7N5OS) [R_1], 8-hydroxy-7-(thiazole-2-yldiazenyl) quinoline-5-sulfonic acid ($C_{12}H_8N_4O_4S_2$) [R_2], and 1-hydroxy-4-(thiazole-2-yldiazenyl)-2-naphthoic acid ($C_{14}H_9N_3O_3S$) [R_3]

2.2. Reagents and Chemicals

All chemicals and reagents employed in this study were of analytical grade (Merck, Darmstadt, Germany), and the solutions were prepared using bi-distilled water. A stock solution of 1×10^{-2} M mercuric chloride was prepared by weighing out 0.679 g $HgCl_2.2H_2O$, dissolved in the least amount of bi-distilled water and completed in a 100-mL measuring flask to the mark with bi-distilled water. The stock solution was then standardized by EDTA [26]. All used solutions were carefully diluted from a stock solution. At room temperature, the solution held up for a whole month. The preceding method was used to prepare universal buffer solutions. As a result of the low Hg (II) concentration, these methods are either not directly applicable to environmental and biological models or necessitate additional pre-concentration processes to increase selectivity. Mercury ion concentrations have been measured spectrophotometrically using a variety of photometric reagents. The most commonly used reagent for this was dithizone [27]. Tween 80 [0.5% (v/v)], Triton X-100 [0.5% (v/v)], cetyltrimethylammonium bromide (CTAB) [0.5% (w/v)], and sodium dodecyl sulphate (SDS) [0.5% (w/v)] were used as surfactants due to their commercial availability in a highly purified form, low toxicity, and low charge. Tween 80 and Triton X-100 were prepared by adding 0.5 mL of each surfactant to 50 mL of bi-distilled water and then bringing the volume to 100 mL to achieve a 0.5% (v/v) solution. In the case of SDS and CTAB, a 0.5% (w/v) solution was intended by dissolving 0.5 g of the surfactant in 50 mL of bi-distilled water and then filling a 100 mL measuring flask with bi-distilled water to the desired volume. Nitric acid (HNO_3), 70 %, and hydrogen peroxide (H_2O_2), 30 % (w/w) in H_2O, were obtained from Aldrich.

2.3. Synthesis of reagents

A solution of 2-aminothiazole (10.014 g, 0.1 mole) dissolved in 1:1 (v/v) HCl aqueous solution was cooled in an ice bath at ca. – 5.0 ºC. To this solution, while stirring vigorously, a cold aqueous solution of sodium nitrite (6.903 g, 0.1 mole) was added, and the reaction mixture was kept in an ice bath at a temperature range of 0-5.0ºC for 30 min. The obtained cold diazonium salt was used for coupling with an equivalent quantity of cold solution of 2-amino-3-hydroxypyridine (11.01 g, 0.1 mole), dissolved in 10 % (w/v) NaOH. The formed azo dye (R_1) was kept for 40 min in an ice bath at ca. -5.0ºC, filtered off, washed with bi-distilled water, and dried. The obtained azo compound was finally re-crystallized using absolute C_2H_5OH. For the preparation of the other azo compounds, 8-hydroxy-7-(thiazole-2-glaze) quinoline-5-sulfonic acid [R_2] and 1-hydroxy-4-(thiazole-2-ylazo)-2-naphthoic acid [R_3], a typical procedure was used using 8-hydroxyquinoline-5-sulphonic acid (26.125 g, 0.1 moles) and 1-hydroxy-2-naphthoic acid (18.81 g, 0.1 moles), respectively. The reaction yield was in the range of 75-85 %. The azo compounds showed a sharp melting point, indicating high purity. The compounds were characterized using ^{1}H-NMR spectroscopy (Fig. 2a-c). The reagent solutions were prepared by dissolving 0.110, 0.033 and 0.148 g of R_1, R_2 and R_3 in 100 mL ethanol to obtain 5×10^{-3}, 1×10^{-3} and 5×10^{-3} mol L^{-1} of R_1, R_2 and R_3, respectively.

2.4. General procedure

In a typical procedure, for the reagents R_1 and R_2, an appropriate volume of the sample containing 1×10^{-3} M of Hg(II) was placed in a 10 mL measuring flask. The universal buffer of pH 6.0 (5 mL) or pH

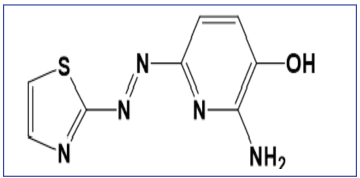

R1

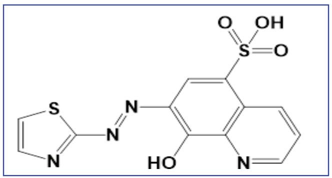

R2

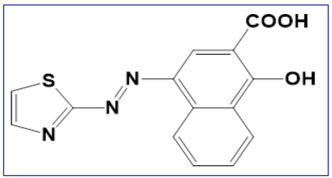

R3

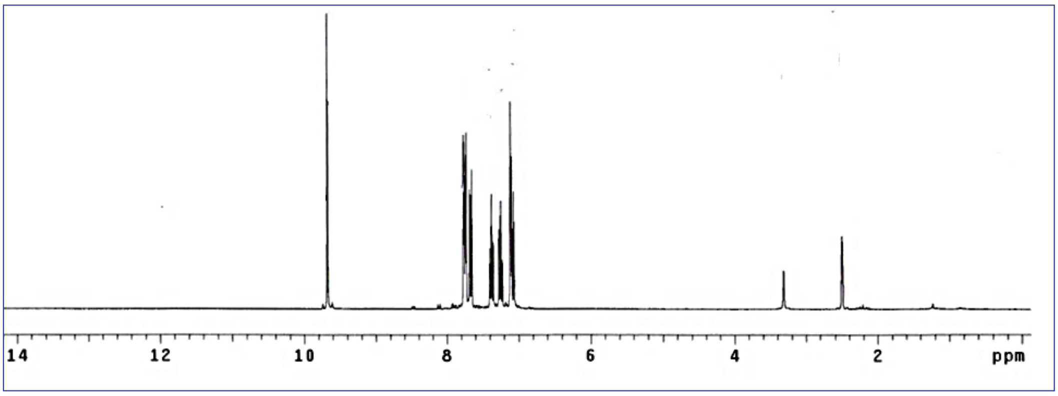

Fig. 2a. ^{1}H-NMR spectroscopy of 2-amino-6-(thiazole-2-yldiazenyl)-3-pyridinol (C8H7N5OS) [R_1]

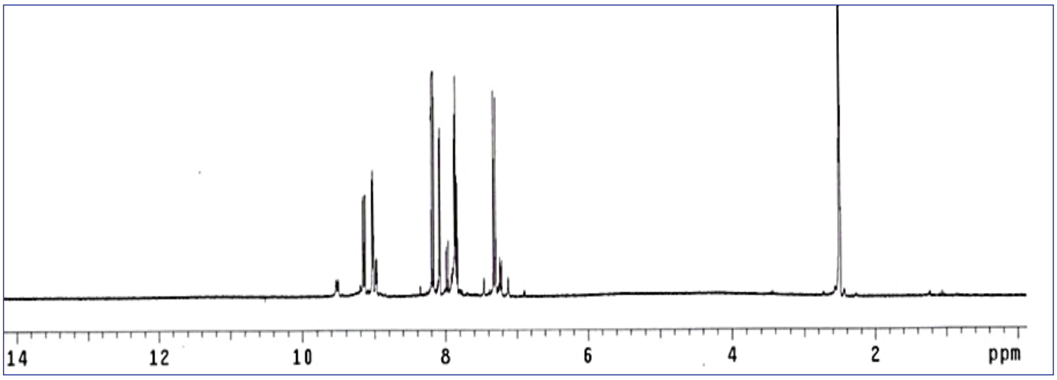

Fig. 2b. ^{1}H-NMR spectroscopy of 8-hydroxy-7-(thiazole-2-yldiazenyl) quinoline-5-sulfonic acid ($C_{12}H_8N_4O_4S_2$) [R_2]

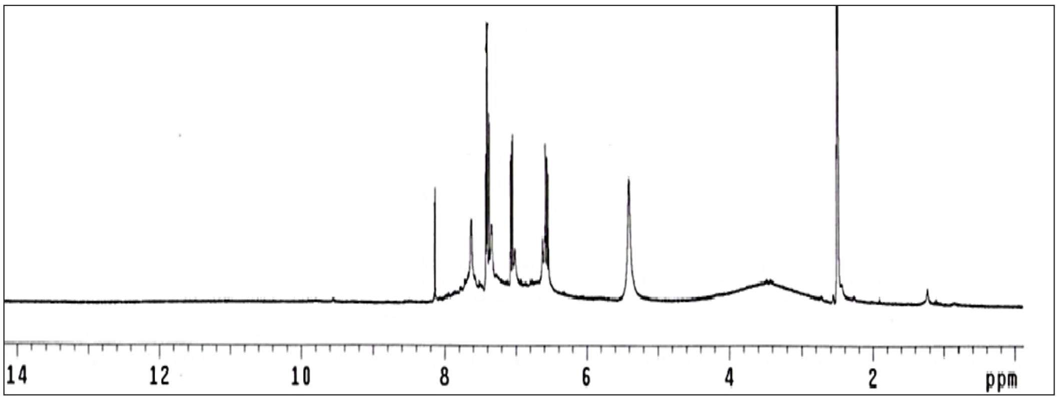

Fig. 2c. ^{1}H-NMR spectroscopy of 1-hydroxy-4-(thiazole-2-yldiazenyl)-2-naphthoic acid ($C_{14}H_9N_3O_3S$) [R_3]

7.13 (4 mL) was added to the sample for R_1 or R_2, respectively. Afterwards, 1.0 mL of (5 × 10^{-3} M) R_1 or 2.0 mL of (1×10^{-3} M) R_2 was added, then 1.0 mL of tween [0.5% (v/v)] or 1.5 mL of CTAB [0.5% (w/v)] was added, respectively. A blank solution with all the chemicals except Hg(II) was equipped and treated as the sample solution. The procedure was performed at room temperature (25°C). As outlined above, the difference in absorbance between the sample and its respective blank was measured at wavelengths of 617 or 633 nm for R_1 and R_2, respectively. On the other hand, a similar procedure was used when the R_3 reagent was used. The optimal order of addition was reagent R_1 (1.0 mL, 1 × 10^{-3} M), metal (1 × 10^{-3} M), buffer (pH 4.97, 4 mL), and surfactant (0.5 mL of tween [0.5% (v/v)]). In addition, at a wavelength of 554 nm, the difference in absorbance between the sample and its corresponding negative was measured (Scheme 1). After sample preparation, the optimal time was determined for each of the three reagents by measuring the absorbance at various intervals(times). Different experimental parameters, such as pH, buffer volume, reagent concentration, surfactant type, concentration, reaction time, and reaction temperature, have been investigated to determine the optimal conditions for the proposed spectrophotometric method.

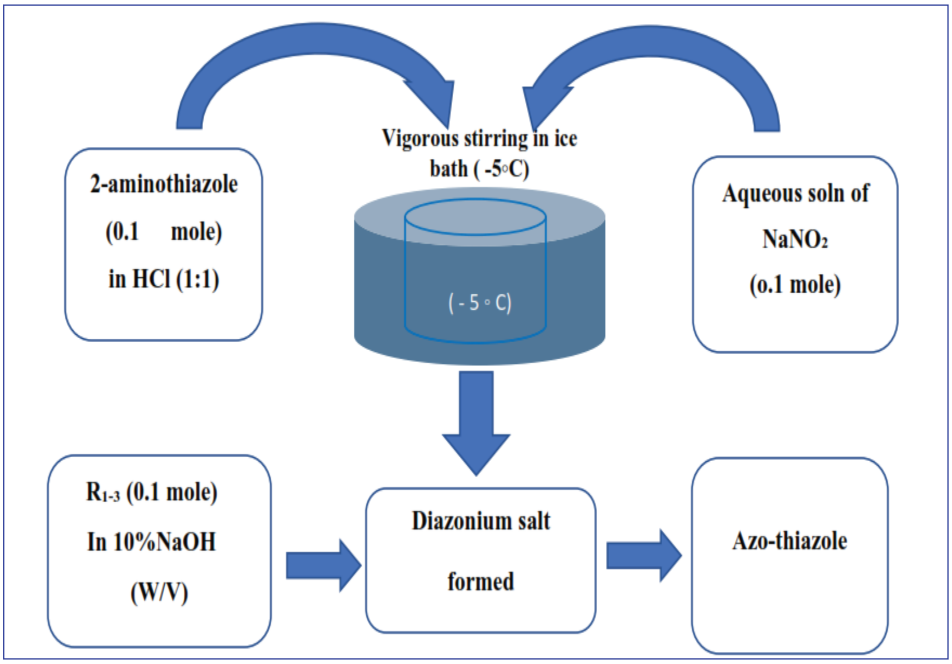

Scheme 1. Procedure for extraction and separation of mercury in water and food samples

2.5. Determination of the molecular structures using the mole ratio method

In the mole ratio procedure illustrated in [28], the Hg(II) ion concentration was held constant at 1 mL of 1.0×10^{-4} M, while that of the ligand was systematically modulated between 0.2 and 2.4 mL of 1.0×10^{-4} M. The absorbance of the prepared solutions was measured at the optimal wavelength under the optimal conditions. The obtained absorbance was then plotted against the mole ratio of ligand, [ligand/metal]. The stoichiometric ratio of the formed stable complexes was extracted from the purified intersections.

2.6. Mercury ion determination in some real samples

The food samples (potatoes, beans, rice, soybeans, and legumes) were dried in an oven at 75°C until their weights stabilized and then ground into a fine powder. In a 100 mL vial, 2.5 g of powder was weighed, and 10 mL of concentrated nitric acid was added. The obtained mixture was digested for 20 minutes in a microwave oven. After allowing the flask to settle, an additional 10 mL of nitric acid and 1 mL of hydrogen peroxide were added, and the mixture was allowed to stand for approximately 25 minutes [29, 30]. The mélange was then re-heated in the microwave for 40 minutes. The digest was then permitted to chill. Finally, 1.0 mL of nitric acid was added and allowed to sit for 10 minutes. The obtained solution was adjusted to a pH range of 8.0 to 9.0 by adding sodium carbonate. The solutions were then processed by the general procedure. Standard addition was used to estimate the recovery percentage and verify the results' precision.

2.7. Determination of mercury (II) in water samples

Water samples were collected around the settlements of Benha and Qalyub in the Al-Qalyubia Governorate. After adding (1:2) (v/v) concentrated H_2SO_4 and concentrated HNO_3 to each filtered water sample in a fume chamber [29, 30], each sample was roughly evaporated to dryness. After chilling, the remaining solution was re-heated with 10.0 mL of double-distilled water. The solution was cooled and neutralized with diluted ammonium hydroxide. The solution was then filtered and transferred precisely into a 25 mL measuring vial. The solutions were then processed by the general procedure.

3. Results and Discussion

Under ideal conditions, mercury (II) creates pink complexes with R_1, R_2, and R_3. Figure 3 shows the absorption spectra of Hg(II)–R_1, Hg(II)–R_2, and Hg(II)–R_3 complexes at maximum values of 617 nm, 633 nm, and 554 nm, respectively. The mercury complexes exhibited a bathochromic shift in their absorption spectra compared to the free reagents, which absorbed at 557 nm, 563 nm, and 477 nm. Studies were conducted to determine the optimal conditions for obtaining high colour intensity and maximal colour development for micro quantification of mercury. Each of the following parameters' effects on colour development was investigated.

3.1. Influence of pH of the medium

Specifically, pH is a crucial factor influencing the chelation of the Hg ion by the proposed reagent molecules. A universal buffer system ranging from 2.7 to 12.0 was utilized to ascertain the optimal pH. As shown in Figure 4, the maximum absorption values for Hg (II) complexes with R_1, R_2, and R_3 were obtained at pH 6.0, 7.13, and 4.97, respectively. In addition, the effect of buffer volume on the analytical peak was investigated between 0.5 and 6 mL (in a total volume of 10 mL). With a buffer volume of 5.0 mL for R_1-Hg (II) and 4.0 mL for both R_2-Hg (II) and R_3-Hg (II) complexes, the highest analytical absorbance was found (Fig.4).

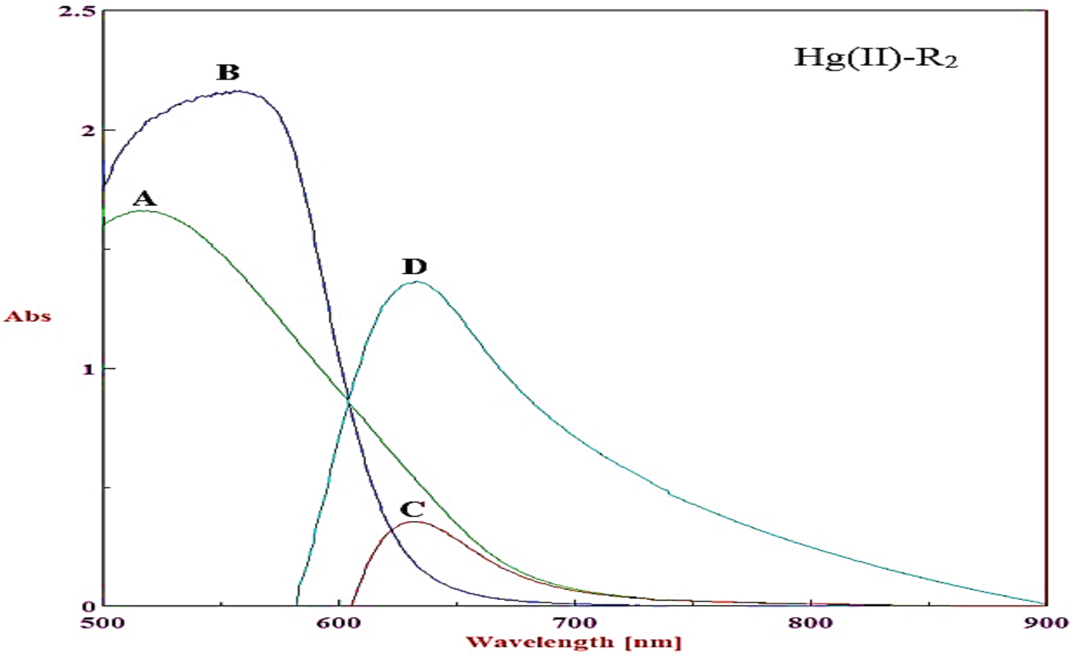

Fig. 3. The absorption spectra of the complex formed between reagents R_2 with Hg(II) where **A**: Spectrum of pure ligand at pH 7.13 against buffer solution as a blank, **B**: Spectrum of a complex solution containing ligand, metal ion and buffer using the same buffer as blank. **C**: Spectrum of solution (B) against ligand and buffer of the same pH as blank and **D**: spectrum of solution (C) in the presence of CTAB.

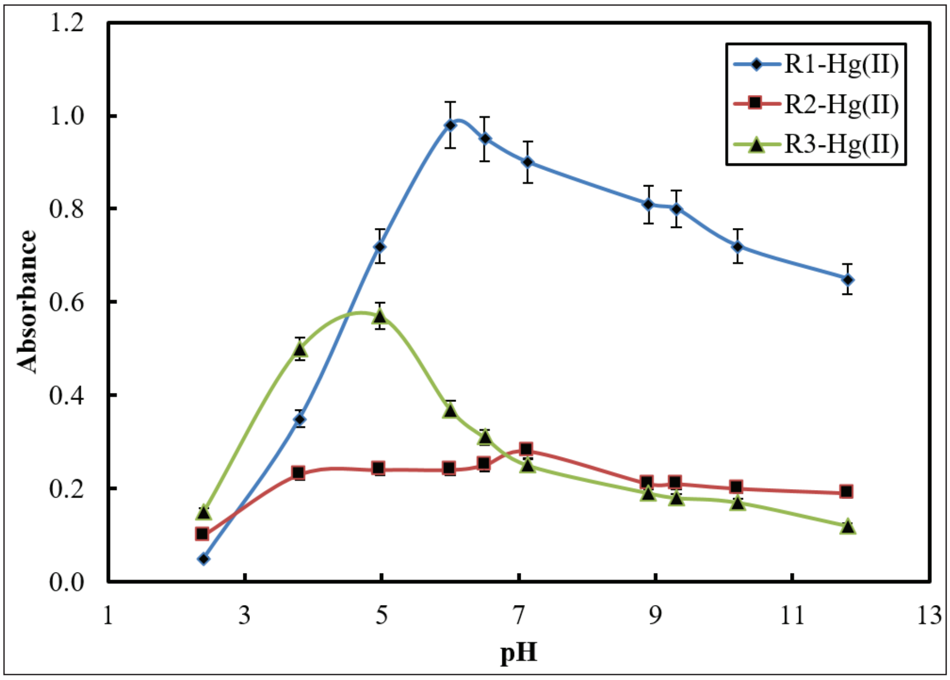

Fig. 4. Effect of pH on the absorption spectra of complexes formed between Hg(II) and the reagents under study.

3.2. Influence of the reagent concentration

The effect of R_1, R_2 and R_3 concentrations on the analytical signal (absorbance) of the formed complexes with Hg(II) is shown in Figure 5. It was clear that for R_1-Hg(II) and R_3-Hg(II) complexes, the absorbance increased with the reagent concentration up to 5 × 10^{-4} M and then suffered from some decrease by increasing the reagent concentration. Therefore, 5 × 10^{-4} M of the reagents R_1 and R_3 was selected as the optimum concentration. However, the absorbance enhanced with R_2 concentration and reached its maximum value at 2 × 10^{-4} M. Consequently, 2 × 10^{-4} M was chosen as the optimal concentration for R_2 reagent.

3.3. Effect of surfactant volume

Tween 80 was the most appropriate solvent for R_1 and R_3, while CTAB was the most suitable for the R_2 complex. The optimal volumes of 0.5% (v/v) Tween-80 were 1 and 0.5 mL for Hg(II) complexes with R_1 and R_3, respectively. For the Hg(II)-R_2 complex, however, the optimal volume for obtaining a high absorbance value was 1.5 mL of 0.5% (w/v) solution.

3.4. Effect of sequence of addition

The effect of the sequence of addition [reagent (R), metal (M), buffer (B), and surfactant (S)] on the formation of complexes was investigated by measuring the absorbance of sample solutions prepared using various addition sequences. The sequence [M.B.R.S.] was the best for Hg(II)-R_1 and Hg(II)-R_2 complexes, while [R.M.B.S.] was the best for reagent R_3. The optimal addition sequence and other optimal conditions for each metal complex are listed in Table 1.

3.5. Effect of temperature and time

The influence of temperature and time on the proposed methodologies was investigated over 25 - 60°C and 2 - 50 min, respectively. The optimal reaction temperature for R_1-Hg(II), R_2-Hg(II), and R_3-Hg(II) complexes was determined to be 25°C. The optimization of the reaction time revealed that all complexes instantly attained their maximum absorbance, except for R_1, which achieved its maximum absorbance 10 minutes after blending. Table 1 presents the optimal time and temperature for other complexes.

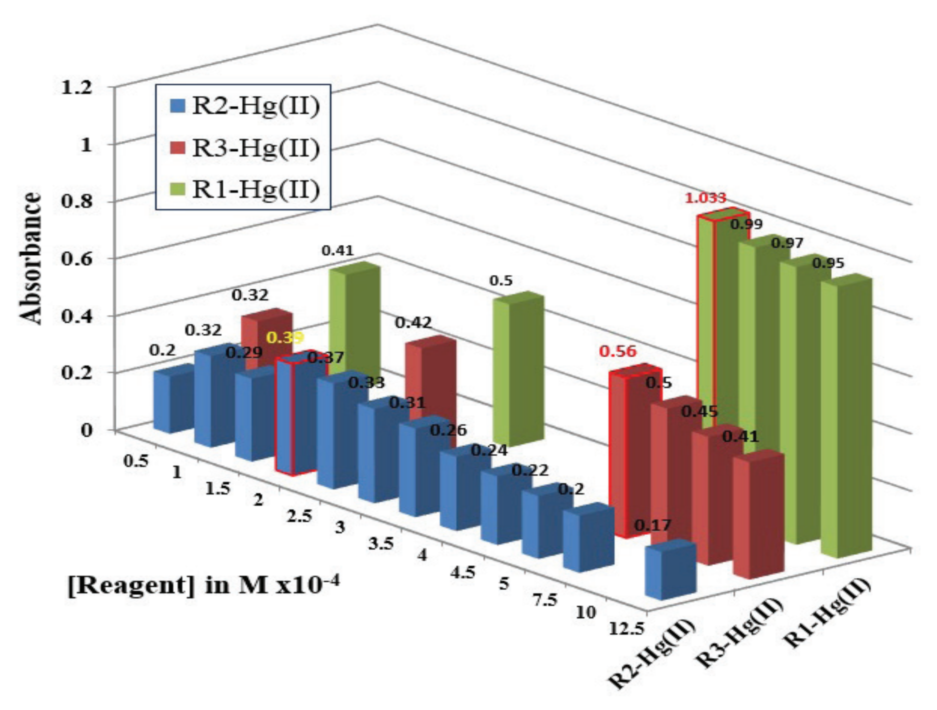

Fig. 5. Effect of reagent concentration on the absorption spectra of complexes formed between Hg(II) and the reagents under study.

Table 1. The optimum condition parameters of Hg(II) with the azo-dye reagents.

Parameters	Hg(II)		
	R_1	R_2	R_3
Type of buffer	Universal	Universal	Universal
Working pH	6.00	7.13	4.97
Volume of buffer, mL	5.00	4.00	4.00
λ_{max}, nm	617	633	554
Reagent's concentration, M	5 x 10^{-4}	2 x 10^{-4}	5 x 10^{-4}
Surfactant used	Tween 80	CTAB	Tween 80
Volume of surfactant, mL	1.0 [0.5% (v/v)]	1.5 [0.5% (w/v)]	0.5 [0.5% (v/v)]
Sequence of addition	M.B.R.S	M.B.R.S	R.M.B.S
Time, min	10	1	1
Stoichiometric ratio (M: L)	(1:1)	(1:1)	(1:1), (1:2)
Stability constant[a]	11.11	7.62	9.54

R: Reagent B: Buffer M: Metal S: surfactant

[a]Stability constant using the molar ratio method

3.6. Stoichiometric ratio

Utilizing a molar ratio routine, the stoichiometry of Hg (II)-R_{1-3} complexes was determined. The optimal absorbance wavelengths for each complex were 617 nm, 633 nm, and 554 nm for the R_1, R_2, and R_3 complexes, respectively. The results indicated that the absorbance curves for R_1 and R_2 complexes attained their maximum value at the same molar ratio (1:1). This demonstrated that a singular complex compound composed of (Hg-R_1) and (Hg-R_2) can be formed from these two systems. The results indicated that the R_3 complex's molar ratio curve attained two maximum values with molar ratios of 1:1 and 1:2 (M: L). This indicated that two complex compounds with the structures (Hg-R_3) and (Hg-$[R_3]_2$) may be present in the method. The calculated stability constants for the formed (1:1) complexes of Hg(II) with the reagents R_1, R_2, and R_3 were 11.11, 7.62, and 9.50, respectively. Due to the high chemical stability of its structure, the Hg(II)-R_1 complex has a high value for its stability constant. This is likely because reagent R_1 contains two electron-donating groups (-OH and -NH_2), which increase the electron cloud on the chelation centre and subsequently increase the stability of this complex relative to the other complexes under investigation.

3.7. Study of the interference

Taking into account the high selectivity provided by the spectrophotometric technique at the selected wavelengths of 617 nm, 633 nm, and 554 nm for Hg(II) chelated with R_1, R_2, and R_3, the tolerance limits for a maximum error of 3.0% were determined. Various interfering ions of varying concentrations were added to a solution containing 2 mg L^{-1} of Hg(II) for investigation. The results demonstrated that common coexisting ions had no appreciable effect on determining analyte ions. Co(II), Ni(II), and Mn(II) species were discovered to cause interference at high tolerance limits between 1 and 20. Therefore, they must be eliminated or disguised prior to mercury analysis. Sodium chloride, sodium borate, and sodium tungstate do not interfere with detecting mercury (II) ions. In addition, the concentrations of these ions are typically deficient in most water and food samples, so these procedures can be used to detect Hg(II) ions in actual water and food samples.

3.8. Spectrofluorometric measurements

As revealed in Figures 6-8, an aqueous solution of R_2 and R_3 with a concentration of 1.0×10^{-5} M displays a vigorous fluorescence intensity at $\lambda_{ex/em}$=507/614 and $\lambda_{ex/em}$=480/610 nm, respectively. Two phenomena were observed for R_2 and R_3. The emission fluorescence peak of free reagents R_3 has suffered from quenching after adding 1.0 × 10-4 M mercury ion. This quenching increased seriously by increasing the concentration of Hg(II). The second observation was shown in the case of reagent $R_{2,}$ where the absence of a new emission peak at λ_{em} 664 nm as shown in Fig. 6. These two observations gave evidence that the formation of nonluminous complexes between R_2, R_3 and Hg(II) [31]. Therefore, these observations can accurately estimate mercury ions using the prepared reagents R_2 and R_3 in this research. It turns out that mercury ion acts as a fluorescent quencher in the case of R_2 and R_3. Experimentally, it was found that the R_1 detector is not given fluorescence intensity, which may be attributed to the structure of R_1 compared to the other R_2 and R_3.

3.9. Analytical characteristics

The calibration graphs for Hg(II) complexes were linear in the concentration range 0.2-10.0 µg mL^{-1} with an excellent correlation coefficient (r^2) of 0.998 for R_1 complex while 0.6-13.0 µg mL^{-1} with (r^2) of 0.998 in case of R_2 complex and 0.9-5.0 µg mL^{-1} with (r^2) of 0.999 in case of R_3 complex. The regression equation may be expressed by

$A = 0.064\ C-0.024$ for Hg(II)-R_1
$A = 0.020\ C+0.001$ for Hg(II)-R_2
$A = 0.028\ C-0.013$ for Hg(II)-R_3

where C is the Hg(II) concentration in a sample solution in µg mL^{-1}, and A is the absorbance. The molar absorptivity and Sandell`s sensitivities of the formed complexes were calculated and exhibited a high sensitivity of the three reagents.

In addition, Table 2 tabulated the analytical parameters for the three proposed methods. The limits of detection and quantification were 51 µg L^{-1} and 156 µg L^{-1} for R_1-complex, 15 µg L^{-1} and 45 µg L^{-1} for R_2 complex, and 26 µg L^{-1} and 785 µg L^{-1} for R_3 complex. These concentration intervals are suitable for the measured [Hg(II)] in four real water and five food samples. The relative standard deviation (RSD) for six replicate measurements of 2 mg L^{-1} of Hg(II) with $R_{1,}$ R_2 and R_3 was obtained at 2.88%, 3.42% and 3.32%, respectively.

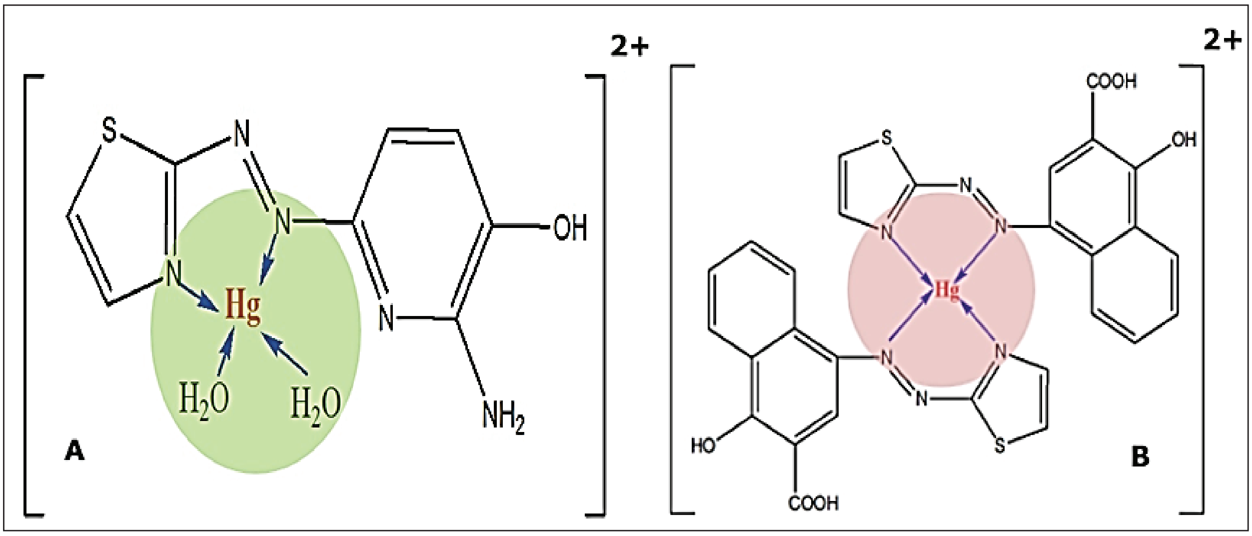

Fig. 6. The proposed structures of the complexes formed between Hg(II) and reagents where A) is (1:2)(Hg(II)-2R_3) and B) is (1:1)(Hg(II)-R_1)

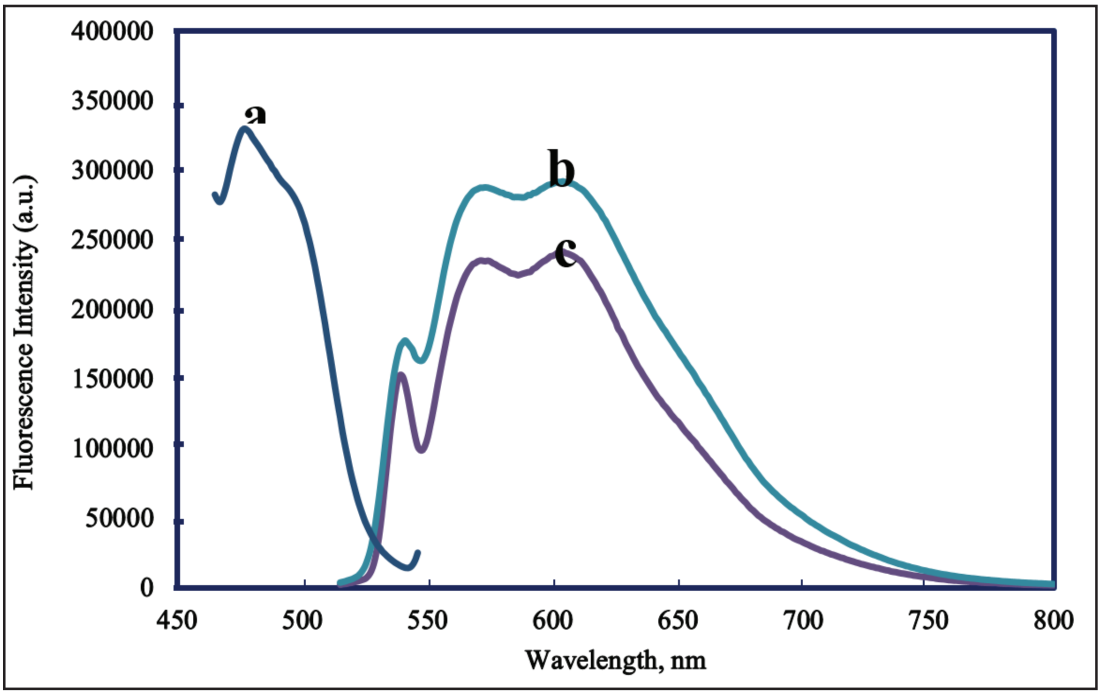

Fig. 7. Fluorescence excitation (a), emission (b) and after addition of 1.0 × 10^{-4} M Hg(II) (c) spectra for R_2 in a universal buffer of pH 7.13, λ_{ex}=507 nm and λ_{em}=614 nm.

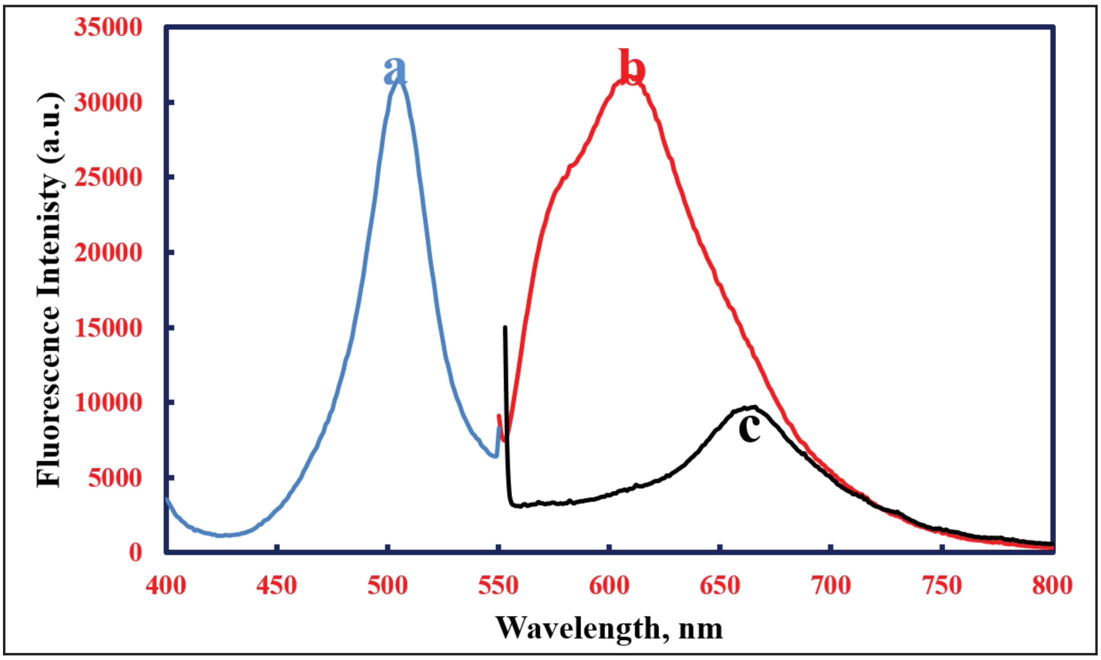

Fig. 8. Fluorescence excitation (a), emission (b) and after the addition of 1.0 × 10^{-4} M Hg(II) (c) spectra for R_3 in the universal buffer of pH 4.97, λ_{ex} = 480 nm and λ_{em} = 610 nm

Table 2. Cumulative data of the analytical conditions for spectrophotometric determination of Hg(II) with different reagents

Parameters	**Hg(II)**		
	R_1	**R_2**	**R_3**
Color	Violet	Violet	Violet
pH	6.00	7.13	4.97
λ_{max} (nm), A curve	557	563	477
λ_{max} (nm), B curve	567	521	496
λ_{max} (nm), C curve	624	632	572
λ_{max} (nm), D curve	617	633	554
Beer's law range (μg mL^{-1})	0.2-10.0	0.6-13.0	0.9-5.0
Ringbom range, (μg mL^{-1})	1.99-6.30	1.99-5	1.99-3.4
Detection limit, (μg mL^{-1})	0.051	0.150	0.26
Quantification limit, (ng mL^{-1})	0.156	0.450	0.785
Standard deviation (SD) (n=6)	0.022	0.007	0.015
RSD (%)	2.88	3.42	3.32
Variance x 10^{-4}	4.80	0.57	2.20
Error %	0.9%	0.31%	0.61%
Slope (b)	0.064	0.020	0.028
Intercept (a)	-0.024	0.001	-0.013
Correlation coefficient, r^2	0.998	0.998	0.999
Molar absorptivity (L mol^{-1} cm^{-1})	12838	4012	5617
Sandell's sensitivity (ng cm^{-2})	0.015	0.050	0.035
Confidence limit	5.2 ± 0.023	4.5 ± 0.007	4.8 ± 0.015

[a]Average of six consecutive measurements.

3.10. Analytical applications

For the availability and reliability of the proposed procedures, the methods were applied to four different real water samples and five different food samples with three azo dyes. The obtained results are similar based on the standard addition method. The accuracy was tested by the Student's *t*-test. According to this test, the calculated *t*-values ranging from 0.23 to 2.27 are less than that of the theoretical value (2.44) at a confidence level of 95 %. In addition, the statistical *F*-test was also applied to compare the precision of the studied methods with another reference method for the determination of trace mercury (UV-visible diffuse reflectance spectroscopy after complexation and membrane filtration enrichment) [32, 33]. The calculated $F_{4,2}$ test value at a 95% confidence level did not exceed the theoretical value (19.2) with a value ranging from (1.10 to 17.77), indicating no significant difference between the performance of the two methods. The results were validated for three dyes in food and water samples in Tables 3-5. Also, the proposed spectrophotometric methods are compared to other published analytical methods in Table 6 [34-40].

Table 3. Determination of mercury ion in environmental samples using reagent R_1

Sample	Added ($\mu g\ mL^{-1}$)	Found ($\mu g\ mL^{-1}$)	Recovery (%)	RSD (%)	The calculated student's t-test and F-values [b]
Potato	-	2.92±0.008	-	0.44	0.60, 4.00
	3	5.98±0.026	102.0	4.42	
	5	7.88±0.023	99.2	4.16	
Beans	-	0.70±0.001	-	4.87	0.41, 2.50
	3	3.66 ±0.008	98.6	0.33	
	5	5.90 ±0.001	104.0	0.13	
Rice	-	6.98±0.011	-	2.36	0.44, 1.56
	1	7.90±0.054	96.5	3.30	
	3	9.85±0.011	95.6	0.17	
Soybean	-	3.35±0.009	-	2.37	2.27, 4.93
	3	6.28±0.018	97.6	4.24	
	5	8.4±0.008	101.0	1.36	
Lentils	-	2.89±0.008	-	0.16	0.23, 1.10
	3	5.85±0.038	98.6	1.42	
	5	7.95±0.009	101.2	1.66	
Tap water	-	0.60±0.001	-	5.60	0.57, 4.93
	3	3.57±0.018	99.0	2.97	
	5	5.56±0.002	99.2	0.60	
Pump	-	1.08±0.057	-	1.11	2.11, 5.50
	3	4.15±0.017	102.4	3.25	
	5	6.02±0.001	98.7	0.27	
Surface water	-	0.70±0.001	-	4.70	0.54, 17.77
	3	3.48±0.001	98.5	0.55	
	5	5.59±0.003	97.8	0.90	
Well	-	0.68±0.001	-	5.50	1.80, 10.00
	3	3.72±0.005	101.3	1.90	
	5	5.61±0.005	98.6	1.20	

[a] The average values and their standard deviations for five replicate measurements.

[b] The tabulated student's *t*-and $F_{(4,2)}$ values are 2.44 and 19.2 for a 95% confidence level and four degrees of freedom

Table 4. Determination of mercury ion in environmental samples using reagent R2

Sample	**Added (µg mL^{-1})**	**Found (µg mL^{-1})**	**Recovery (%)**	**RSD (%)**	**The calculated student's t-test and F-values** [b]
Potato	-	2.97±0.002	-	2.66	2.10, 4.20
	3	6.15±0.003	106.0	1.77	
	5	8.12±0.001	103.0	0.12	
Beans	-	0.67±0.001	-	0.57	1.99, 2.20
	3	3.68±0.001	100.3	0.3	
	5	6.05±0.015	107.6	1.09	
Rice	-	6.94±0.018	-	1.10	0.87, 7.20
	1	7.85±0.016	97.0	2.86	
	3	9.70±0.005	96.0	2.05	
Soybean	-	3.33±0.001	-	0.44	1.97, 5.23
	3	6.35±0.006	100.6	3.90	
	5	8.29±0.001	99.2	0.36	
Lentils	-	2.91±0.001	-	0.67	0.54, 4.57
	3	5.96±0.086	101.6	2.23	
	5	7.92±0.006	100.1	3.14	
Tap water	-	0.57±0.001	-	1.77	1.66, 3.47
	3	3.70±0.003	104.3	4.00	
	5	5.06±0.011	100.6	2.67	
Pump water	-	1.10±0.003	-	1.56	0.89, 2.35
	3	4.25±0.002	105.0	2.25	
	5	6.20±0.009	102.0	2.94	
Surface water	-	0.85±0.003	-	1.66	0.68, 8.21
	3	3.65±0.002	97.6	2.16	
	5	5.62±0.001	95.4	0.13	
Well water	-	0.63±0.001	-	1.84	0.74, 7.89
	3	3.40±0.003	98.4	3.7	
	5	5.62±0.003	99.8	0.26	

[a] The average values and their standard deviations for five replicate measurements.

[b] The tabulated student's t-and $F_{(4,2)}$ values are 2.44 and 19.2 for 95% confidence level and four degrees of freedom

Table 5. Determination of mercury ion in environmental samples using reagent R3

Sample	Added (μg mL^{-1})	Found (μg mL^{-1})	Recovery (%)	RSD (%)	The calculated student's t-test and F-values [b]
Potato	-	2.69±0.009	-	2.65	0.69, 14.2
	1	3.62±0.003	96.5	2.27	
	2	4.65±0.004	98.0	2.50	
Beans	-	0.64±0.002	-	2.85	1.05, 7.21
	1	1.66±0.020	102.0	3.94	
	2	2.62±0.030	99.0	3.35	
Rice	-	1.50±0.004	-	4.20	2.11, 6.51
	1	2.54±0.003	104.0	3.40	
	2	3.48±0.001	99.0	1.06	
Soybean	-	2.66±0.004	-	5.00	1.68, 1.98
	1	3.67±0.007	101.0	3.55	
	2	4.60±0.006	97.0	3.47	
Lentils	-	2.84±0.016	-	1.66	1.58, 4.54
	1	3.87±0.002	103.0	1.05	
	2	4.70±0.007	94.7	4.16	
Tap water	-	0.73±0.002	-	1.43	1.58, 8.94
	1	1.67±0.009	94.5	1.82	
	2	2.71±0.004	99.0	2.84	
Pump	-	1.04±0.006	-	2.50	1.58, 4.54
	1	1.96±0.011	97.3	1.90	
	2	2.97±0.009	96.5	2.75	
Surface water	-	0.77±0.001	-	2.35	1.78, 4.69
	1	1.72±0.006	96.8	1.13	
	2	2.75±0.004	99.0	2.78	
Well	-	0.66±0.003	-	3.20	1.42, 4.57
	1	1.68±0.009	102.0	1.76	
	2	2.70±0.006	102.0	2.45	

[a] The average values and their standard deviations for five replicate measurements.

[b] The tabulated student's t-and $F_{(4,2)}$ values are 2.44 and 19.2 for a 95% confidence level and four degrees of freedom

Table 6. Comparison of the proposed spectrophotometric methods with other analytical methods

Reagent	λ_{max} (nm)	Range of Beer's law (μg mL^{-1})	Remark	Reference
TMK	570	5.0-80.0	Acetate buffer, Triton X-114	[34]
Iodide	330	10.0-400.0	H_2SO_4, Triton X-114	[35]
Rhodamine	556	10-100	pH5.0, Triton X-114	[36]
Dithizone	490	50-500	pH1-3, Triton X-100	[37]
PAN	554	10.0-1000.0	pH9.0, BR buffer, Triton X-114	[38]
TAR	389	500-2500.0	pH8.0, BR buffer, Triton X-114	[38]
Dithizone	490	0.2-4.0	Triton X-100	[39]
R1	617	0.2-10	Tween 80	This Work
R2	633	0.6-13	CTAB	
R3	554	0.9-5	Tween 80	

TMK: Thio-Michler's Ketone

PAN: 1-(2-pyridyl azo)-2-naphthol

TAR: 4-(2-thiazolylazo) resorcinol

4. Conclusions

The proposed paper established three new approaches for the micro-determination of mercury ions. Three prepared azo dyes, R_1, R_2 and R_3, were used as complex reagents. Absorbances of the formed complexes were measured at 617 nm, 633 nm and 554 nm, respectively. The mercury concentrations of 0.2-10.0 μg mL^{-1} for R_1, 0.6-13.0 μg mL^{-1} for R_2 and 0.9-5.0 μg mL^{-1} for R_3 were studied and determined. The detection limits are 50 μg L^{-1} for R_1, 150 μg L^{-1} for R_2 and 260 μg L^{-1} for R_3. The procedures were applied effectively to determine mercury in water and food matrices. The results were in excellent agreement relative to accuracy and precision. The developed methods can be used for the micro-determination of mercury in real samples by the UV-Vis-spectrophotometer without requiring any costly tool.

5. References

[1] M. Salgarello, G. Visconti, L.B. Adesi, Interlocking circumareolar suture with undyed polyamide thread: a personal experience, Aesthetic Plast. Surg., 37 (2013) 1061-1062. https://doi.org/10.1007/s00266-013-0186-1

[2] R. Gürkan, T. Çepken, H.I. Ulusoy, Surfactant-sensitized spectrophotometric determination of Hg (II) in water samples using 2-(2-thiazolylazo)-p-cresol as ligand and cetylpyridinium chloride as cationic surfactant, Turk. J. Chem., 36 (2012) 159-177. https://doi.org/10.3906/kim-1104-32

[3] A. Ghaffari, Performance comparison of neural network training algorithms in modeling of bimodal drug delivery, Int. J. Pharm., 327 (2006) 126-138. https://doi.org/10.1016/j.ijpharm.2006.07.056

[4] M. Saber Tehrani, F. Rastegar, A. Parchehbaf, M. Khatamian, Determination of Pb (II) and Cu (II) by electrothermal atomic absorption spectrometry after preconcentration by a Schiff base adsorbed on surfactant coated alumina, Chin. J. Chem., 24 (2006) 765-769. https://doi.org/10.1002/cjoc.200690145

[5] M.S. Hosseini, H. Hashemi-Moghaddam, Sensitized extraction spectrophotometric determination of Hg (II) with dithizone after its flotation as ion-associate using iodide and ferroin, Talanta, 67 (2005) 555-559. https://doi.org/10.1016/j.talanta.2005.01.010

[6] R.M. Blanco, M. Tagle Villanueva, J. Enrique Sánchez Uría, A. Sanz-Medel, Field sampling, preconcentration and determination of mercury species in river waters, Anal. Chim. Acta, 419 (2000) 137-144. https://doi.org/10.1016/S0003-2670(00)01002-3

[7] A.N. Anthemidis, G. A. Zachariadis, C. E. Michos, J. A. Stratis, Time-based on-line preconcentration cold vapour generation procedure for ultra-trace mercury determination with inductively coupled plasma atomic emission spectrometry, Anal. Bioanal. Chem., 379 (2004) 764-769. https://doi.org/10.1007/s00216-004-2593-2

[8] S. Rıo-Segade, C. Bendicho, Determination of total and inorganic mercury in biological and environmental samples with on-line oxidation coupled to flow injection-cold vapor atomic absorption spectrometry, Spectrochim. Acta Part B: Atom. Spect., 54 (1999)1129-1139. https://doi.org/10.1016/S0584-8547(99)00052-X

[9] Q. Tu, J. Qvarnström, W. Frech, Determination of mercury species by capillary zone electrophoresis-inductively coupled plasma mass spectrometry: a comparison of two spray chamber–nebulizer combinations, Analyst, 125 (2000) 705-710. https://doi.org/10.1039/A908880F

[10] M. Bacci, D. Magrini, M. Picollo, M. Vervat, A study of the blue colors used by Telemaco Signorini (1835–1901), J. Cult. Herit., 10 (2009) 275-280. https://doi.org/10.1016/j.culher.2008.05.006

[11] V. Fernández-Pérez, L.E. Garcia-Ayuso, M. L. de Castro, Focused microwave Soxhlet device for rapid extraction of mercury, arsenic and selenium from coal prior to atomic fluorescence detection, Analyst, 125 (2000) 317-322. https://doi.org/10.1039/A905217H

[12] S. Suresha, M. Fawaz Silwadi, A. Ahmed Syed, Sensitive and selective spectrophotometric determination of Hg (II), Ni (II), Cu (II) and Co (II)

using iminodibenzyl and 3-chloroiminodibenzyl as new reagents and their applications to industrial effluents and soil samples, Int. J. Environ. Anal. Chem., 82 (2002) 275-289. https://doi.org/10.1080/03067310290024300

[13] C.C. MagalhŃes, F. Krug, A.H. Fostier, Direct determimnation of mercury in sediments by atomic absorption spectrometry, J. Anal. At. Spectrom., 12 (1997) 1231-1234. https://doi.org/10.1039/A701870C

[14] D. C. Nambiar, N. N. Patil, V.M. Shinde, Liquid-liquid extraction of mercury (II) with triphenylphosphine sulphide: Application to medicinal and environmental samples, Fresenius J. Anal. Chem., 360 (1998) 205-207. https://doi.org/10.1007/s002160050675

[15] K.L. Cheng, K. Ueno, T. Imainura, Handbook of organic analytical reagents, CRC Press, 1982. https://library.unitech.ac.pg/cgi-bin/koha/opac-detail.pl?biblionumber=25868

[16] H.Z. Mousavi, M.M. Eskandari, A.A. Miran-Beigi, Ultra-trace arsenic and mercury speciation and determination in blood samples by ionic liquid-based dispersive liquid-liquid microextraction combined wif flow injection-hydride generation/cold vapor atomic absorption spectroscopy, Chem. Papers, 69 (2015) 779-790. https://doi.org/10.1515/chempap-2015-0086

[17] M. Osanloo, M. Ghazaghi, H. Hassani, Validation of a new and cost-effective method for mercury vapor removal based on silver nanoparticles coating on micro glassy balls, Atmos. Pollut. Res., 8 (2017) 359-365. https://doi.org/10.1016/j.apr.2016.10.004

[18] A. Rouhollahi, Determination of mercury concentration in the air of dental clinics and the urines of their personnel with cold vapor atomic absorption spectrometry, Iran. J. Toxicol., 2 (2009) 287-291 http://ijt.arakmu.ac.ir/article-1-66-en.html

[19] M. Osanloo, O. Qorban Dadrass, Using silver nano particles for sampling of toxic mercury vapors from industrial air sample, J. Health Safe. Work, 4 (2014) 21-30. http://jhsw.tums.ac.ir/article-1-5119-en.html

[20] F. Golbabaei, A. Vahid, A. Faghihi Zarandi, A novel nano-palladium embedded on the mesoporous silica nanoparticles for mercury vapor removal from air by the gas field separation consolidation process, Appl. Nanosci., 12 (2022) 1667-1682. https://doi.org/10.1007/s13204-022-02366-0

[21] F. Golbabaei, H. Hassani, F. Eftekhar, M.J. Kian, Occupational exposure to mercury: air exposure assessment and biological monitoring based on dispersive ionic liquid-liquid microextraction, Iran. J. Public Health, 43 (2014) 793-799. http://ijph.tums.ac.ir

[22] M. Bagheri Hosseinabadi, N. Khanjani, M.D. Mobarake, Neuropsychological effects of long-term occupational exposure to mercury among chloralkali workers, Work, 66 (2020) 491-498. https://doi.org/ 10.3233/WOR-203194

[23] F Golbabaei, A Ebrahimi, A Koohpaei, A Faghihi-Zarandi, Single-walled carbon nanotubes (SWCNTs), as a novel sorbent for determination of mercury in air, Global J. Health Sci., 8 (2016) 273-280. https://doi.org/10.5539/gjhs.v8n7p273

[24] M. Habibnia, A. Rashidi, A.F. Zarandi, M.D. Mobarake, Simultaneously speciation of mercury in water, human blood and food samples based on pyrrolic and pyridinic nitrogen doped porous, graphene nanostructure, Food Chem., 403 (2023) 134394. https://doi.org/10.1016/j.foodchem.2022.134394

[25] F. Golbabai, A. Ebrahimi, Performance comparison survey of multi-walled and single-walled carbon nanotubes for adsorption and desorption of mercury vapors in the air, Iran. Occup. Health, 10 (2013) 21-31. https://espace.library.uq.edu.au/view/UQ:9d03f02

[26] A. I. Vogel, Á textbook of quantitative inorganic analysis, Longman, London, 1978. https://archive.org/details/vogelstextbookof0000voge

[27] A. B. Fowler, R. K. Zalups, Mercury, Chapter 22, Handbook on the Toxicology of Metals, Academic press, fifth Edition, Volume II (2022) 539-599. https://doi.org/10.1016/B978-0-12-822946-0.00020-9

[28] J.H. Yoe, A. Jones, Colorimetric determination of iron with disodium-1, 2-dihydroxybenzene-3, 5-disulfonate, Am. Chem. Soc., 16 (1944)111-115. https://doi.org/10.1021/i560126a015

[29] A. Keramat, R. Zare-Dorabei, Ultrasound-assisted dispersive magnetic solid phase extraction for preconcentration and determination of trace amount of Hg (II) ions from food samples and aqueous solution by magnetic graphene oxide (Fe_3O_4@ GO/2-PTSC): Central composite design optimization, Ultrason. Sonochem., 38 (2017) 421-429. https://doi.org/10.1016/j.ultsonch.2017.03.039

[30] M.H. Mashhadizadeh, Solid phase extraction of trace amounts of silver, cadmium, copper, mercury, and lead in various food samples based on ethylene glycol bis-mercaptoacetate modified 3-(trimethoxysilyl)-1-propanethiol coated Fe_3O_4 nanoparticles, Food Chem.,151 (2014) 300-305. https://doi.org/10.1016/j.foodchem.2013.11.082

[31] M.A. Kassem, I. I. Althagafi, Sensitive spectrofluorimetric study of the interaction between Europium (III) and 1, 2-Phenylenebis (azan-1-yl-1-ylidene) bis (methan-1-yl-1-ylidene) diphenol Schiff Base, J. Fluorescence, 26 (2016) 2087-2093. https://doi.org/10.1007/s10895-016-1903-3

[32] Y.G. Yin, Dithizone-functionalized solid phase extraction–displacement elution-high performance liquid chromatography–inductively coupled plasma mass spectrometry for mercury speciation in water samples, Talanta, 81 (2010) 1788-1792. https://doi.org/10.1016/j.talanta.2010.03.039

[33] L. Li, Transformation of cefazolin during chlorination process: products, mechanism and genotoxicity assessment, J. Hazard. Mater., 262 (2013) 48-54. https://doi.org/10.1016/j.jhazmat.2013.08.029

[34] A.Niazi,T.Momeni-Isfahani,Spectrophotometric determination of mercury in water samples after cloud point extraction using nonionic surfactant Triton X-114, J. Hazard. Mater., 165 (2009) 1200-1203. https://doi.org/10.1016/j.jhazmat.2008.09.091

[35] A. Afkhami, T. Madrakian, H. Siampour, Flame atomic absorption spectrometric determination of trace quantities of cadmium in water samples after cloud point extraction in Triton X-114 without added chelating agents, J. Hazard. Mater., 138 (2006) 269-272. https://doi.org/10.1016/j.jhazmat.2006.03.073

[36] M. Pandurangappa, K.S. Kumar, Micellar mediated trace level mercury quantification through the rhodamine B hydrazide spirolactam ring opening process, Anal. Methods, 3 (2011) 715-723. https://doi.org/10.1039/C0AY00693A

[37] M. Garrido, M.S. Di Nezio, A.G. Lista, M. Palomeque, B.F. Band, Cloud-point extraction/preconcentration on-line flow injection method for mercury determination, Anal. Chim. Acta, 502 (2004) 173-177. https://doi.org/10.1016/j.aca.2003.09.070

[38] H. I. Ulusoy, R. Gürkan, S. Ulusoy, Cloud point extraction and spectrophotometric determination of mercury: species at trace levels in environmental samples, Talanta, 88 (2012) 516-523. https://doi.org/10.1016/j.talanta.2011.11.026

[39] M. Arjomandi, A review: analytical methods for heavy metals determination in environment and human samples, Anal. Methods Environ. Chem. J., 2 (2019) 97-126. https://doi.org/10.24200/amecj.v2.i03.73

[40] H.B. Singh, B. Kumar, R.L. Sharma, M. Katyal, Direct spectrophotometric determination of trace amounts of mercury (II) in aqueous media as its dithizonate complex in the presence of a neutral surfactant, Analyst, 114 (1989) 853-855. https://doi.org/10.1039/AN9891400853

Anal. Methods Environ. Chem. J. 6 (4) (2023) 37-51

AMECJ

Research Article, Issue 4
Analytical Methods in Environmental Chemistry Journal
Journal home page: www.amecj.com/ir

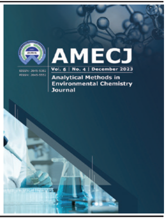

Removal and determination of carbon monoxide based on copper oxide immobilized on Zeolite 13X Nanocatalyst by catalytic oxidation process and gas flow analyzer

Bahar Parsazadeh[a], Hasan Asilian Mahabadi [a,*], and Niloofar Damyar[b]
[a] *Department of Occupational Health, Faculty of Medical Sciences, Tarbiat Modares University, Tehran, Iran*
[b] *Department of Occupational Health, Damghan School of Public Health, Semnan University of Medical Sciences, Semnan, Iran*

ARTICLE INFO:
Received 2 Aug 2023
Revised form 14 Oct 2023
Accepted 3 Nov 2023
Available online 28 Dec 2023

Keywords:
Carbon monoxide,
Copper Oxide nanoparticles,
Zeolite 13X,
Catalytic oxidation,
Response surface methodology,
Central composite design

ABSTRACT

Carbon monoxide is one of the main air pollutants, mainly produced from the incomplete combustion of fossil fuels. This study aims to oxidize carbon monoxide by copper oxide nanoparticles immobilized on zeolite13X substrate**.** The present investigation was conducted to determine the effect of carbon monoxide concentration parameters (in the range of 200-1400 ppm) and reaction temperature (in the range of 100-500 °C) on the efficiency of carbon monoxide conversion by CuO/Zeolite 13X nanocatalyst. The design of the experiment and the determination of the number of experiments were analyzed using the central composite design method, and the statistical test of analysis of variance was done using the response surface method. Also, the structural and morphological characteristics of the nanocatalyst were investigated using BET, BJH, FE-SEM, EDX, and XRF tests. The results show that CuO/Zeolite 13X nanocatalyst efficiently oxidizes carbon monoxide. The highest conversion efficiency of 82.6% was obtained at a temperature of 400 °C and a carbon monoxide concentration of 500 ppm as the optimal conditions. According to the EDX test results, copper oxide nanoparticles with a weight percentage of 5.9% were loaded on the Zeolite 13X substrate. Design Expert11 software reduced the cubic model with an R_2 coefficient of 0.98.

1. Introduction

According to the World Health Organization (WHO), 7 million deaths occur yearly due to air pollution [1]. Carbon monoxide is a colourless, odourless, and non-irritating gas mainly produced from the incomplete combustion of carbonaceous materials (coal, diesel, natural gas, oil, propane, and so forth) [2]. Industries and vehicles are the most important sources of this gas emission [3]. Carbon monoxide is a poisonous gas for humans and animals and also has adverse effects on the environment [2] Regarding the concentration

---

*Corresponding Author: Hasan Asilian Mahabadi
Email: asilian_h@modares.ac.ir
https://doi.org/10.24200/amecj.v6.i04.259

of carbon monoxide in the exhaust air of Iran's industries, several investigations have been carried out, for example, in 2010, Junadi et al. investigated the exhaust of waste incinerators of several hospitals in Hamedan city, and the highest concentration of carbon monoxide reported as 1041 ppm, which 10.4 times the standard of the Environmental Organization in 2002 [4]. Also, in another study, Guderzi et al. investigated the pollutants from cement industries in Lorestan city, and based on the results, the highest concentration of carbon monoxide is related to winter and spring seasons and is equal to 630 ± 53.04 and 2378 ± 76 ppm, respectively, which are higher than the permissible exposure limit [5]. About 95% of the absorbed carbon monoxide is easily combined with hemoglobin to form carboxyhemoglobin. Complications such as muscle paralysis, coma, cardiovascular complications, and eventual death occur when the percentage of carboxyhemoglobin increases by more than 50%. Also, nano-palladium embedded on the mesoporous silica nanoparticles was used for CO and mercury removal from air [2, 6]. Hence, controlling and reducing the concentration of carbon monoxide is essential in maintaining public health. Oxidation of carbon monoxide to carbon dioxide is a practical and straightforward way to control this pollutant [7]. Using heterogeneous catalysts to oxidate various chemical compounds is among the leading technologies in advanced environmental science and engineering [8-10]. Many studies have reported that platinum group metals (PGM), including Platinum (Pt), Palladium (Pd), Radium (Rd), and Iridium (Ir), have high catalytic activity for carbon monoxide oxidation [11, 12]. However, their use as catalysts is limited due to challenging problems such as low natural abundance, high cost, and sulphur poisoning [13]. Therefore, transition metals such as copper [14, 15], nickel [16, 17] and cobalt [18] and their combinations have been considered for carbon monoxide oxidation due to their high natural abundance and high stability [13, 14, 19, 20] To date, many studies have been performed to investigate the catalytic activity of nanocatalysts. According to previous studies, metal nanoparticles used as catalysts can help improve the reaction efficiency due to their high surface-to-volume ratio, specific surface area, and high chemical and thermal resistance [21, 22]. Hence, attempts have been made to place active nanostructures on mesoporous supports to increase the stability of nanocatalysts and prevent them from c. So far, various porous materials, such as metal oxides, diatomite, zeolites, activated carbon, and alumina, have been studied to make copper oxide catalysts [23-27]. Zeolites are available in synthetic and natural forms and generally consist of a basic structure consisting of an aluminosilicate framework and a quadrilateral set of silicate cations (SiO_4^+) and aluminum (Al^{3+}) cations surrounded by four oxygen anions. Synthetic zeolites have a higher surface area, more pore volume, and no impurities compared to natural zeolites [28, 29]. NaX faujasite (with the brand name of zeolite 13X) is an alkaline metal aluminosilicate with the sodium form of zeolite X [30, 31]. However, the investigation of the catalytic activity of copper oxide nanoparticles immobilized on zeolite 13X was not found by our research team.

This study aimed to catalyze carbon monoxide oxidation by zeolite 13X stabilized copper oxide nanocatalyst. The CCD central composite design method (a subset of the RSM response surface method) and the Design-Expert software version 11 were used to design, model, and optimize the experiments.

2. Experimental

2.1. Catalyst preparation

This study synthesized the copper oxide using aqueous copper acetate salt $Cu(OAc)_2{\cdot}H_2O$ by co-precipitation. Previous research reported 4-5% by weight of copper oxide fixed on the support as the optimal catalyst [20, 32]. Accordingly, CuO/Zeolit13X nanocatalyst with 4% by weight was investigated in this study. To make a copper oxide nanocatalyst of 4% by weight, 2.8 g of the aqueous copper acetate salt ($Cu(OAc)_2{\cdot}H_2O$) was added to 100 ccs of distilled water to reach a clear blue solution. The solution temperature was adjusted to 80 °C, and

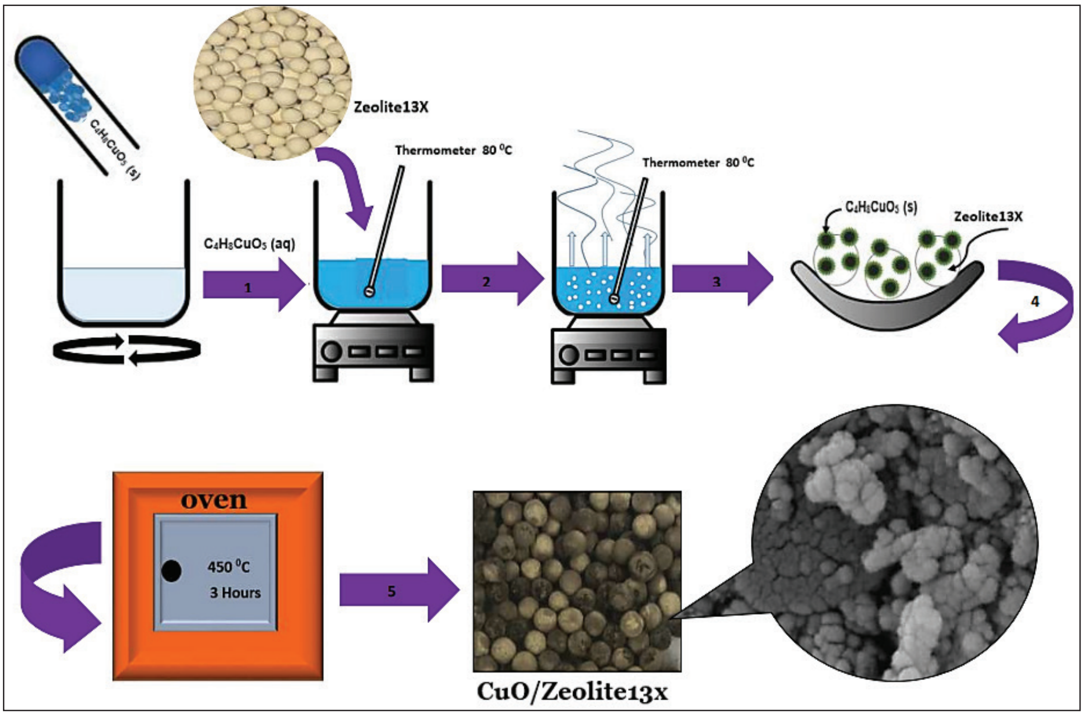

Fig. 1. Schematic view of the manufacturing steps of CuO/Zeolite13X nanocatalyst

20 g of zeolite 13X was added. The suspension was then placed on a mixer and gently stirred until all the water in the suspension was evaporated. Next, zeolite pellets impregnated with copper acetate salt were calcined at 450 °C for 3 hours (Fig.1).

2.2. Characterization

Elemental analysis of zeolite13x was performed by X-ray fluorescence test (XRF) using an XRF device (model PW 2404 Philips Company) with the LIO method (loss-on-ignition) on pressed powders. The Brunauer-Emmett-Teller (BET) and Barrett-Joyner-Halenda (BJH) tests determined specific surface area, pore volume, and pore size. The tests were performed with the physical adsorption of N2 at -196 °C using a micrometric TriStar II 3020 analyzer. Field Emission Scanning Electron Microscope (FE-SEM) and Energy-dispersive X-ray spectroscopy (EDX) examined the morphology of the catalyst and quantitative and elemental identifications appended with FE-SEM, respectively. Using FE-SEM analysis, high-resolution images of the catalyst surface were provided with a magnification of 5,000 x and an operating voltage of 20 kV.

2.3. Procedure based on catalytic activity and gas flow analyzer

Catalytic activity tests of copper oxide nanocatalysts were performed in a fixed bed reactor (quartz glass tube with an inner diameter of 13 mm and a catalyst length of 20 mm were used) at the atmospheric pressure and with a 1 liter per minute flow rate. As shown in Figure 2, a carbon monoxide cylinder with a purity of 99.99% was used as the main gas, and purified ambient air (silica gel and soda-lime) was used as the carrier gas. The concentration of carbon monoxide was adjusted by needle valves, rotameters, and flowmeters with control valves in the path before the reactor, and its amount was determined both before and after the reactor (reactor outlet) by a continuous gas flow analyzer (MRU Vario Plus, Germany) with 10-ppm accuracy which was calibrated before all tests. This device is Suitable for industrial applications using combined infrared (NDIR) technology and electrochemical sensors for maximum versatility. It can measure 9 gases, including O_2, CO, NO, NO_2, NOx, SO_2, CO-high, CO-very high, H_2S or H_2, CH_4 or C_3H_8. This device can measure carbon monoxide, carbon dioxide, and oxygen simultaneously. To perform the tests, the supported copper oxide nanocatalyst was placed in an oven at 150 °C for 2 hours with the aim of dehumidifying, and then 1 g of it was placed in a reactor (Fig.3). Refractory fibreglass was also used to hold the catalysts in place. The conversion efficiency of carbon monoxide to carbon dioxide was calculated by Equation 1.

$$\eta\% = \frac{C_{in} - C_{out}}{C_{in}} \times 100$$

(Eq. 1)

In this equation: C_{in}: input concentration (ppm), C_{out}: output concentration (ppm), and η: efficiency in percentage.

2.4. Experimental design and statistical analysis

To achieve maximum efficiency, there is a need to optimize the process variables. Traditional and old optimization methods are done by considering the effect of a parameter on the process at a certain time. In recent years, to overcome the shortcomings, the

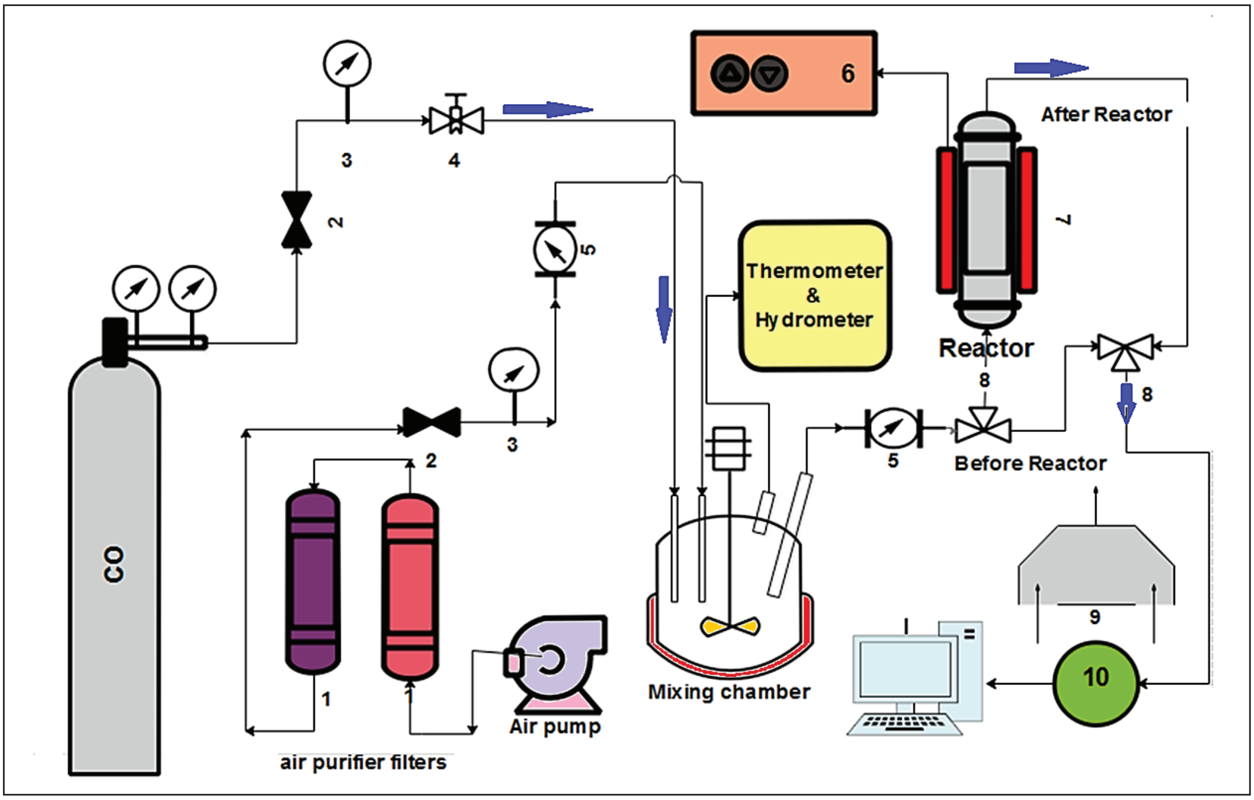

Fig. 2. Schematic design of the test set-up, 1: Gas valves, 3: Pressure measurement, 4: Needle valve, 5: Flowmeter, 6: Heat control thermostat, 7: Furnace, 8: Three-way valve, 9: Vent, 10: Gas analyzer

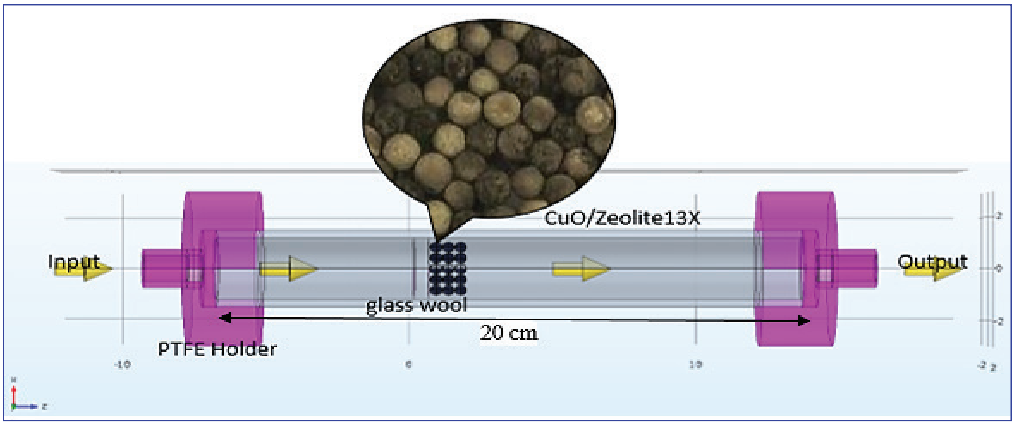

Fig. 3. The packed CuO/Zeolite 13X reactor

Table 1. The experimental range and levels of the factors in the CCD

Factor	Name	Units	Type	Minimum	Maximum	Coded low	Coded high	Mean
A	Temperature	°C	Numeric	100.00	500.00	-1 ↔ 200.00	+1 ↔ 400.00	300.00
B	Concentration	ppm	Numeric	200.00	1400.00	-1 ↔ 500.00	+1 ↔ 1100.00	800.00
C	packing type	Categoric		Zeolite13X	CuO/Zeolite13X			Levels: 2

RSM response surface method, which is a powerful optimization method, has been widely used [33-35]. This method is based on mathematical and statistical techniques that find optimal conditions by understanding the effects of various factors and their interaction on the response. CCD (Central Composite Design) is one of the most common RSM methods [36] [37]. As shown in Table 1, temperature variables and carbon monoxide concentration in 5 levels α, -1,0, +α, +1 were examined. Also, the qualitative catalyst type variable was studied in CuO/Zeolite 13X and Zeolite 13X (uncoated catalyst base). After carrying out the carbon monoxide oxidation tests, the effect of each independent variable (carbon monoxide concentration and temperature) on the response and their relationship with each other was obtained by Equation 2 [38].

$$Y = \beta 0 + \sum_{i=1}^{k} \beta i\, Xi + \sum_{i=1}^{k} \beta ii\, Xi^2 + \sum_{i=1}^{k} \sum_{j=1}^{k} \beta ij\, Xi\, Xj + eij \quad \text{(Eq.2)}$$

In this formula, Y is the predicted response, β0 is a constant coefficient, βi is the linear effects, βii squared effect, βij interaction, εij random error, Xi and Xj are the temperature and concentration of carbon monoxide (independent variables), respectively.

3. Results and Discussion

3.1. Statistical analysis of the catalytic conversion of CO

This study aimed to determine the influential factors on carbon monoxide conversion efficiency (CEC), study the interaction of variables, and determine their optimal values. Table 1 lists the variables under consideration, which were reaction temperature (A) and CO concentration (B) under two reactors' conditions (reactor packed with Zeolite13X (uncoated base) and reactor packed with CuO/Zeolite13X nanocatalyst). The minimum and maximum values of the main variables (CO gas concentration and reaction temperature) were selected according to the reported conditions of the exhaust gas concentration of many industries and refineries, according to the values given in Table 1. Firstly, CO adsorption by uncoated Zeolite 13X pellets was investigated to ensure that they had no adsorption and catalytic effects. The central composite design (CCD) method in 5 levels has been used to obtain logical results in this research. To evaluate the effect of variables, the reaction temperature (A), carbon monoxide gas concentration (B) and type of packed reactor (C), 26 tests were designed using the CCD method, and the results of each test are given in Table 2.

3.2. Model matching and statistical analysis

The experimental data from 26 runs defined by the CCD were analyzed to achieve significant and insignificant effects of each variable and their interactions. Then, the best regression model will be obtained to predict the carbon monoxide conversion efficiency of the reactor packed with CuO/Zeolite 13X and zeolite 13X. ANOVA results for the selected reduced cubic model, which can predict the response (carbon monoxide conversion efficiency), are given in Table 3. According to the obtained results (Table 2), the carbon monoxide conversion efficiency for the reactor packed with Zeolite 13X is 0.11-7.43%, which is significantly higher than that of the reactor packed with CuO/Zeolite 13X nanocatalyst. In this study, the maximum carbon monoxide conversion efficiency is achieved by CuO/Zeolite 13X nanocatalyst (92.96%), which is 12.5 times greater than that of the reactor packed with Zeolite 13X. Therefore, it can be concluded that Zeolite 13X is catalytically inactive, which is consistent with other studies conducted in this area. To achieve the carbon monoxide conversion efficiency (CEC) regression model, according to the results obtained from 26 tests, Equations 3 and 4 were created by Design-Expert software version 11.

Table 2. Results of CO conversion efficiency experiments

Run	A: Temperature (°C)	B: CO concentration (ppm)	C: Catalyst type	(%) $\eta_{predicted}$	(%) η_{actual}
1	300	800	ZeoliteX13	3.74	3.08
2	400	1100	ZeoliteX13	5.16	5.70
3	100	800	CuO/ZeoliteX13	2.31-	6.77
4	300	800	ZeoliteX13	3.74	3.10
5	300	200	ZeoliteX13	5.47	5.76
6	300	800	CuO/ZeoliteX13	46.85	41.57
7	300	1400	ZeoliteX13	2.02	2.10
8	300	800	ZeoliteX13	3.74	2.77
9	500	800	ZeoliteX13	8.31	9.10
10	300	800	ZeoliteX13	3.74	2.68
11	400	1100	CuO/ZeoliteX13	66.84	78.89
12	400	500	CuO/ZeoliteX13	76.02	82.60
13	200	500	CuO/ZeoliteX13	26.86	22.10
14	300	800	ZeoliteX13	3.74	3.13
15	300	800	CuO/ZeoliteX13	46.85	41.20
16	200	500	ZeoliteX13	2.32	2.50
17	300	1400	CuO/ZeoliteX13	37.67	38.02
18	200	1100	CuO/ZeoliteX13	17.68	16.81
19	300	800	CuO/ZeoliteX13	46.85	42.85
20	500	800	CuO/ZeoliteX13	96.01	92.96
21	100	800	ZeoliteX13	0.82-	0.11
22	400	500	ZeoliteX13	6.89	7.43
23	300	800	CuO/ZeoliteX13	46.85	42.05
24	200	300	CuO/ZeoliteX13	56.03	61.06
25	200	1100	ZeoliteX13	0.60	1.20
26	300	800	CuO/ZeoliteX13	46.85	42.20

The following equations can predict the CEC at the levels of the original units determined for each factor.

$$R\%\ CuO/Zeolite13X = +17.19889 +0.112493A-0.054183B+0.000013AB +0.000205A^2+0.000022B^2$$

(Eq.3)

$$R\%\ Zeolite13X = +3.32835 + 0.000295A-0.006330B-3.58333E\text{-}06AB + 0.000042A^2 + 2.83118E\text{-}06B^2$$

(Eq.4)

Analysis of variance (Table 3) showed that the selected reduced cubic model with P-values of less than 0.05 and a 95% confidence interval is suitable for predicting CEC. The factors of reaction temperature (A), CO concentration (B), packed reactor type (C), and AC interaction) have P-values less than 0.05 and are significant factors in carbon monoxide conversion efficiency. This model is robust, with more than 99.99% accuracy. Based on the statistical results, the values predicted by the model with the results of regression experiments are equal to 0.98. Also, the R-square (R^2) and adjusted R-squared (adj, R^2) are equal to 0.98 and 0.97, respectively, with a difference of less than 0.2, indicating the model's suitability. The precision also shows the signal-to-noise ratio, which is 31.54 for the prediction model, which is more than four and is desirable. Also, the standard deviation values (SD) and the coefficient of variation (CV) equal 68.4 and 18.50, respectively. Based on these results, the predicted values and the values obtained from the experimental tests for the CO conversion efficiency response have good regression, which indicates that this model can be used with good reliability to predict the response. Parameters A and B represent the actual reaction temperature and CO concentration values, respectively. Positive regression coefficients indicate a positive linear effect, and negative regression coefficients indicate a negative linear effect on carbon monoxide conversion efficiency. It should be noted that the P-value determines the effect of each parameter. For significant parameters, the smaller the P-value, the greater the effect of that parameter on the response, and if the P-values are the same, the F-value should be considered; the higher this value is, the greater the effect of the parameter on the response. The significant parameters in this study based on their importance in carbon monoxide conversion efficiency are C > A > AC > B. The comparison of the predicted values obtained from the selected model against the actual values obtained from the experimental tests for the intended response is shown in Figure 4. The scatter of points around the diagonal line (Figure 4) shows a good correlation between the experimental data and the predicted values and, consequently, the model's strength. Based on these results, the predicted values and the values obtained from experiments for the CO conversion efficiency response showed a good regression, revealing that this model can be used with good reliability to predict the response.

Table 3. ANOVA for Reduced Cubic model

Source	Sum of Squares	df	Mean Square	F-value	p-value
Model	19803.02	11	1800.27	82.23	< 0.0001
A-Temperature	4330.10	1	4330.10	197.78	< 0.0001
B-Concentration	178.38	1	178.38	8.15	0.0127
C-Type of reactor	4647.60	1	4647.60	212.28	< 0.0001
AB	0.1653	1	0.1653	0.0076	0.9320
AC	2982.63	1	2982.63	136.23	< 0.0001
BC	83.37	1	83.37	3.81	0.0713
A^2	69.88	1	69.88	3.19	0.0957
B^2	56.45	1	56.45	2.58	0.1306
ABC	0.5050	1	0.5050	0.0231	0.8815
A^2C	30.17	1	30.17	1.38	0.2600
B^2C	33.51	1	33.51	1.53	0.2364

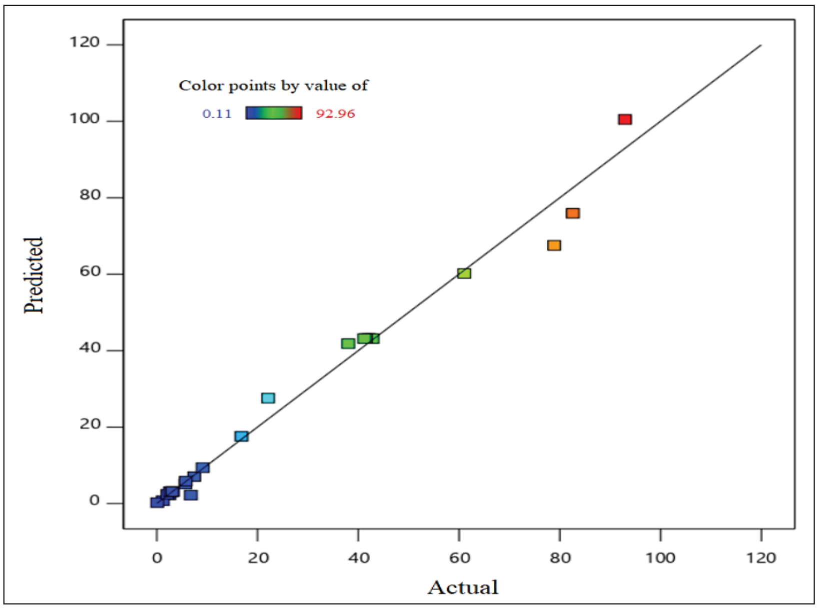

Fig. 4. Comparison of values predicted by the model and obtained from experimental tests

3.3. Effect of carbon monoxide concentration and reaction temperature on carbon monoxide conversion efficiency

The effect of the main parameters, i.e. reaction temperature and CO concentration, on carbon monoxide conversion efficiency is shown in Table 3. Based on the obtained results and as expected, there is a linear relationship between carbon monoxide conversion efficiency and reaction temperature, CO concentration, and type of reactor.

Figure 5a shows the carbon monoxide conversion efficiency by CuO/Zeolite 13X and Zeolite 13X nanocatalysts as a function of reaction temperature. The composition of the incoming feed stream contains 800 ppm of CO gas with a space velocity of 22641 h^{-1}. Based on the analysis of variance, reaction temperature (A) has a positive linear effect on carbon monoxide conversion efficiency. According to the results shown in Figure 5a, the CuO/Zeolite 13X nanocatalyst is inactive at temperatures below 100°C, and the carbon monoxide conversion efficiency is low. At a temperature of 100 °C, the conversion efficiency is equal to 6.77% (experiment number 3) and with increasing temperature, the efficiency of carbon monoxide conversion also increases so that it reaches 41.57% on average at a temperature of 300°C and 92.96% at a temperature of 500 °C (experiment number 20) found that the obtained results are consistent with similar studies [20, 32]. Of course, according to previous studies [39], by using copper oxide nanoparticles with a smaller diameter (up to 5 nm), it is possible to achieve a carbon monoxide conversion efficiency of 99.5% at a temperature of 250 °C, which indicates the effect of the catalyst preparation method and the size of the nanoparticles.

Figure 5b shows the effect of CO concentration of 1100-500 ppm on CEC during carbon monoxide oxidation by CuO/Zeolite13X and Zeolite13X nanocatalysts at 300°C and with a space velocity of 22641 h^{-1}. Based on the analysis of variance, CO concentration has a linear negative effect on carbon monoxide conversion efficiency. The experimental results show that when the concentration of CO is equal to 500 and 1100 ppm at a constant temperature of 400 °C, the conversion efficiency of carbon monoxide is equal to 82.60% (experiment number 12) and 78.89% (experiment number 11), respectively. Theoretically, the conversion efficiency decreases with the increase in pollutant concentration, which is consistent with the results of this study. Of course, using a pure oxygen cylinder can limit this effect and increase the catalyst's efficiency [40], which could not be used in this study due to existing limitations.

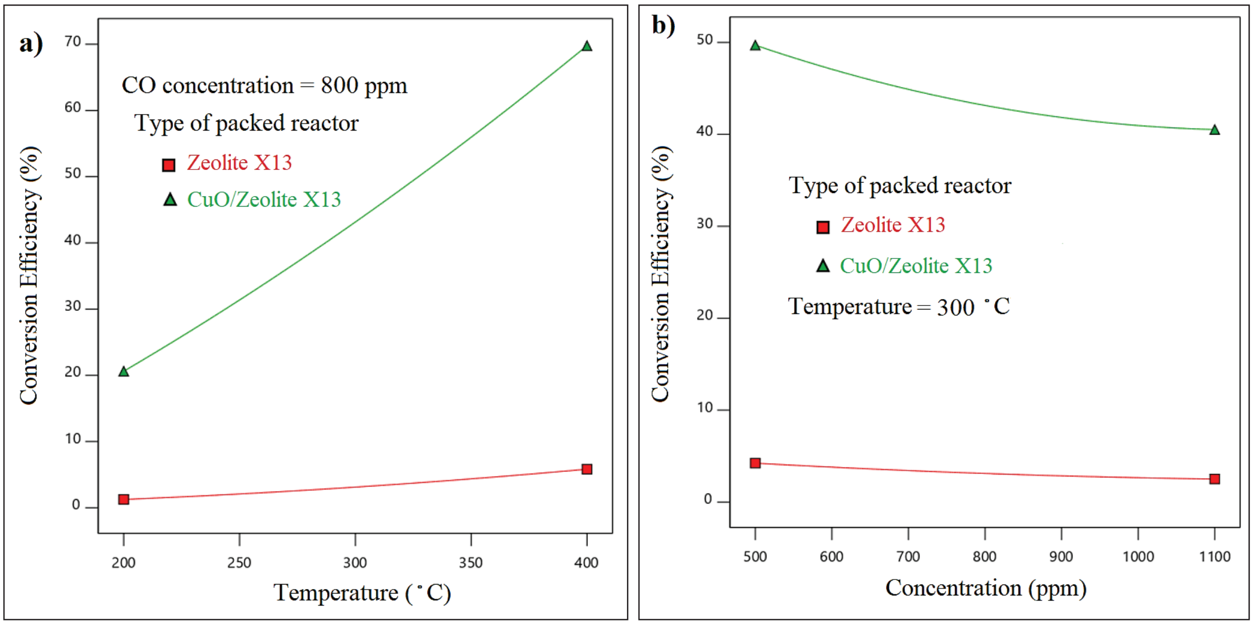

Fig. 5. The results of the effect of (a) reaction temperature and (b) carbon monoxide concentration on carbon monoxide conversion efficiency

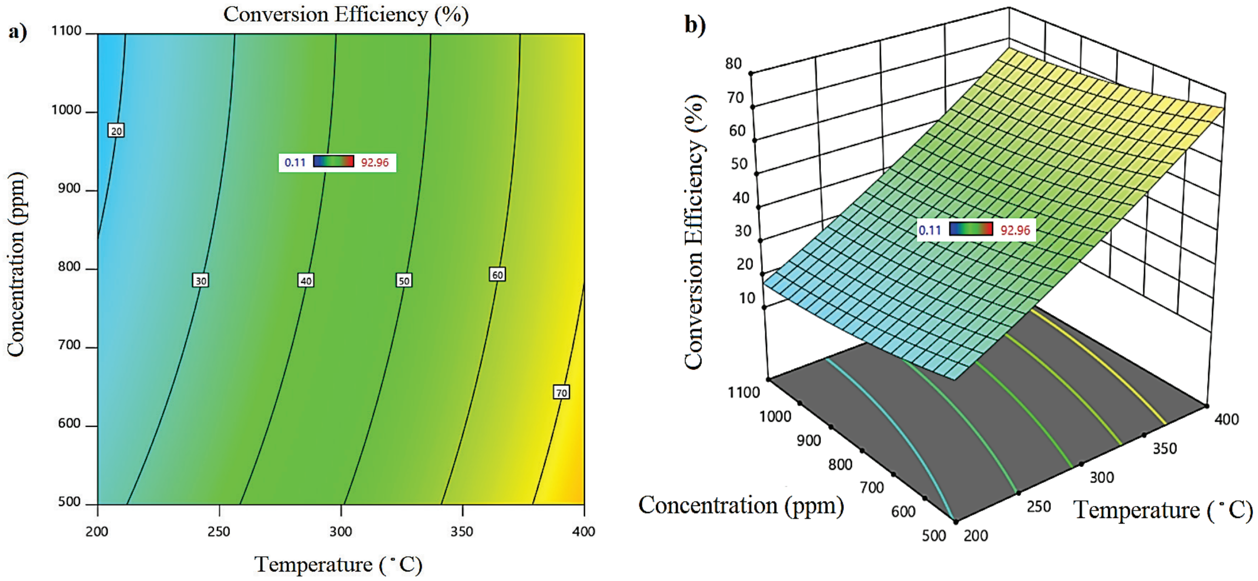

Fig. 6. a) surface view and b) three-dimensional view of the effect of main variables on carbon monoxide conversion efficiency by CuO/Zeolite 1 nanocatalyst

3.4. Three-dimensional (3D) response surfaces and contour plots

Figures 6a and 6b show three-dimensional (3D) response surfaces and contour plots indicating the main variables' effect (CO concentration and reaction temperature) on CEC by CuO/Zeolite 13X nanocatalyst. According to Figures 6a and 6b, there is a positive linear relationship between reaction temperature and CEC and a negative linear relationship between CO concentration and CEC, which means that the CEC increases with increasing temperature and decreasing CO concentration.

3.5. Determining the optimal conditions for carbon monoxide conversion efficiency and validation

In the carbon monoxide conversion process by the CuO/Zeolite 13X nanocatalyst, based on the optimization, the highest carbon monoxide conversion efficiency of 75.94% was obtained at a concentration of 500 ppm and a reaction temperature of 400 °C as optimal conditions. Further, to confirm the correctness and validity of the model obtained from the experimental results of carbon monoxide conversion efficiency by CuO/Zeolite 13X nanocatalyst, experiments were conducted under optimal conditions, and the results are reported in Table 4. As shown in Table 4, the result of the confirmation test lies between the lower and upper limits of the 95% confidence interval, and so on, the results of predictions by the model and experimental tests are in good agreement.

3.6. Characterization of CuO/Zeolite 13X catalysts

The results of the XRF test are shown in Table 5. According to the results obtained from the XRF test, Al_2O_3 and $SiO_{2,}$ with percentages of 23.397 and 45.108, are the main components of zeolite X13, which indicates the aluminosilicate structure of this material. The structure of this article confirms this. The results of the BET test are presented in Table 6.

Table 4. Optimized conditions with predicted and experimental values for the intended response

Response	Catalyst Type	Concentration (ppm)	Temperature (°C)	Predicted Response	Confirmation Experiment	C.I (95%)	
						Low	High
CEC	CuO/Zeolite13X	500	400	75.94	82.6	68.88	82.99

Based on the results, the specific surface area and total pore volume of Zeolite 13X equal 495.85 m^2 g^{-1} and 0.265368 cm^3 g^{-1}, respectively. According to the studies conducted on other types of zeolite, it was found that Zeolite 13X has a higher specific surface area compared to USY and ZSM-5 zeolite [42-44] because increasing the specific surface increases the active sites, and as a result, the reaction efficiency increases, Zeolite 13X can be a more suitable substrate for the catalyst compared to other zeolites. According to the BJH test shown in Figure 7, based on adsorption and desorption, N_2 isotherms zeolite 13X has a structure composed of mesoporous and microspores (Table 7). So 62.77% of the zeolite13X is microporous, and 37.23% is mesoporous.

The images obtained from the FE-SEM test are shown in Figure 8, and the size distribution of nanoparticles calculated using MIPCloud software is shown in Figure 9. The images presented in Figure 8 show the uniform distribution of copper oxide nanoparticles on the surface of zeolite X13. Figure 9 shows the size distribution of nanoparticles. The cumulative percentage of nanoparticle size is different; particles of 20-40 nm have the highest cumulative rate, and particles larger than 100 nm have a cumulative percentage of less than 25%. The results of the EDX test are shown in Figure 10, which shows the weight percentage of the copper element stabilized on the X13 zeolite bed. Based on the results, copper oxide nanoparticles with a weight percentage of 5.4% have been stabilized

Table 5. Elemental analysis test results(XRF) of zeolite X13

Components	Si/Al	Fe_2O_3	TiO_2	K_2O	SiO_2	Al_2O_3	MgO	Na_2O	LOI
Zeolite13X	1.928	1.027	0.017	0.504	45.108	23.397	1.92	11.336	15.95
Components	2.77	ND	ND	ND	49.28	30.17	ND	12.49	----

Table 6. Structural features of zeolite 13X (BET Equation) in CuO/Zeolite13X

Adsorption average pore diameter by BET A^0	The total pore volume of pores cm³ g^{-1}	BET Surface Area m²/g	BJH Adsorption average pore A^0
21.40	0.265368	495.8508	28.172

Table 7. Characterization of microporous and mesoporous pores in CuO/Zeolite13X

Microspore volume	Microspores surface area	Mesoporous volume	Mesoporous surface area	Microspores %	Mesoporous %
0.16657	453.847	0.0988	42.003	62.77	37.23

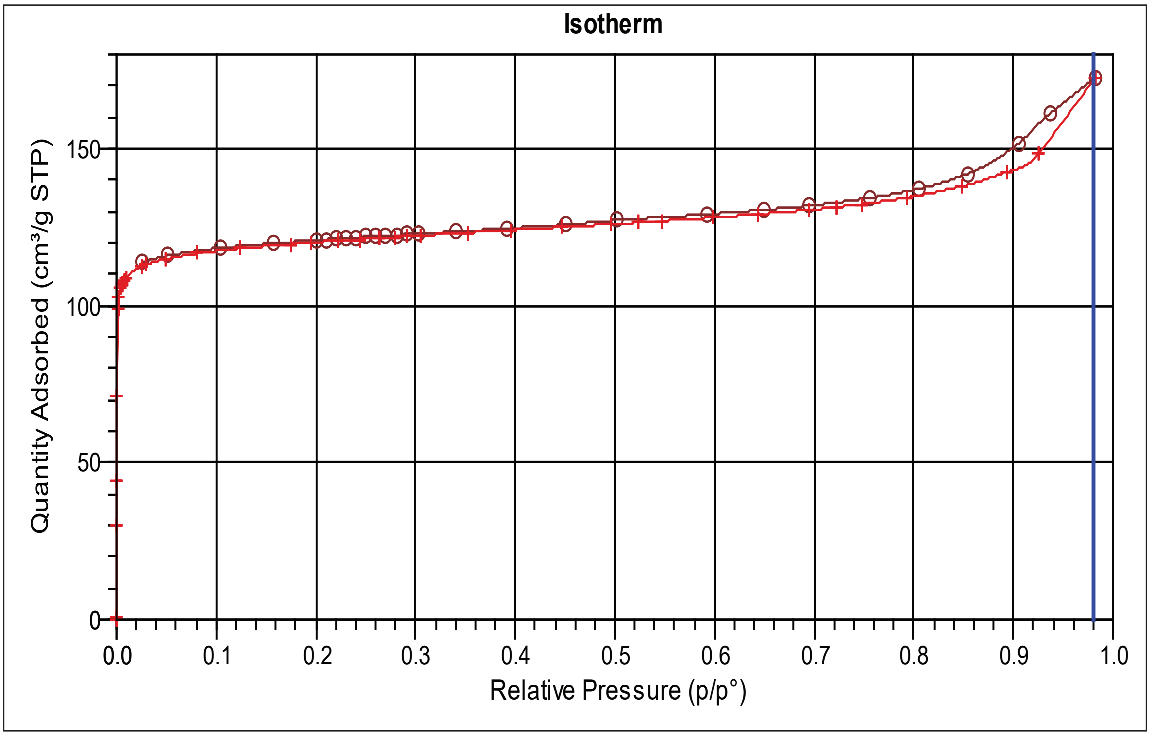

Fig. 7. Adsorption and desorption isotherms N2 for CuO/Zeolite 13X nanocatalyst

on the X13 zeolite substrate. Based on previous studies, the optimal efficiency of carbon monoxide conversion by copper nanocatalyst with a weight percentage of 4-5% stabilized on different substrates has been reported and based on these results [20, 32], increasing the loading of copper oxide nanoparticles on the substrate does not only lead to an increase in efficiency but also the accumulation of nanoparticles and collection of masses causes a decrease in catalytic activity. As a result of the EDX test obtained from Zeolite13X, silica and aluminum, which are the main components of zeolite, can be seen.

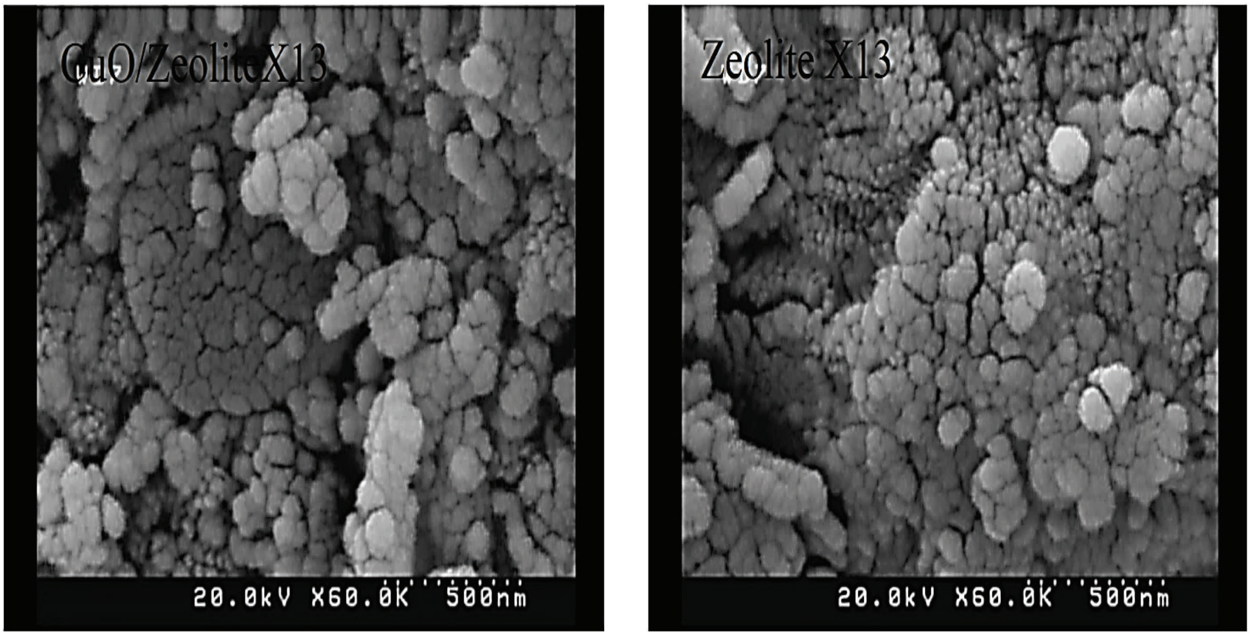

Fig. 8. Scanning electron microscope image of CuO/Zeolite 13X and zeolite 13

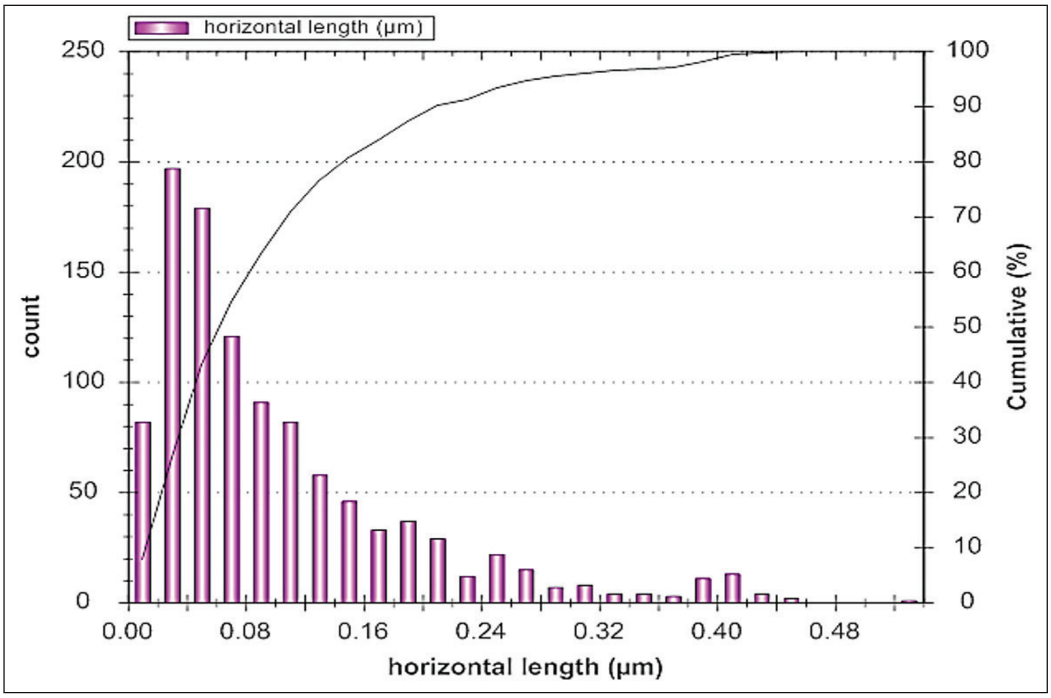

Fig. 9. Size distribution of copper oxide nanoparticles immobilized on zeolite13X

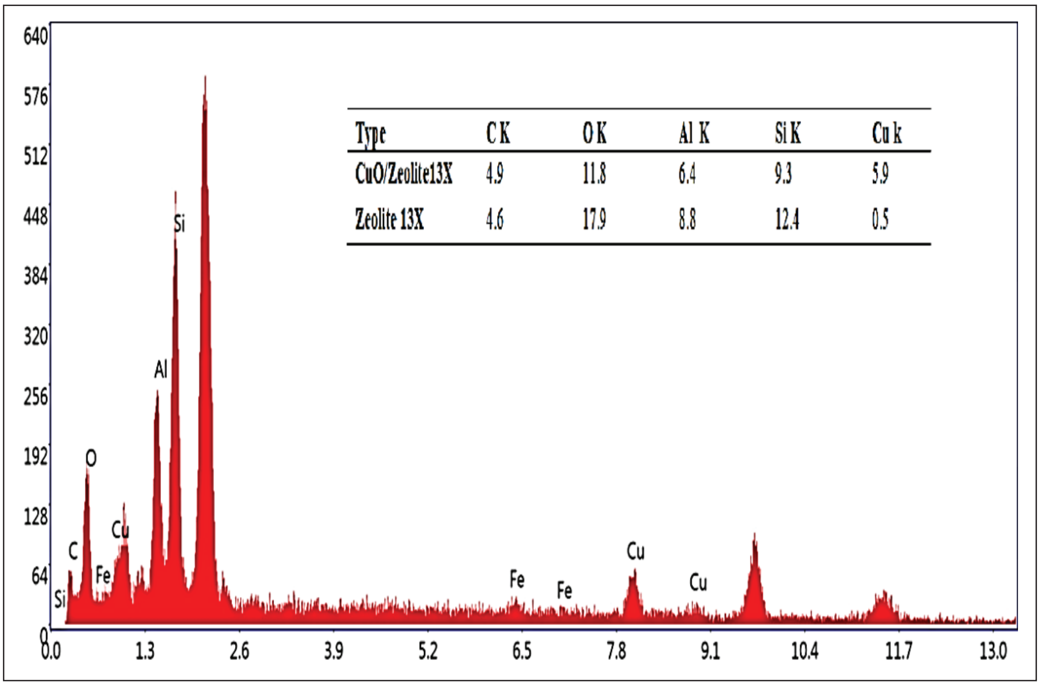

Type	C K	O K	Al K	Si K	Cu k
CuO/Zeolite13X	4.9	11.8	6.4	9.3	5.9
Zeolite 13X	4.6	17.9	8.8	12.4	0.5

Fig. 10. Energy-dispersive X-ray spectroscopy (EDX) test results

4. Conclusion

This study was conducted to determine the efficiency of carbon monoxide conversion by CuO/Zeolite 13X nanocatalyst. Based on the results, this nanocatalyst has acceptable efficiency and thermal stability in carbon monoxide oxidation. However, it is significant that compared to other natural and synthetic zeolites, zeolite 13X has a much higher surface area (according to the 495-bat test), which can provide many active sites for nanoparticles. However, based on the results obtained from the XRD images, it was found that the most significant number of particles stabilized on zeolite 13X having a diameter equal to 60-40 nm, which indicates the clumping of nanoparticles and the reduction of the contact surface of the carbon monoxide flow with the nanocatalyst. Based on previous studies, nanoparticles with smaller dimensions can be produced by changing the manufacturing method, increasing efficiency and decreasing reaction temperature.

5. Acknowledgement

Dr. Hasan Asilian Mahabadi was responsible for guiding and advising on the research. Miss Bahar Parsazadeh was accountable for doing experiments, analyzing and interpreting the data, and writing the manuscript. Dr. Niloofar Damyar was responsible for data analysis, interpretation of the data, and correction of the written manuscript.

6. References

[1] B.M. Kuehn, WHO: More than 7 million air pollution deaths each year, Jama, 311 (2014) 1486-1486. https://doi.org/10.1001/jama.2014.4031

[2] G.K. Gulati, L.K. Gulati, S. Kumar, Carbon monoxide sensing technologies, Materials Research Forum LLC publisher, 2021. https://www.mrforum.com/product/9781644901212/

[3] M. Comotti, W. C. Li, B. Spliethoff, F. Schüth, Support effect in high activity gold catalysts for CO oxidation, J. Am. Chem. Soc., 128 (2006) 917–924. https://doi.org/10.1021/ja0561441

[4] A. Joneydi Jaffari, M.J. Asari, M. Saremi, Determination of some air pollutants emited from hospital incinerators in Hamadan in 2002, J. Maz. Univ. Med. Sci., 15 (2005) 95-102. http://jmums.mazums.ac.ir/article-1-797-en.html

[5] G. Goudarzi, An assessment on dispersion of carbon monoxide from acement factory, J. Environ. Health Manage. Eng., 3 (2017) 163-168. http://eprints.kmu.ac.ir/id/eprint/26577

[6] F. Golbabaei, A. Vahid, A. Faghihi Zarandi, A novel nano-palladium embedded on the mesoporous silica nanoparticles for mercury vapor removal from air by the gas field separation consolidation process, Appl. Nanosci., 12 (2022) 1667-1682. https://doi.org/10.1007/s13204-022-02366-0

[7] S. Royer, D. Duprez, Catalytic oxidation of carbon monoxide over transition metal oxides, Chem. Cat. Chem., 3 (2011) 24-65. https://doi.org/10.1002/cctc.201000378

[8] R.M. Heck, R.J. Farrauto, S.T. Gulati, Catalytic air pollution control: commercial technology, 3r edition, John Wiley & Sons publisher, 544 pages, 2012. https://onlinelibrary.wiley.com/

[9] M.D. Mobarake, Thiol modified bimodal mesoporous silica nanoparticles for removal and determination toxic vanadium from air and human biological samples in petrochemical workers, NanoImpact, 23 (2021)100339. https://doi.org/10.1016/j.impact.2021.100339

[10] L. Theodore, Air pollution control equipment calculations, John Wiley & Sons, 2008. https://doi.org/10.1002/9780470255773

[11] M. Chen, Highly active surfaces for CO oxidation on Rh, Pd, and Pt, Surf. Sci., 601(2007) 5326-5331. https://doi.org/10.1016/j.susc.2007.08.019

[12] G. Ertl, Reactions at surfaces: From atoms to complexity (Nobel lecture), Angewandte Chem. Int. Edit., 47 (2008) 3524-3535. https://doi.org/10.1002/anie.200800480

[13] S. Dey, Cobalt doped CuMnOx catalysts for the preferential oxidation of carbon monoxide, Appl. Surf. Sci., 2441(2018) 303-316. https://doi.org/10.1016/j.apsusc.2018.02.048

[14] H. Yen, Tailored mesostructured copper/ceria catalysts with enhanced performance for preferential oxidation of CO at low temperature, Angewandte Chem., 124 (2012) 12198-12201. https://doi.org/10.1002/ange.201206505

[15] M. Krämer, Structural and catalytic aspects of sol–gel derived copper manganese oxides as low-temperature CO oxidation catalyst, Appl. Catal. A: General, 302 (2006) 257-263. https://doi.org/10.1016/j.apcata.2006.01.018

[16] M.G. Jeong, Room temperature CO oxidation catalyzed by NiO particles on mesoporous SiO2 prepared via atomic layer deposition: Influence of pre-annealing temperature on catalytic activity, J. Mol. Catal. A: Chem., 414 (2016) 87-93. https://doi.org/10.1016/j.molcata.2016.01.002

[17] J. Knudsen, Low-temperature CO oxidation on Ni (111) and on a Au/Ni (111) surface alloy, ACS Nano, 4 (2010) 4380-4387. https://doi.org/10.1021/nn101241c

[18] Q. Guo, Y. Liu, MnOx modified Co_3O_4-CeO_2 catalysts for the preferential oxidation of CO in H_2-rich gases, Appl. Catal. B: Environ., 82 (2008) 19-26. https://doi.org/10.1016/j.apcatb.2008.01.007

[19] D. Svintsitskiy, Low-temperature catalytic CO oxidation over mixed silver–copper oxide $Ag_2Cu_2O_3$, Appl. Catal. A: General, 510 (2016) 64-73. https://doi.org/10.1016/j.apcata.2015.11.011

[20] M. Kikugawa, K. Yamazaki, H. Shinjoh, Characterization and catalytic activity of CuO/TiO_2-ZrO_2 for low temperature CO oxidation, Appl. Catal. A: General, 547 (2017)199-204. https://doi.org/10.1016/j.apcata.2017.09.005

[21] J.A. Schwarz, C.I. Contescu, K. Putyera, Dekker encyclopedia of nanoscience and nanotechnology, CRC press, Vol 5, 4014 pages, 2004. https://www.routledge.com/go/crc-press

[22] A.F. Zarandi, P. Paydar, A novel method based on functionalized bimodal mesoporous silica nanoparticles for efficient removal of lead aerosols pollution from air by solid-liquid gas-phase extraction, J. Environ. Health Sci. Eng., 18 (2020) 177-188. https://doi.org/10.1007/s40201-020-00450-7

[23] B. Solsona, Total oxidation of VOCs on mesoporous iron oxide catalysts: Soft chemistry route versus hard template method, Chem. Eng. J., 290 (2016) 273-281. https://doi.org/10.1016/j.cej.2015.12.109

[24] J. Kašpar, P. Fornasiero, N. Hickey, Automotive catalytic converters: current status and some perspectives, Catal. Today, 77 (2003) 419-449. https://doi.org/10.1016/S0920-5861(02)00384-X

[25] M. Bandyopadhyay, Gold nano-particles stabilized in mesoporous MCM-48 as active CO-oxidation catalyst, Micropor. Mesopor. Mater., 89 (2006) 158-163. https://doi.org/10.1016/j.micromeso.2005.09.029

[26] C.W. Chiang, A. Wang, C.-Y. Mou, CO oxidation catalyzed by gold nanoparticles confined in mesoporous aluminosilicate Al-SBA-15: Pretreatment methods, Catal. Today, 117 (2006) 220-227. https://doi.org/10.1016/j.cattod.2006.05.026

[27] Y. Jing, Preparation, Characterization and catalytic oxidation property of CeO_2/Cu^{2+}-attapulgite (ATP) nanocomposites, J. Rare Earths, 28 (2010) 347-352. https://doi.org/10.1016/S1002-0721(10)60328-6

[28] M. Moshoeshoe, M. S. Nadiye-Tabbiruka, V. Obuseng, A review of the chemistry, structure, properties and applications of zeolites, Am. J. Mater. Sci., 7 (2017) 196-221. https://doi.org/10.5923/j.materials.20170705.12

[29] I. Petrov, T. Michalev, Synthesis of zeolite A: a review, Sci. Works Ruse Univ., 51(2012) 30-35. https://www.scribd.com/document/435962390/Synthesis-of-Zeolite-a-a-Review

[30] G. Busca, Heterogeneous catalytic materials, solid state chemistry, surface chemistry and catalytic behaviour, 1st Edition, Elsevier, 2014. https://shop.elsevier.com/books/heterogeneous-catalytic-materials/busca/978-0-444-59524-9

[31] M Arjomandi, A review of analytical methods, Anal. Methods in Environ. Chem. J., 2 (2019) 97-126. https://doi.org/10.24200/amecj.v2.i03.73

[32] S. D. Athar, H. Asilian, Catalytic Oxidation of Carbon Monoxide Using Copper-Zinc Mixed Oxide Nanoparticles Supported on Diatomite, J. Health Scope, 1 (2012) 52-56. https://doi.org/10.24200/amecj.v2.i03.7310.5812/jhs.4590

[33] F. Mansouri, Energy efficiency improvement in nitric oxide reduction by packed DBD plasma: optimization and modeling using response surface methodology (RSM), Environ. Sci. Pollut. Res., 27 (2020) 16100-16109. https://doi.org/10.1007/s11356-020-07870-w

[34] N. Hasyimah, M. Rashid, H. Norelyza, Optimization of a developed multi-cyclone using response surface methodology (RSM) to control fine particulate emission, Eng. Innov., 4 (2023) 21-29. https://doi.org/10.4028/p-7540tu

[35] A.N. Tamar, M. Karbasi, M. R. Khani, Response surface methodology (RSM) for optimizing ozone-assisted process parameters for formaldehyde removal, J. Environ. Health Sci. Eng., 21 (2023) 475-484. https://doi.org/10.1007/s40201-023-00873-y

[36] R.M. Gholami, S. Mousavi, and S. Borghei, Process optimization and modeling of heavy metals extraction from a molybdenum rich spent catalyst by Aspergillus niger using response surface methodology, J. Ind. Eng. Chem., 18 (2012) 218-224. https://doi.org/10.1016/j.jiec.2011.11.006

[37] M. Fayazi, Removal of Safranin dye from aqueous solution using magnetic mesoporous clay: optimization study, J. Mol. Liq., 212 (2015) 675-685. https://doi.org/10.1016/j.molliq.2015.09.045

[38] W. Djoudi, F. Aissani-Benissad, S. Bourouina-Bacha, Optimization of copper cementation process by iron using central composite design experiments, Chem. Eng. J., 133 (2007) 1-6. https://doi.org/10.1016/j.cej.2007.01.033

[39] B. White, Complete CO oxidation over Cu_2O nanoparticles supported on silica gel, Nano Lett., 6 (2006) 2095-2098. https://doi.org/10.1021/nl061457v

[40] C.Y. Lu, M. Y. Wey, The performance of CNT as catalyst support on CO oxidation at low temperature, Fuel, 86 (2007) 1153-1161. https://doi.org/10.1016/j.fuel.2006.09.022

Anal. Methods Environ. Chem. J. 6 (4) (2023) 52-64

Research Article, Issue 4
Analytical Methods in Environmental Chemistry Journal
Journal home page: www.amecj.com/ir

AMECJ

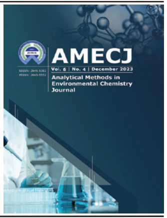

Design of sludge drying package pilot for removal of excess sludge in petrochemical industries: Heavy metals determination in sludge by polarography and atomic absorption spectrometry

Mostafa Hassani [a,b*] **and Bahareh Azemi Motlagh**[c]
[a] *Department of Applied Chemistry, Faculty of Science, Islamic Azad University, South Tehran Branch, Tehran, Iran*
[b] *Member of the Research Council of Sablan Petrochemical Industries Company, Assaluyeh. Iran*
[c] *Master of Environmental Management, Faculty of Natural Resource and Environment, Science and Research Branch, Islamic Azad University, Tehran, Iran*

ARTICLE INFO:
Received 16 Aug 2023
Revised form 20 Oct 2023
Accepted 24 Nov 2023
Available online 29 Dec 2023

Keywords:
Sludge,
Bed design,
Wastewater,
Heavy metals,
Atomic absorption spectrometry,
Polarography

ABSTRACT

In this research, according to the high amount of sludge in a petrochemical company, an iron package type of drying sludge bed was made/designed with carbon steel. Then, the drying sludge pond was filled with layers of sand with different mesh sizes. The excess sludge from the sedimentation pond was passed over this bed, and the amount of sludge removed by the bed was obtained at %96. The values of heavy metal and microbial forms were determined using the proposed method based on activated sludge after wastewater treatment. For the validation process, 10 mL of deionized water (DW) was mixed with 1.0 g of dried sludge with pure nitric acid (2% HNO_3), and then the solid phase was filtered with the Whatman filter (WF). The concentration of heavy metals (As, Cd, Cu, Pb, Hg, Mo, Ni, Co, Se, Zn) in the remaining solution of sludge (mg kg^{-1}) and wastewater (μg L^{-1}) was extracted/ separated based on sulfur-doped graphene oxide adsorbent (SDGO) by solid-phase microextraction procedure (SPME) before being determined by the flame and hydride generation atomic absorption spectrometry (F-AAS; HG-AAS) which had similar range to the polarography analysis. The limit of detection (LOD), linear range (LR) and preconcentration factor (PF) for (As, Hg) and (Cd, Cu, Pb, Mo, Ni, Co, Se, Zn) were obtained (0.016 μg L^{-1}; 3.3 μg L^{-1}), (0.05-10 μg L^{-1}; 10-1000 μg L^{-1}), and 10.0 by HG-AAS and F-AAS, respectively.

1. Introduction

Wastewater treatment is always associated with producing two parts: sewage and sludge. Effluent after secondary treatment is often of favourable quality for discharge into the environment, while sludge requires treatment and stabilization due to its high pollution load. Wastewater treatment concentrates the impurities and pollutants in them and separates them from the liquid phase. The detached part contains a high concentration of contaminants and undesirable substances that must be purified appropriately. This part is generally called sludge. In a wastewater treatment plant, sludge treatment and stabilization facilities are far more sensitive, specialized, and expensive than other units. So, sludge treatment

---

*Corresponding Author: Mostafa Hassani
Email: dr.hasani.2023@gmail.com
https://doi.org/10.24200/amecj.v6.i04.315

and disposal devices usually account for 40 to 60 percent of the construction cost and up to 50 percent of the operation cost of a treatment plant, creating a significant share of the operational problems related to this facility. Based on this, special attention should be paid to the technical and economic optimization of sludge purification and stabilization methods [1]. The main technology in wastewater treatment is removing organic matter by biological oxidation. The final products of this process are new cells (sludge), carbon dioxide, soluble microbial products, and water. The activated sludge process is widely used worldwide in municipal and industrial wastewater treatment. The daily production of excess sludge from the conventional activated sludge process is about 15 to 100 litres per kilogram of BOD_5 removed, which contains more than 95% water [2]. Since the sludge produced as a waste material must continuously be discharged into the environment economically, biomass production is of economic importance. Nowadays, the solutions to minimize excess sludge production in the activated sludge process are becoming very practical. Therefore, it seems necessary to review the methods used to reduce the sludge production from the activated sludge process on an industrial scale [3]. Until now, the main techniques are the aerobic process with anaerobic sedimentation [4], activated sludge process combined with ozonation [5], sludge retention time control and its biological decomposition [6], and high dissolved oxygen process [7] for the management of excess sludge produced in the activated sludge process has been reported. Since the disposal of excess sludge from purification systems in the environment is done either as compost (fertilizer) or as landfill, the presence of heavy metal pollution plays an important and influential role in its disposal because the entry of heavy metals into the soil and the structure of plants, it will eventually appear in the human body through diffusion in water and dust. Heavy metals such as arsenic (skin cancer) [8-9], cadmium (lung cancer) [10-11], copper (kidney and liver failure) [12], lead (destroying the nervous system) [13], mercury (congenital abnormalities) [14-15], molybdenum (hyperactivity and convulsion factor) [16], nickel (cardiovascular abnormalities) [17] and selenium (kidney and liver destruction) [18] which are considered a serious threat to human health. There are many methods for determining and extracting heavy metals from different matrixes. Recently, some adsorbents such as nano graphene oxide modified phenyl methanethiol nanomagnetic composite, Fe3O4-supported naphthalene-1-thiol-functionalized graphene oxide (SH-GO), CysSB/MetSB@MWCNTs, task-specific ionic liquid immobilized on multi-walled carbon nanotubes (TSIL-MWCNTs), functionalized multi-walled carbon nanotubes (F-MWCNTs), MWCNTs@DMP, nitrogen-doped porous graphene adsorbent (NDPG), immobilization of N-acetylcysteine on MWCNTs, thiol modified bimodal mesoporous silica (HS-UVM7), and palladium embedded on the mesoporous silica (Pd-MSN) were used for extraction and determination heavy metals in different matrixes[19-31].

Therefore, in this research, the design and construction of a pilot sludge drying reactor to dispose of the excess sludge of petrochemical industries (methanol) and measure the amount of fecal coliforms, and heavy metals such as cadmium, copper, lead, nickel, cobalt and zinc (Cd, Cu, Pb, Ni, Co, Zn were determined by polarography (VT). Also, after treatment in the resulting sludge, Hg, As, Se, Mo plus Cd, Cu, Pb, Ni, Co, and Zn were determined by F-AAS and HG-AAS.

2. Experimental

2.1. Instrumental

Polarography is an electrolysis technique in which micro-electrodes are performed at a solution's dropping mercury electrode (DME). The polarography device measured the heavy metals (Metrohm model VA Computrace 797, Swiss) by the anodic stripping voltammetry (ASV) mode. The results are achieved as a current–voltage curve (CVC). Polarography or voltammetry technique (VT) determines ion species based on loss or take electrons at the surface of a DME at an optimized potential. Electrode surfaces are used for inorganic and organic compounds. Polarography is used for heavy metal analysis (Cd, Cu, Pb, Ni, Co, Zn) in high sludge concentrations (mg kg^{-1}), but it cannot determine the low concentration of less than ppm. The Flame atomic absorption spectrometry had more sensitivities (DL<0.1 mmol L^{-1}) compared to polarography (DL>0.1 mmol L^{-1}). In analytical applications, the alternating current (AC) mode has more sensitivities than the direct current (DC) polarography, but it is better to use the FAAS for a low detection limit. In this work, we used polarography/ VT and F-AAS /HG-AAS for high and low values of heavy metals in sludge. The cold vapor-atomic absorption spectrometer (CV-AAS) was used for trace determination of mercury in the water samples (HG-3000, GBC, Aus). The $NaBH_4$ reagents and a reaction loop were used for mercury determination by CV-AAS. The linear ranges (LR) and the detection limit (LOD) of mercury were obtained between 1-60 μg L^{-1} and 0.25 μg L^{-1}, respectively, by open quartz cell of CV-AAS. The wavelength, the current lamp and the slit of mercury HCL were tuned at 253.7 nm, 3 mA and 0.5 nm, respectively, by AAS (peak area). The HG-AAS was also used for arsenic determination in water samples. Other heavy metals such as Cd, Cu, Pb, Mo, Ni, Se, Co and Zn were determined by flame atomic absorption spectrometer (F-AAS, GBC 932 plus, Autosampler, Air/Acetylene). The mean LOD and LR for Cd, Cu, Pb, Mo, Ni, Se, and Zn were obtained from 50-100 μg L^{-1} and 0.1-10 mg L^{-1}, respectively. A pH meter determined the sample pH (Metrohm AG 744, Switzerland).

2.2. Reagents and Materials

The different layers used in the designed bed consist of sand with different meshes, which are very economical. All reagents, such as nitric acid (Sigma, CAS No.: 7697-37-2, 65%) and sodium hydroxide, were purchased from Sigma and Merck (Germany). The standard solutions of arsenic, cadmium, copper, lead, mercury, molybdenum, nickel, selenium, and zinc (As, Cd, Cu, Pb, Hg, Mo, Ni, Co, Se, Zn) were purchased from Sigma, Germany. The different standard solutions of heavy metals were prepared by amounts of metal salt as 1000 mg L^{-1} solution by dissolving in HNO_3 (2%). The sample pH was adjusted using proper buffer reagents of sodium acetate (CAS No.: 6131-90-4, $CH_3COO\text{-}Na/CH_3COOH$) for pH 3 to 7.5. Pure GO (CAS No.: 1034343, CxHyOz) prepared from Sigma Aldrich, Germany. Sodium sulphite (CAS No.: 7757-83-7, Na_2S) was purchased from Merck, Germany.

2.3. Synthesis of sulfur-doped graphene oxide

The pure GO was prepared from Sigma, Germany. First, 5.0 mg of pure GO was dispersed in 10 mL of DW and was sonicated for 30 min as suspension material before adding 1.5 mL of Na_2S (2%). The mixture was shaken for 85 minutes at 95 °C, and S-doped reduced graphene oxide was produced (SDGO). Then, the SDGO adsorbent was cooled and separated (25°C) by centrifuging. The final product was washed with DW many times and separated by the Whatman filter. After drying for 2 hours in the oven (70°C), the adsorbent is used for further work (Fig.1).

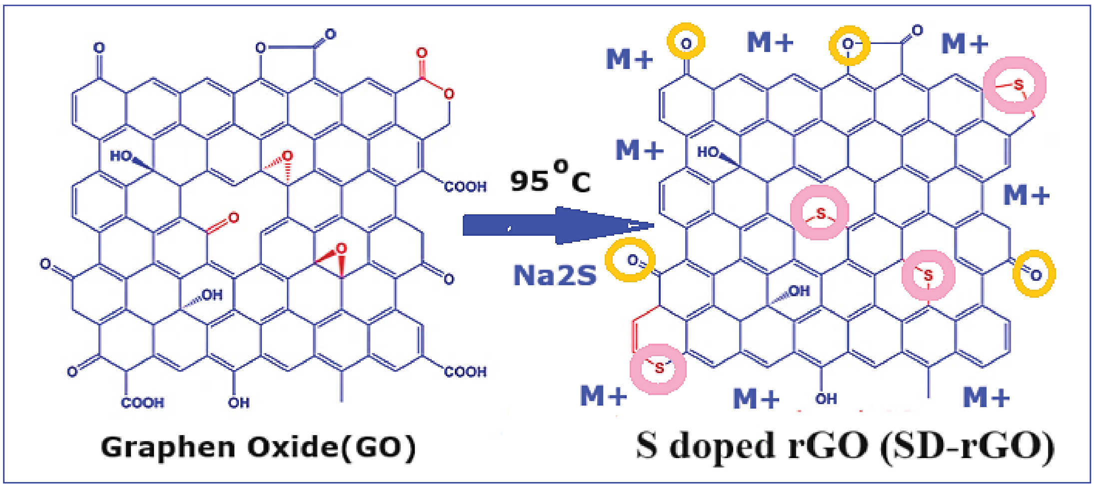

Fig. 1. Synthesis of sulfur-doped graphene oxide by Na_2S

2.4. Characterization

The field emission scanning electron microscopy (FE-SEM), XRD, and FTIR analysis characterized the S-doped graphene. FE-SEM images were obtained with a JEOL JSM-IT500 device. X-ray diffraction (XRD, Hitachi, Japan, EA8000A model, λ=1.5 Å) was used to analyze the crystalline nanostructures. Fourier Transform Infrared (FT-IR) spectra in the 400–4000 cm^{-1} range were achieved by the IR-Affinity-Shimadzu (Japan).

2.5. Description of the pilot

The designed drying sludge bed has an approximate volume of 0.6 cubic meters and sand layers with the size of sand from bottom to top (8 cm with 60 mm grain size, 6 cm with 18 to 25-grain size, 6 0 to 12 cm and 10 cm will be coarse grain sand). The material of the pilot body is stainless carbon with a thickness of 3 mm (Fig.2).

2.6. General procedure

To disinfect the sludge, it is enough to heat it twice at 60^{O}C [21]. F-AAS and HG-AAS validated the heavy metal analysis with a polarography device. First, 10 mL of DW was mixed with 1.0 g of dried sludge with pure nitric acid (2% HNO_3), and then the solid phase was filtered with the Whatman filter (WF). The heavy metals (M: As, Cd, Cu, Pb, Hg, Mo, Ni, Co, Se, Zn) in 20 mL of the remaining solution of sludge and wastewater (µg L^{-1}) were extracted based on 30 mg of SD-rGO as solid-phase microextraction procedure (SPME) at pH 6.5 and then heavy metals back-extracted from adsorbent with eluent (1.0 mL, HNO3, 0.5 M) before being determined by the flame and hydride generation atomic absorption spectrometry (F-AAS; HG-AAS) after dilution up to 2.0 mL with DW. The results showed heavy metal concentrations were like the VT analysis after sample treatment. For the VT, 10 g of each drying sludge or sludge sample was prepared with 60 mL of 3.0 M of HNO_3 for 2 hours of stirring. Finally, the samples were vacuum filtered (200 nm, Watman filter) and put into Cole-Parmer Essentials Plus Class A (100 mL, Canada), which was kept at 0^{o}C before determining heavy metals. An aliquot of 0.1 mL of each sample was diluted up to 200 mL with DW for the VT measurements. The dilution solution was put into the voltammetry cell before being degassed by Ar/N_2 for 25 minutes. Then, heavy metal ions (M: Cd, Cu, Pb, Ni, Co,

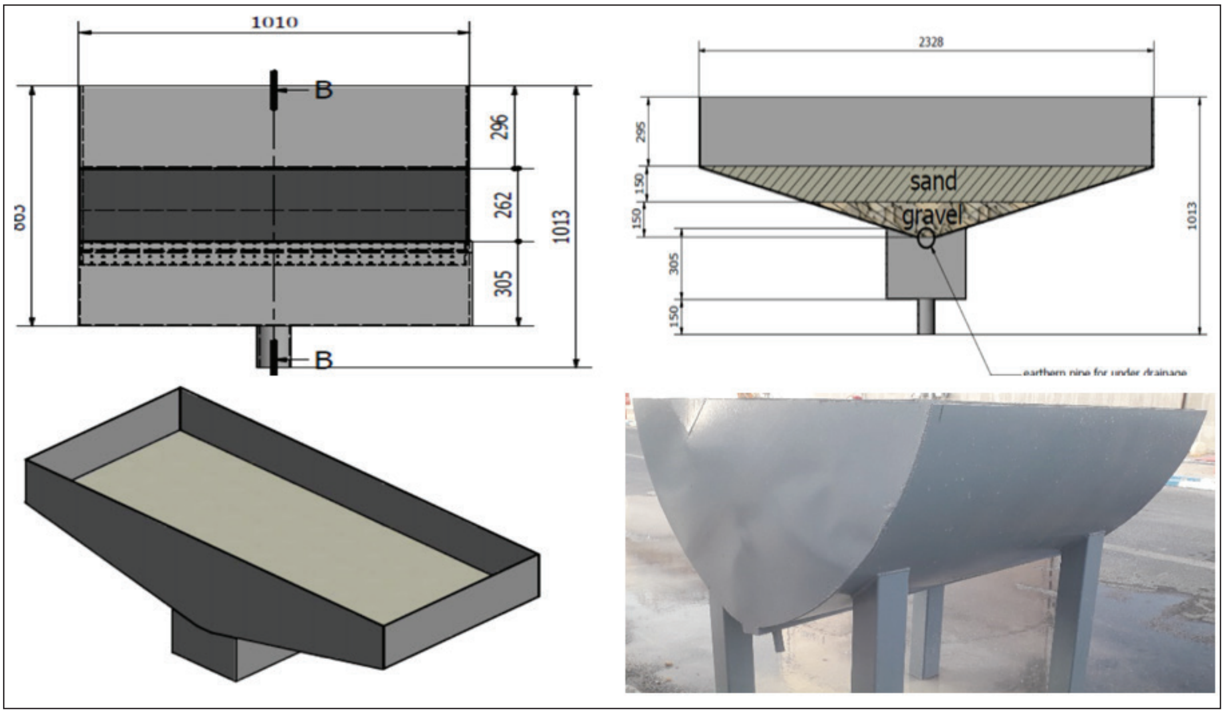

Fig.2. Image of the pilot design of the sludge dryer bed of the current project

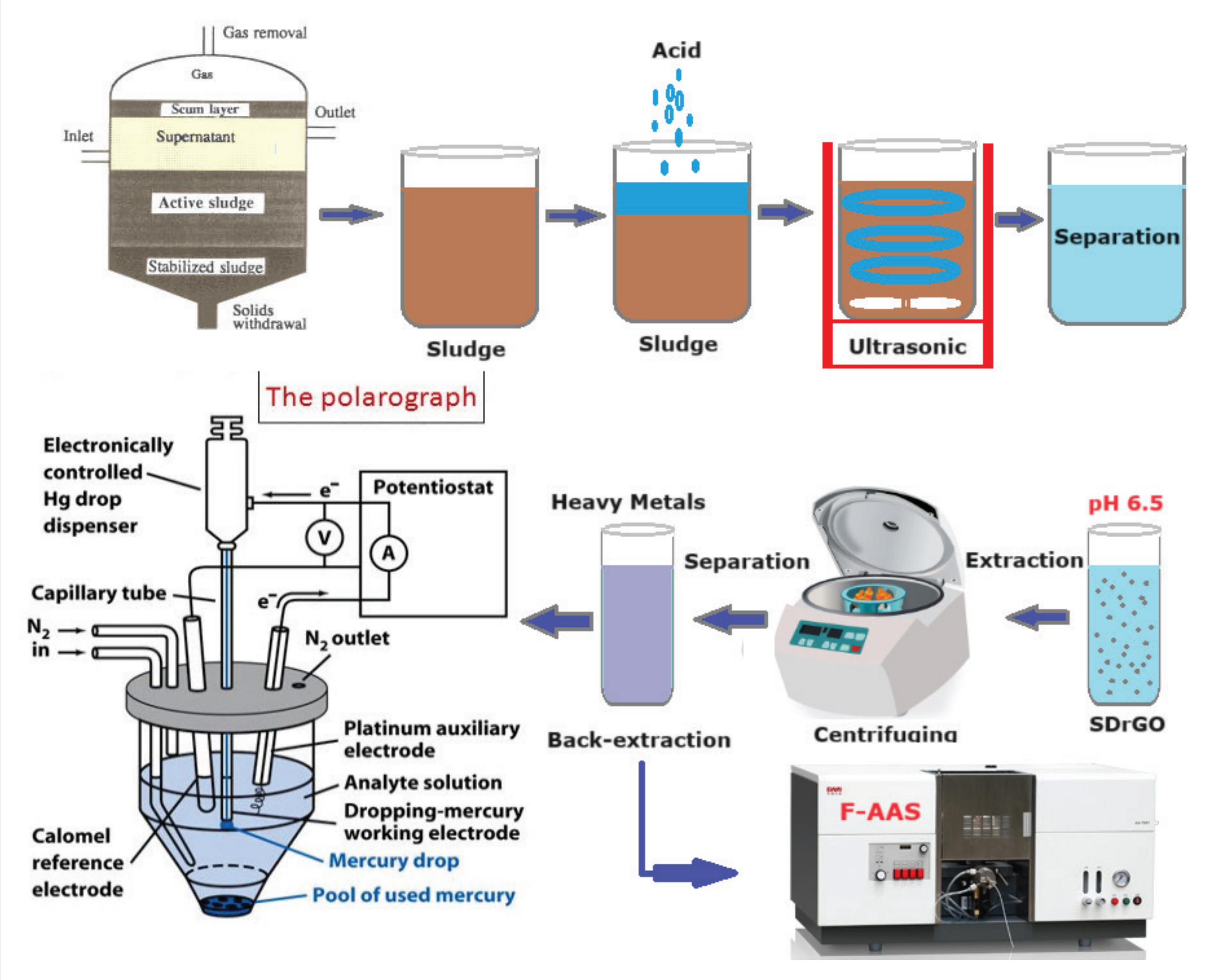

Fig.3. Procedure for extraction and determination of heavy metals by polarography and F-AAS

Zn) were deposited for 2.5 minutes at −1.2 V under stirring. (Fig.3) After 0.5 minutes, as equilibration time, the potential was scanned from −1.2 to 0.2 V by the anodic stripping voltammetry (ASV) mode (5 and 30 mV in square wave). Before peak integration, the VT software acquired baseline subtraction.

2.6.1.Measurement of sludge heavy metals with polarography

Voltammetry is an electrochemical method that, by measuring the amount of current in terms of potential changes in a three-electrode set, provides the possibility of qualitative and quantitative analysis of heavy metals in water and wastewater samples. This method is called polarography in special cases where the working electrode and a mercury drop electrode are used. This method allows qualitative and quantitative analysis of metals such as zinc, lead, tin, iron, nickel, cobalt, chromium, cadmium, etc. with high reproducibility. After equilibration time, the potential was scanned from −1.2 to 0.2 V by the anodic stripping voltammetry (ASV) mode.

2.6.2.Measurement of sludge heavy metals with AAS

All sample solutions were treated using SD-rGO adsorbent as an SPME procedure at pH 6.5. Then, after the back-extraction of heavy metals from SD-rGO adsorbent and dilution with DW, the concentrations of heavy metals were determined by F-AAS/HG-AAS.

3. Results and Discussion

3.1. FTIR spectra of SDGO

the FT-IR spectra of SD-rGO are shown in Figure 4. Based on the FT-IR spectrum, the peaks at 3458 cm^{-1} related to stretching vibrations of

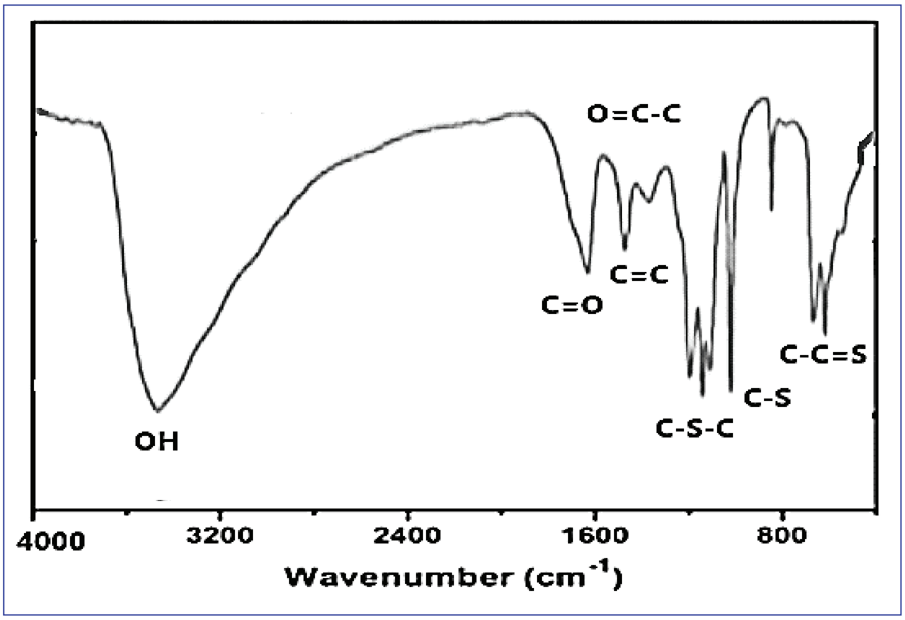

Fig. 4. FTIR spectra of SD-rGO adsorbent

-OH groups, 1628 cm^{-1} observed the carbonyl group(C=O), 1588 cm^{-1} peak showed carbon binding (C=C) and 1402 cm^{-1} are attributed to O=C–C bonding groups. Further, the peaks at 1201 cm^{-1}, 892 cm^{-1} and 575 cm^{-1} are related to the vibrations of C–S–C, C–S and C=S, respectively. The sulphur ions in Na_2S (negative charge) are absorbed with the carbonyl group (C=O) by the nucleophilic substitution mechanism.

3.2. XRS analysis

The XRD analysis of the pristine GO sheets and the SD-rGO sheets (2% sulphur doping) were obtained in Figure 5. Due to the XRD patterns, 30 mg of GO

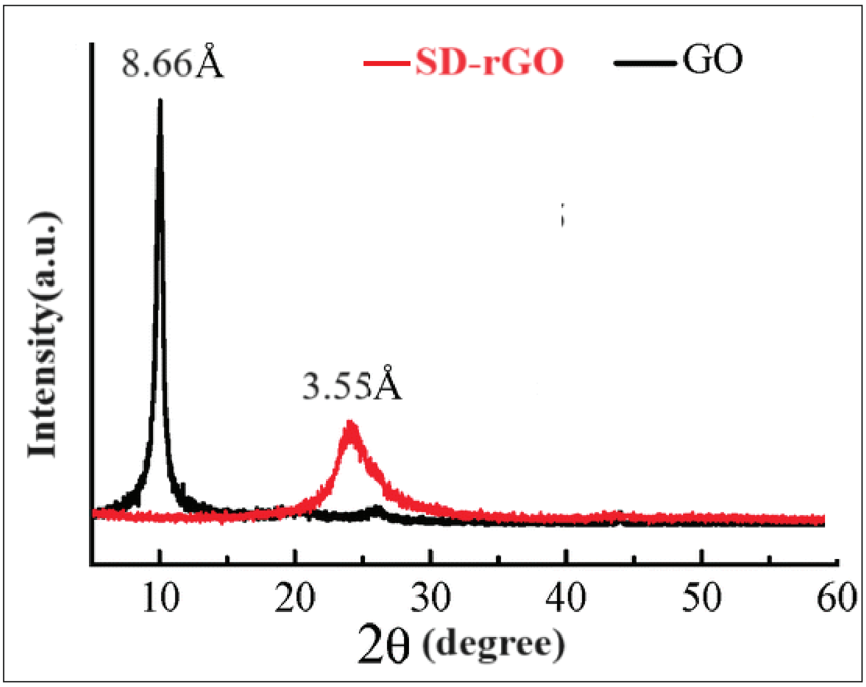

Fig.5. XRD Analysis of SD-rGO adsorbent

sheets have a sharp diffraction peak at $2\theta = 10.24°$ with an interlayer spacing of ~ 8.66 Å, related to the oxygen functional groups between graphene sheets. The SD-rGO adsorbent peaked at $2\theta = 24.21°$ associated with an interlayer spacing of ~ 3.55 Å. Thus, the XRD results showed the structural restoration of the graphitic during the hydrothermal reaction.

3.3. SEM of SD-rGO adsorbent

The SEM of GO and SD-rGO is shown in Figure 6. The size of GO and SD-rGO was between 35-100 nm. In images, the SD-rGO is in the nanometer range, and functionalization of S- did not result in aggregation of rGO. The images showed that the functionalization sulphur on rGO does not change the general structure and morphology of rGO.

3.4. Sludge volume measurement

To determine the amount of sludge volume, the SVI criterion with the name of the sludge volume index will be used. In this method, a 100 mL cylinder of the sample is poured, and after 30 minutes, its sedimentation rate is measured. It is filtered by filter paper and dried in an oven at a temperature of 105^{o}C, and the weight of the dry sludge is put into the following formula and calculated as the SVI [32]. (SVI: Sludge rate per 30-minute sedimentation rate)

3.5. Pilot control of sludge bed dryer

At this stage, first, the constructed sludge bed will be loaded with 200 litres of excess sludge from the sedimentation pond, whose volume index has already been measured, and the volume index of the output sludge will also be measured. Then, the pond is exposed to the ambient air for 120 hours to dry the sludge. The amount of heavy metals arsenic, cadmium, copper, lead, mercury, molybdenum, nickel, cobalt, and selenium is measured on it by a polarography and AAS device.

3.6. Optimization of pH, amount of adsorbent and sample volume for extraction in sludge

For efficient extraction of heavy metals, the amount of SD-rGO adsorbent between 5-50 mg has been examined in sludge samples by heavy metal concentration between 0.05-10 µg L^{-1} for Hg/As and 10-1000 µg L^{-1} for Cd/Cu/Pb/ Mo/ Ni/Se/Zn. The results showed that the maximum extraction of heavy metal ions in sludge samples

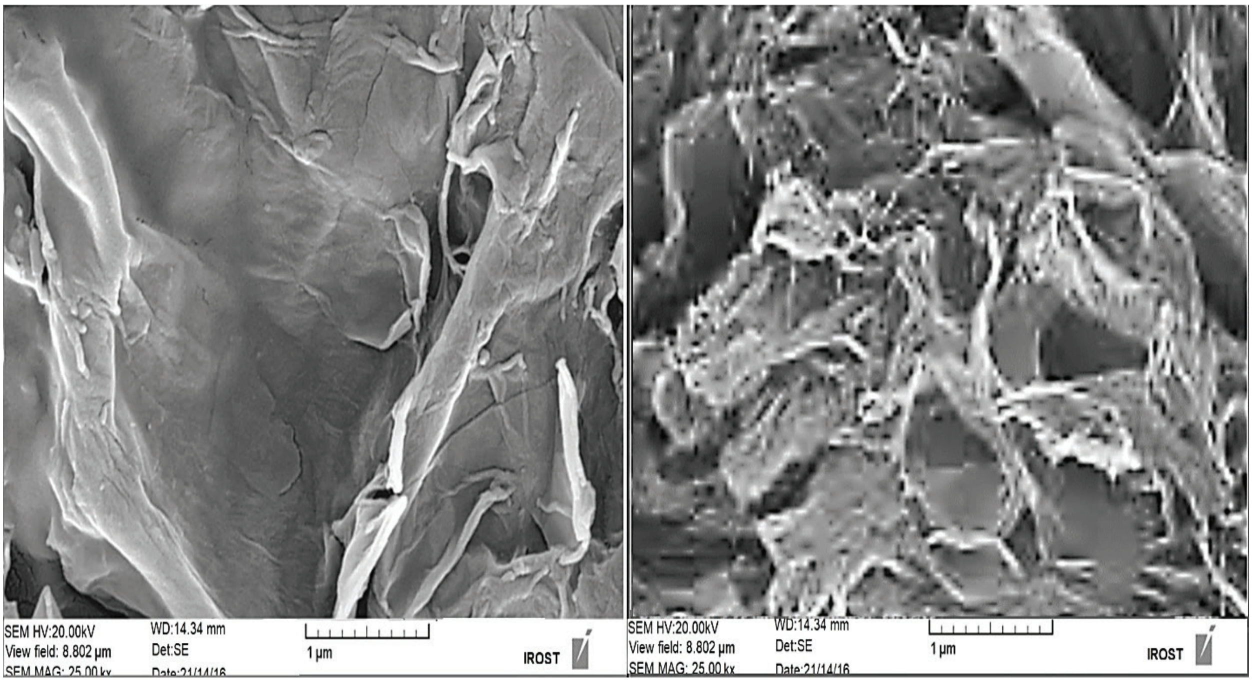

Fig.6. SEM of GO (Right) and SD-rGO (left)

was achieved at 30 mg of SD-rGO adsorbent at optimized conditions (Fig.7). The pH is the main factor for extracting heavy metals by SD-rGO adsorbent. Therefore, the various pH levels from 2 to 12 were studied in sludge samples through the buffer solutions. Due to the result, the best pH for Cd/Cu/Pb/Ni/Co/Zn concentration was obtained at 6.5 in sludge samples (Fig.8).

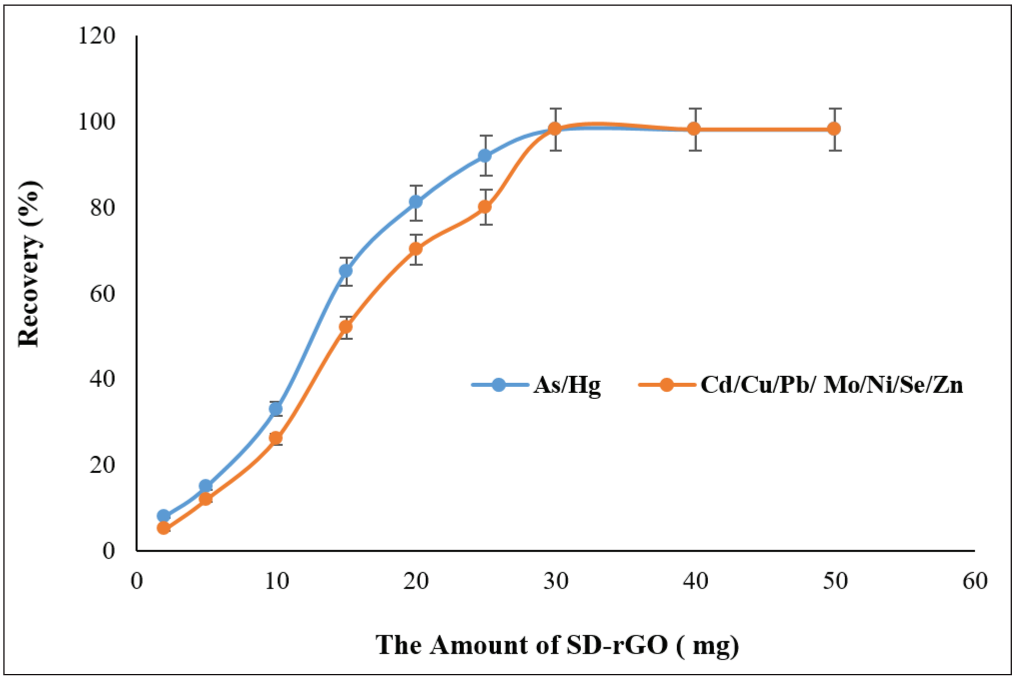

Fig.7. The effect of the amount of SD-rGO adsorbent on the extraction of heavy metals

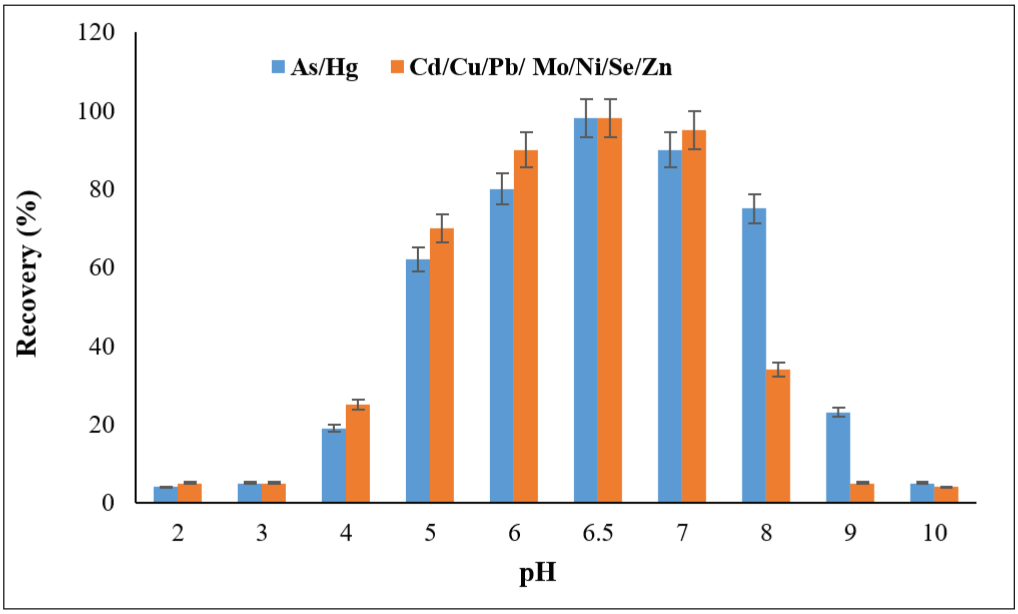

Fig. 8. The effect of pH on the extraction of heavy metals by the SD-rGO adsorbent

The extraction recoveries were decreased at less than a pH of 5 and more than 7. Also, the best volume for extraction was obtained at 20 mL. The various eluents such as HNO_3, HCl, and H_2SO_4 were used for back extraction of heavy metal ions from SD-rGO adsorbent. At low pH, the covalence bonding in S-Metal was broken, and metals were released in eluents. So, the procedure used the eluents (HNO3, HCl, and H2SO4) with different volumes and concentrations (0.2-0.8 mol L^{-1}, 0.2-2 mL). The results showed the HNO_3 (1 mL, 0.5 M) had maximum recovery.

3.7. Analysis in real samples

Table 1 shows the amount of SVI of the input and output of the sludge dryer. According to this table, the efficiency of removing SVI from the bed input has been 96% [33,34]. Table 2 and Figure 9 relate to the analysis of heavy metals in the output bed sludge by the polarography (Zn, Cd, Pb, Ni, Co,

Table 1. SVI of inlet and outlet wastewater sluge dryer

SVI	type
1900	sewage inlet bed
76	sewage outlet bed

Table .2 Concentration of heavy metals in dried sludge by polarography and F-AAS (mg kg^{-1})

Heavy Metals	Polarography	F-AAS	HG-AAS
As	-----	-----	0.048
Cd	0.041	0.039	-----
Cu	36.33	35.72	-----
Pb	0.096	0.101	-----
Hg	-----	-----	0.801
Mo	-----	-----	0.053
Ni	6.27	6.39	-----
Se	----	0.028	-----
Zn	8.69	8.92	-----
Co	5.23	5.18	-----

Table 3b. Standard concentration of pathogens in biological solids [35].

Concentration (MPN/100 mL)	Types of pathogens
191	Fecal coliforms
400	Total coliforms

MPN: Fecal coliform of organisms per 100 mL of sample water.
Maximum Acceptable Concentration for Drinking Water = no detected coliforms in 100 mL water.

Table 3a. The amount of digestive and fecal coliform in dried sludge

Concentration (MPN/100 mL)	Types of pathogens
191	Fecal coliforms
383	Total coliforms

MPN: Fecal coliform of organisms per 100 mL of sample water.
Maximum Acceptable Concentration for Drinking Water = no detected coliforms in 100 mL water.

Cu) and F-AAS. Also, the amount of digestive and fecal coliform in dried sludge and the standard concentration of pathogens in biological solids [35] are shown in Tables 3a and b. The standard concentration and loading rate of biological solids for use on land as sludge environmental standards are shown in Table 4 [35]. According to the results of Table 1, the dry sludge bed made in this research has a sludge removal efficiency of %96. The comparison of Tables 2 and 4 shows that the amount of heavy metals in the resulting sludge is by the environmental standards for use on the ground, and in this sense, there is no threat to the environment. On the other hand, comparing the results of microbiological analyses (Table 3a and 3b) with microbiological standards confirms the microbial standard of sludge. Therefore, the surplus sludge from this system can be used as compost in the green space with current conditions and disinfection at 60 degrees Celsius.

Table 4. Standard concentration and loading rate of biological solids for use on land [35].

Heavy metals	Max. Concentration (mg kg^{-1})	Concentration (mg kg^{-1})	Annual loading rate (mg kg^{-1})	Cumulative loading rate (mg kg^{-1})
As	75	41	2	41
Cd	85	39	1.9	39
Cu	4300	1500	75	1500
Pb	840	300	15	300
Hg	57	17	0.85	17
Mo	75	-	-	-
Ni/Co	420	420	21	420
Se	100	36	5	36
Zn	7500	2800	2	41

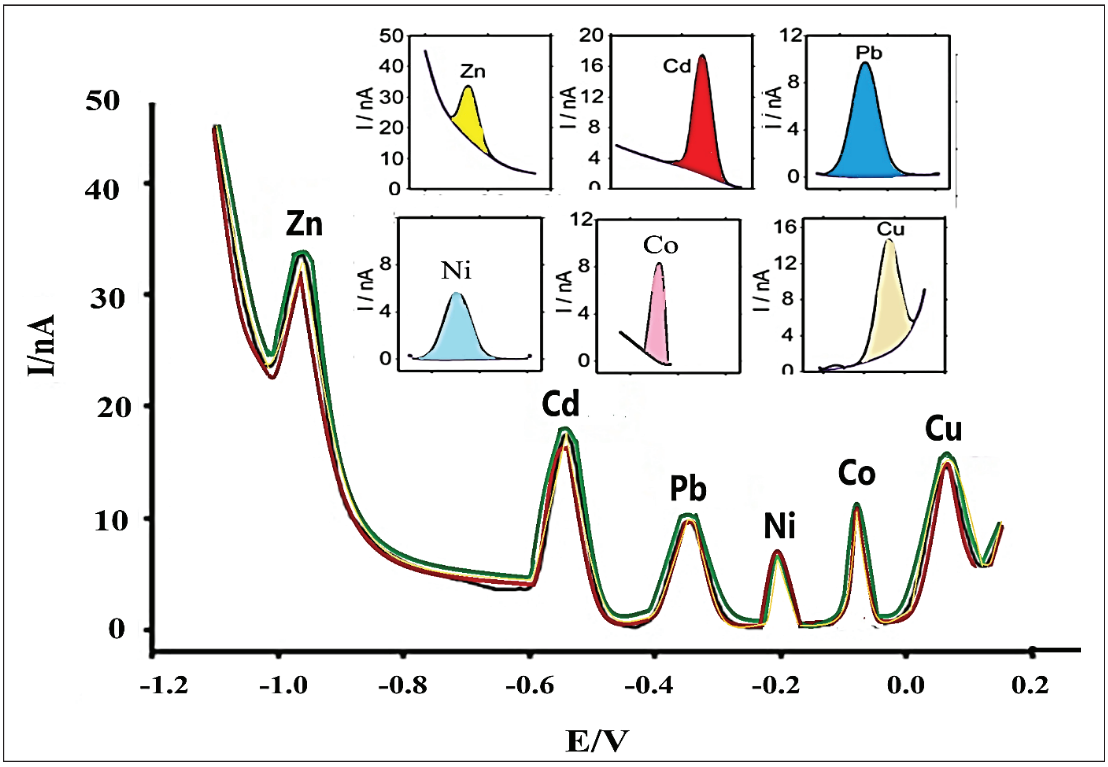

Fig. 9. Determination of heavy metals by the polarography (ASV mode)

4. Conclusion

Managing and controlling excess sewage sludge will be an important approach to preserving the environment and the health of living organisms in applications such as the cement industry and agriculture. Therefore, its purification is done by the methods of concentration, digestion, and dehydration, and its monitoring will prevent the entry of dangerous chemicals, such as heavy metals, into the environment. Therefore, in this research, a metal drying sludge package with an approximate capacity of 0.7 cubic meters with a bed of sand (8 cm with 60 mm grain size, 6 cm with 18 to 25-grain size, 6.0 to 12 cm and 10 cm will be coarse grain sand) was designed and built, which could reach 96% Physically remove excess sewage sludge. Considering the importance of the amount of heavy metals in the sludge, the concentration of these metals in the sludge obtained from the dryer sludge package was measured by polarography (ASV; ranges from 0.041 to 36.33 mg kg^{-1}) and atomic absorption methods (F-AAS, HG-AAS; ranges from 0.028 to 35.72 mg kg^{-1}). The results showed that the concentration of heavy metals in the resulting sludge is equal to standards and indicates the high-efficiency removal by packages (n=10, AAS: RSD<3% and CV: RSD<7%). Among the advantages of this package, we can mention the economical and changeable adsorbent bed so that in future research, we can use the method of sludge pretreatment with nanoabsorbents and change the bed of the dry sludge package to a large extent. So, the different amounts of heavy metals in the sludge are removed based on the changeable adsorbent bed. The package absorbed and removed the water coming out of the bed. As a result, this substrate can be widely used in the sewage industry due to its small volume and high sludge removal efficiency.

5. Acknowledgments

We are grateful for the unquestionable efforts of Mr. Farid Nikpour, Behnam Khodabakhshi, Ruhollah Asadi, Sajjad Kiyani, Yunes Koravand, and Habibullah Tahmasebi in designing and building the pilot package.

6. References

[1] M. Nasr, A.M. Negm, Cost-efficient Wastewater Treatment Technologies: Engineered Systems, Springer Nature, 385 pages, 2023. https://link.springer.com/book/10.1007/978-3-031-12902-5

[2] H. D. Stensel, R. Tsuchihashi, F.L. Burton, G. Tchobanoglous, Treatment and Resource Recovery, Fifth edition, McGraw-Hill, New York, NY, 2014. https://www.mheducation.com/

[3] Y. Liu, J.H. Tay, Strategy for minimization of excess sludge production from the activated sludge process, Biotechnol. Adv., 19 (2001) 97-107. https://doi.org/10.1016/S0734-9750(00)00066-5

[4] P. Chudoba, J. Chevalier, J. Chang, B. Capdeville, Effect of anaerobic stabilization of activated sludge on its production under batch conditions at various So/Xo ratios, Water Sci. Technol., 23 (1991) 917-926. https://iwaponline.com/wst/article-pdf/23/4-6/917/112799/917.pdf

[5] T. Kamiya, J. Hirotsuji, New combined system of biological process and intermittent ozonation for advanced wastewater treatment, Water Sci. Technol., 38 (1998) 145-153. https://doi.org/10.2166/wst.1998.0801

[6] M. Ghazizadeh, A. Abbasloo, F. Bivar, Speciation and removal of selenium (IV, VI) from water and wastewaters based on dried activated sludge before determination by flame atomic absorption spectrometry, Anal. Methods Environ. Chem. J., 4 (2021) 36-45. https://doi.org/10.24200/amecj.v4.i01.119

[7] L. A. Carrio, A.R. Lopez, P.J. Krasnoff, J.J. Donnellon, Sludge reduction by in-plant process modification, J. Water Pollut. Control Fed., 57 (1985)116-121. https://www.jstor.org/stable/25042541

[8] M. Berg, H.C. Tran, T.C. Nguyen, H.V. Pham, R. Schertenleib, W. Giger, Arsenic contamination of groundwater and drinking water in Vietnam: a human health threat, Environ. Sci. Technol. 35 (2001) 2621-2626. https://doi.org/10.1021/es010027y

[9] M.N. Hoang, P. Le Vo, T.V. Bui, P. Hung, Q.K. Ha, Health risk assessment of arsenic in drinking groundwater: A case study in a central high land area of Vietnam, IOP Conf. Ser.: Earth and Environ. Sci., IOP Publishing, 964 (2022) 012010. https://doi.org/10.1088/1755-1315/964/1/012010

[10] A. Ruczaj, M.M. Brzóska, Environmental exposure of the general population to cadmium as a risk factor of the damage to the nervous system: A critical review of current data, J. Appl. Toxicol., 43 (2023) 66-88. https://doi.org/10.1002/jat.4322.

[11] D. Hou, J. He, C. Lü, L. Ren, Q. Fan, J. Wang, Distribution characteristics and potential ecological risk assessment of heavy metals (Cu, Pb, Zn, Cd) in water and sediments from Lake Dalinouer, China, Ecotoxicol. Environ. Saf., 93 (2013)135-144. https://doi.org/10.1016/j.ecoenv.2013.03.012.

[12] B.R. Stern, M. Solioz, D. Krewski, P. Aggett, T.C. Aw, S. Baker, Copper and human health: biochemistry, genetics, and strategies for modeling dose-response relationships, J. Toxicol. Environ. Health B, 10 (2007) 157-222. https://doi.org/10.1080/10937400600755911

[13] K.F. Lee, E. Li, L.J. Huber, S.C. Landis, A.H. Sharpe, M.V. Chao, Targeted mutation of the gene encoding the low-affinity NGF receptor p75 leads to deficits in the peripheral sensory nervous system, Cell. 69 (1992) 737-749. https://doi.org/10.1016/0092-8674(92)90286-l.

[14] F. Zahir, S.J. Rizwi, S.K. Haq, R.H. Khan, Low-dose mercury toxicity and human health, Environ. Toxicol. Pharmacol., 20 (2005) 351-360. https://doi.org/10.1016/j.etap.2005.03.007

[15] M. Esteban-López, J.P. Arrebola, M. Juliá, P. Pärt, E. Soto, A. Cañas, Selecting the best non-invasive matrix to measure mercury exposure in human biomonitoring surveys, Environ. Res., 204 (2022)112394. https://doi.org/10.1016/j.envres.2021.112394

[16] V.S. Tambat, Y.S. Tseng, P. Kumar, C.W. Chen, R.R. Singhania, J.S. Chang, Effective and sustainable bioremediation of molybdenum pollutants from wastewaters by potential microalgae, Environ. Technol. Innov., 30 (2023)103091. https://doi.org/10.1016/j.eti.2023.103091

[17] K.K. Das, R.C. Reddy, I.B. Bagoji, S. Das, S. Bagali, L. Mullur, The primary concept of nickel toxicity–an overview, J. Basic Clin. Physiol. Pharmacol., 30 (2018) 141-152. https://doi.org/10.1515/jbcpp-2017-0171

[18] S.N. Luoma, T.S. Presser, Emerging opportunities in the management of selenium contamination, Environ. Sci. Technol. 43 (2009) 8483–8487. https://doi.org/10.1021/es900828h

[19] M. Arjomandi, A review: analytical methods for heavy metals determination in environment and human samples, Anal. Methods Environ. Chem. J., 2 (2019) 97-126. https://doi.org/10.24200/amecj.v2.i03.73

[20] B. Paknejad, M. Aliomrani, Is there any relevance between serum heavy metal concentration and BBB leakage in multiple sclerosis patients, Biol. Trace Elem. Res., 190 (2019) 289-294. https://doi.org/10.1007/s12011-018-1553-1

[21] M.K. Abbasabadi, Nanographene oxide modified phenyl methanethiol nanomagnetic composite for rapid separation of aluminum in wastewaters, foods, and vegetable samples by microwave dispersive magnetic micro solid-phase extraction, Food Chem., 347 (2021) 129042. https://doi.org/10.1016/j.foodchem.2021.129042.

[22] M.K. Abbasabadi, Speciation of cadmium in human blood samples based on Fe3O4-supported naphthalene-1-thiol-functionalized graphene oxide nanocomposite by ultrasound-assisted dispersive magnetic micro solid-phase extraction, J. Pharm. Biomed. Anal., 189 (2020) 113455. https://doi.org/10.1016/j.jpba.2020.113455

[23] Z. Karamzadeh, J. Rakhtshah, N.M. Kazemi, A novel biostructure sorbent based on CysSB/MetSB@ MWCNTs for separation of nickel and cobalt in biological samples by

ultrasound assisted-dispersive ionic liquid-suspension solid phase micro extraction, J. Pharm. Biomed. Anal., 172 (2019) 285-294. https://doi.org/10.1016/j.jpba.2019.05.003

[24] N. Esmaeili, J. Rakhtshah, E. Kolvari, Ultrasound assisted-dispersive-modification solid-phase extraction using task-specific ionic liquid immobilized on multiwall carbon nanotubes for speciation and determination mercury in water samples, Microchem. J., 154 (2020) 104632. https://doi.org/10.1016/j.microc.2020.104632

[25] M. D. Mobarake, Ultrasound-assisted solid-liquid trap phase extraction based on functionalized multi-wall carbon nanotubes for preconcentration and separation of nickel in petrochemical wastewater, J. Anal. Chem., 74 (2019) 865-876. https://doi.org/10.1134/s1061934819090090

[26] N. Esmaeili, J. Rakhtshah, E. Kolvari, A. Rashidi, Rapid speciation of lead in human blood and urine samples based on mwcnts@ dmp by dispersive ionic liquid-suspension-micro-solid phase extraction, Biol. Trace Elem. Res., 199 (2021) 2496-2507. https://doi.org/10.1007/s12011-020-02382-7.

[27] M. Bagheri Hosseinabadi, N. Khanjani, M.D. Mobarake, Neuropsychological effects of long-term occupational exposure to mercury among chloralkali workers, Work, 66 (2020), 491-498. https://doi.org/10.3233/WOR-203194

[28] M. Habibnia, A. Rashidi, A.F. Zarandi, Simultaneously speciation of mercury in water, human blood and food samples based on pyrrolic and pyridinic nitrogen doped porous graphene nanostructure, Food Chem., 403 (2023) 134394. https://doi.org/10.1016/j.foodchem.2022.134394

[29] J. Rakhtshah, Simultaneously speciation and determination of manganese (II) and (VII) ions in water, food, and vegetable samples based on immobilization of N-acetylcysteine on multi-walled carbon nanotubes, Food Chem., 389 (2022) 133124. https://doi.org/10.1016/j.foodchem.2022.133124.

[30] A. Faghihi-Zarandi, Thiol modified bimodal mesoporous silica nanoparticles for removal and determination toxic vanadium from air and human biological samples in petrochemical workers, NanoImpact, 23 (2021) 100339. https://doi.org/10.1016/j.impact.2021.100339.

[31] F. Golbabaei, A. Vahid, A. Faghihi Zarandi, A novel nano-palladium embedded on the mesoporous silica nanoparticles for mercury vapor removal from air by the gas field separation consolidation process, Appl. Nanosci. 12 (2022) 1667-1682. https://doi.org/10.1007/s13204-022-02366-0

[32] R.I. Dick, P.A.Vesilind, The sludge volume index: what is it, J. Water Pollut. Cont. Federation, 41 (1969)1285-1291. https://www.jstor.org/stable/25036678

[33] B. Nazemisalman, N. Bayat, S. Darvish, S. Nahavandi, M. Mohseni, I. Luchian, Polarography can successfully quantify heavy metals in dentistry, Medicina, 58 (2022) 448. https://doi.org/10.3390/medicina58030448

[34] Jr. J. Smith, K. Young, R. Dean, Biological oxidation and disinfection of sludge, Water Res., 9 (1975) 17-24. https://doi.org/10.1016/0043-1354(75)90147-5

[35] N. Miguel, J. Sarasa, Study of evolution of microbiological Properties in sewage sludge-amended soils: A pilot experience, Int. J. Environ. Res. Public Health, 17 (2020) 6696. https://doi.org/10.3390/ijerph17186696

Research Article, Issue 4
Analytical Methods in Environmental Chemistry Journal
Journal home page: www.amecj.com/ir

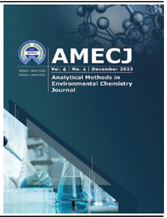

Removal of polypropylene nanoplastics from aqueous solution by biochar derived from Date palm fibers: Kinetics and isotherms studies

Mohammad Reza Rezaei Kahkha[a,*], Mahdi Rezaei Kahkha Zhaleh[b], Batool Rezaei Kahkha[a]

Maryam Khodadadi [c], and Mohsen Faghihi-Zarandi[d]

[a] Faculty of Health, Zabol University of Medical Sciences, Zabol, Iran
[b] Student Research Committee, Isfahan University of Medical Sciences, Isfahan, Iran
[c] Departement of Environmental Health Engineering, School of Health, Medical Toxicology and Drug Abuse Research Center, Birjand University of Medical Sciences, Birjand, Iran
[d] Foreign Languages Department, Shahid Bahonar University of Kerman, Kerman, Iran

ARTICLE INFO:
Received 25 Jul 2023
Revised form 11 Oct 2023
Accepted 7 Nov 2023
Available online 30 Dec 2023

Keywords:
Adsorption,
Activated carbon,
Polypropylene nanoplastics,
Date,
Kinetics,
Isotherm

ABSTRACT

In this work, activated carbon (AC) derived from powder of date palm fibers (DPF) was examined as an adsorbent for removing polypropylene nanoplastics (PPNPs) from aqueous solutions. The adsorbent was characterized using XRD, FT-IR, and SEM analyses. Affecting parameters on removal efficiency in a batch reactor, such as contact time, concentration of PPNPs and amount of adsorbent, were evaluated and optimized. Equilibrium and kinetic studies are performed to understand adsorption mechanisms. In the batch system, 30 mL of polypropylene suspension (5-40 mgL^{-1}) was added to Erlenmeyer flask. First, different amounts of AC adsorbent were added to the container, then microplastic was added to the reactor. The mixture was shaken on a shaker for four hours at 25°C. The flask was removed from the shaker, the concentration of PPNPs in the supernatant was measured, and a settling time of 30 min was obtained. A control suspension system without PPNPs nanoplastics (with biochar and without PPNPs) was also performed to evaluate carbon particle interference by turbidity measurements. Our results showed that kinetic data were consistent with the pseudo-second-order kinetic model. Equilibrium data for the adsorption of PPNPs on biochar represented by the Langmuir isotherm model is better than the Freundlich isotherm model.

1. Introduction

Microplastics are synthetic solid particles or polymer matrices with regular or irregular shapes, in sizes between 1 micrometre and 2 mm, with primary or secondary production origin and insoluble in water. Today, plastics are almost essential materials for human life. [1]The advantages of plastics, including long life, flexibility, resistance to light, excellent mechanical properties, resistance to atmospheric factors and long life, and low price, have led to their use in many cases to improve human life[1, 2]. Today, the global production of plastics is more than 361 million tons[3]. Microplastics can be classified based on their source. Primary microplastics are produced directly by humans, such as personal care products and cosmetic products[4]. Primary microplastics are

---

*Corresponding Author: Mohammad Reza Rezaei Kahkha
Email: m.r.rezaei.k@gmail.com
https://doi.org/10.24200/amecj.v6.i04.314

inevitably subjected to further degradation, which can change their size, morphology, color, density and surface functional groups. Secondary microplastics are obtained from the decomposition of larger pieces of plastic under chemical, physical and biological degradation in situ[5, 6]. Due to their widespread use, microplastics have spread everywhere and have been detected in freshwater, ocean, soil air, and polar regions [7]. The distribution of microplastics in aquatic environments is influenced by various factors such as size, shape, and type and the density of microplastics, as well as living organisms and chemicals in the water environment[8]. There are different ways for microplastics to enter environmental waters [9]. Studies have shown that the highest concentration of microplastics in fresh water is in glaciers and urban areas, followed by fresh water from rainwater and wetlands[10]. The concentration of microplastics has been reported from 900 to 2800 (ng m^{-3}) and from 1250 to 4650 nano gram per cubic meter, respectively, in Dongting Lake and Heng Lake[11, 12]. Minting and colleagues have reported the concentration of microplastics was 0 to 7 items per cubic meter in urban drinking water[13]. Another study showed that from 159 examined tap water samples from global sources, 81% were polluted with microplastics, with concentrations ranging from 0 to 61 pieces per litre, with an average of 5.45 pieces per litre [14]. Due to the importance of removing MPs from aquatic environments, many physical, chemical and biological methods have been proposed. Filtration, weight separation, electrified nanofiber membranes, coagulation and flocculation and sedimentation, advanced oxidation, membrane bioreactor, photocatalytic degradation and absorption are among the methods applied to remove MPs from water[15]. Among the mentioned methods, absorption is the most common, cheapest, fastest and oldest method used in water purification. The absorption method is environmentally friendly. Also, the process of doing it is easy, in addition, the absorbent can be used several times So far, adsorbents such as carbon nanotubes, graphene oxide, metal nanooxides, magnetic materials, coal, sand, activated carbon, aluminum chloride, silica gel, and other compounds such as clay, hydrogel, and sol gel have been used to remove microplastics from water. [16-18]. Also, polypropylene nanoplastics may be exist with other pollutants (VOCs and heavy metals) which must be analyzed based on nanotechnology before determination by GC or AAS methods. Recently, different carbon structures such as CNTs, active carbon, functionalized multi-walled carbon nanotubes, aminopropyl trimethoxysilane-phenanthrene carbaldehyde immobilized on graphene oxide, bimodal mesoporous silica nanoparticles, hydroxyethyl methylimidazolium tetrafluoroborate immobilized on MWCNTs, task-specific ionic liquids, Nanographene oxide modified phenyl methanethiol nanomagnetic composite, pyrrolic and pyridinic nitrogen doped porous, graphene nanostructure, and nano-palladium embedded on the mesoporous silica nanoparticles were used for removal VOCs and heavy metalsfrom water and air samples[19-28].

This research investigated the activated carbon obtained from date palm fibers for removing polypropylene pollutants from the water environment. The influencing variables on PPNPs absorption, including contact time, PPNPs initial concentration, and amount of adsorbent, were investigated and optimized.

2. Material and Methods

2.1. Reagents and Instruments

Polypropylene solution was obtained from Thermo Fisher Scientific-1862725 (Rheinach, Switzerland). Stock suspensions of 1.0 g L^{-1} were prepared from the original solution, which contained 10 g L^{-1} of PPNPs microplastic particles and diluted with ultrapure water (Milli Q water, Millipore, Switzerland). Before use, PPNPs stock suspension was sonicated for 15 min with a sonication bath (Bransonic ultra cleaner, Branson 5510 model, Switzerland). The stock solution was stored in a dark place at a constant temperature of 4 °C and used for further experiments.

2.2. Preparation of adsorbent

Activated carbon was prepared from the remaining dates collected from Zabol villages in eastern Iran. For the preparation of biochar, The date palm fibers biomass are placed in a ceramic tube in a horizontal furnace for 3 hours at a temperature of 400 degrees Celsius under a nitrogen flow at a speed of 5 cm^3 per second. Before activation, the particles are crushed and sieved. 10 g of charcoal were mixed with 10 g of KOH and stirred for four hours. Then, the obtained charcoal was placed in the oven for 48 hours at 150 °C . After drying, biochar was transferred to the furnace under nitrogen flow at 700 °C for 4 hours. Then, the activated charcoal was washed with HCl and distilled water, respectively, until it reached neutral pH, and then the absorbent was dried in an oven at 80 °C for 24 hours[29].

2.3. Characterization of adsorbents

An X-ray diffractometer (XRD, ALMELO, Netherlands) was utilized to get the XRD patterns of the date fibers structure. The SEM instrument (SEM, QUANTA 400F) depicted the surface morphology images. SEM images assisted in revealing the changes in the surface morphology that occurred due to adsorbent synthesizing or due to the adsorption process. FT-IR, Perkin Elmer Mattson 1000 (USA), was utilized to determine the functional group's presence on the date powder and its significance in adsorption. The analysis of FT-IR was conducted within the wavenumber region of 500–4000 cm^{-1}. The StablCal stabilized formazin turbidity standards was use by the turbidimeter The concentration of PS nanoplastics before and after batch adsorption experiments was determined by measuring the supernatant suspension's turbidity at different times. Before analysis, the instrument was calibrated with StablCal solutions from Hach, and the light scattered by the particles was measured in Formazine Nephelometric Unit (FNU).

2.4. Bach adsorption experiment

The experiments were conducted in a 150 mL Erlenmeyer flask containing 30 mL polypropylene suspension with an initial concentration from 5.0 to 40 mg L^{-1}. Before adding microplastic to the reactor, different amounts of adsorbent were added to the container.(Fig.1) The obtained suspension was shaken on a shaker at a speed of 100 rpm for 240 minutes at room temperature. The flask was removed from the shaker, and the concentration of PPNPs nanoplastics in the supernatant was measured. Before analysis, all samples were left to settle for another 30 min to minimize interference of carbon particles. A settling time of 30 min was determined experimentally. A control suspension system without PPNPs nanoplastics (with biochar and without PPNPs) was also performed to evaluate carbon particle interference by turbidity measurements. These data were used to calculate the concentration of PPNPs nanoplastics in the supernatant suspension. The flask contents were shaken for a particular time with a speed of 150 rpm.

The adsorbed amount of the PPNPs, q_e (mg g^{-1}), was computed using Equation 1.

$$q_e = \frac{(C_i - C_{eq})V}{m} \qquad \text{(Eq.1)}$$

Where q_e (mg g^{-1}) is the equilibrium adsorbed amount, and C_i (mg L^{-1}) is the initial concentration. C_{eq} (mg L^{-1}) is the equilibrium concentration, and V (L) is the

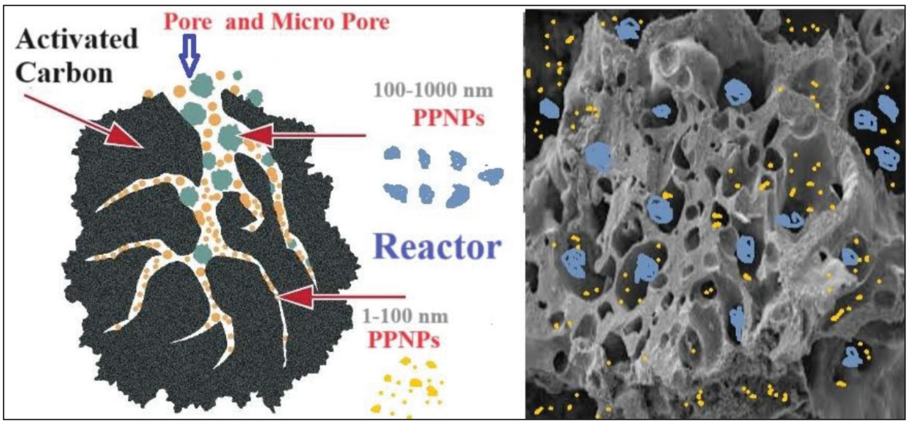

Fig.1. Adsorption polypropylene nanoplastics by activated carbon in reactor

volume of solution that contains mass (g) of adsorbent. Kinetic studies were performed to determine the adsorption rate of the PPNPs onto biochar in a separate experiment. Isotherms of the Langmuir and Freundlich models were applied to comprehend the adsorption mechanism (Eq.2). The adsorption capacity was calculated using Equation 3. The rate of the adsorption of the PPNPs was modelled using pseudo-first-order and pseudo-second-order kinetics. The linear equation of pseudo-first-order kinetic was used in Equation 4. The linear equation of the pseudo-second-order model is shown in Equation 5. The linear equation of the Langmuir isotherm model is expressed by Equation 6. The parameter R_L was calculated according to Equation 7, which can be used to expect the efficiency of the adsorbent. Based on the value of the R_L parameter, the process is irreversible if R_L is equal to zero, favourable if R_L is less than 1, linear if R_L is equal to 1 and unfavourable if R_L is greater than 1. The equation 8 was used for the Freundlich isotherm model.

$$\text{Mass of PPNPs adsorbed} = (C_i - C_f) \times V \qquad \text{(Eq.2)}$$

$$\text{Adsorption capacity} = \frac{M_{adsorbate}}{M_{adsorbent}} \qquad \text{(Eq.3)}$$

As Equation 3: C_i: Initial concentration of PPNPs in (mg L^{-1}), C_f: Final concentration of PPNPs in (mg L^{-1}), V: volume of the solution in (L), M_{PPNPs}: Mass of PPNPs in (g), $M_{adsorbent}$: Mass of adsorbent in (g)

$$\log(q_e - q_t) = \log(q_e) - \left(\frac{k_1}{2.303}\right)t \qquad \text{(Eq.4)}$$

Where k_1 is the rate constant of the pseudo-first-order adsorption process (min^{-1}), q_e is the equilibrium adsorbed amount of material per unit mass of adsorbent (mg g^{-1}), q_t is the equilibrium adsorbed amount of material per unit mass of adsorbent at time t (mg g^{-1}).

$$\frac{t}{q_t} = \frac{1}{k_2 q_e^2} - \frac{1}{q_e}t \qquad \text{(Eq.5)}$$

Where, k_2 is the rate constant of the pseudo-second-order adsorption process (g mg^{-1} min^{-1}), q_e is the equilibrium adsorbed amount of material per unit mass of adsorbent (mg g^{-1}), and q_t is the equilibrium amount of material adsorbed per unit mass at time t (mg g^{-1}). The rate constant value of k_2 was obtained using the slope and intercept from the plot of t/q_t versus t.

$$\frac{C_e}{q_e} = \frac{1}{k_L q_m} + \frac{C_e}{q_m} \qquad \text{(Eq.6)}$$

Where q_e is the equilibrium adsorbed amount of the material (mg g^{-1}), q_m is the maximum capacity of adsorption (mg g^{-1}), K_L is the Langmuir isotherm constant related to the energy of adsorption and is used to determine the affinity of the adsorbate to the adsorbent surface. C_e is the equilibrium material concentration in the solution (mg L^{-1}). The values of K_L and q_m constants were obtained using the slope and the intercept from the linear plot of C_e/q_e versus C_e.

$$R_L = \frac{1}{1+k_L C_i} \qquad \text{(Eq.7)}$$

Where K_L is the Langmuir isotherm constant determined in Equation 6, Ci is the initial concentration of the adsorbate.

$$\log q_e = \log K_f + \frac{1}{n}\log C_e \qquad \text{(Eq.8)}$$

Where q_e is the equilibrium concentration of the solid phase material per gram of adsorbent (mg g^{-1}), C_e is the equilibrium concentration of the material in the bulk phase (mg L^{-1}), K_f is the Freundlich isotherm constant (mg g^{-1}), and n is the intensity of adsorption. The values of K_f and n were obtained using the slope and the plot intercept between log q_e and log C_e.

3. Results and discussion

3.1. Characterization of Adsorbent

FT-IR, SEM, and XRD were employed to characterize the adsorption process of the PPMPs (R, Y, and E) onto biochar.

3.1.1. FTIR analysis

Based on the FT-IR analysis of the raw date fibers, peaks observed in the spectra indicated several functional groups at the surface, which serve as active sites for adsorption on the adsorbent surface. Figure 2 shows many bands at 3300.23 (related to O–H stretching vibration), 3010 (related to O–H stretching vibration), 1738.09 cm^{-1}(related to stretching vibration of C=O of carboxylic groups), 1710.09 (related to stretching vibration of C=O of carboxylic groups), 900.42(related to C=C, the C-H bond, and O-H in the plane deformation), and 528.89 (related to C-H deformation vibration and CH_2 rocking vibration –C–N– and –C–C– stretching) cm^{-1}. Also, SEM images and XRD of the morphology of biochar are shown in Figures 3 and 4.

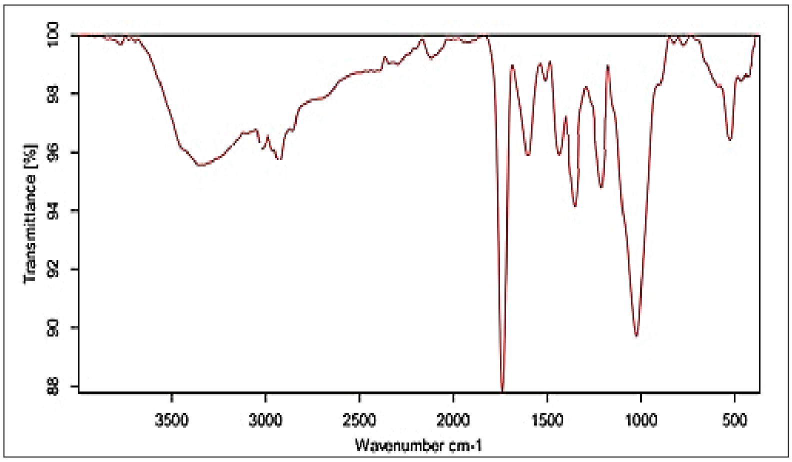

Fig. 2. FT-IR analysis of biochar derived from palm date fibers powder

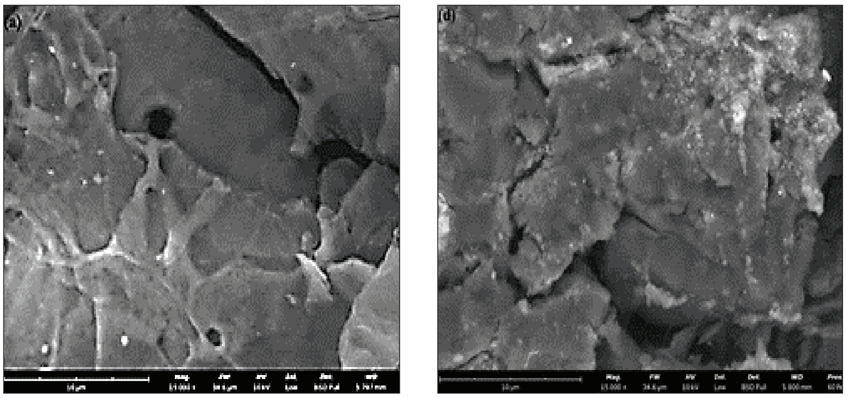

Fig. 3. SEM analysis of (a) date palm fibers biochar, (b) PPNPs on biochar

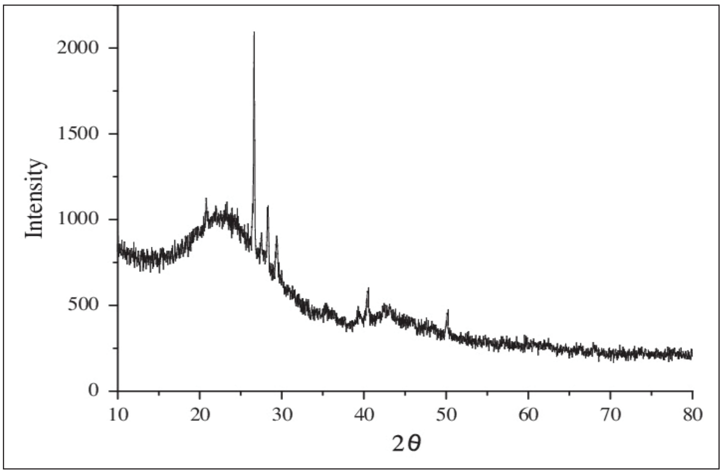

Fig. 4. XRD pattern of date palm fibers biochar

3.2. Batch adsorption

3.2.1. Influence of amount of adsorbent

The amount of adsorbent is a critical factor in the adsorption process. The variation in the adsorbent dosage impacts the adsorption of PPNPs onto biochar. Figure 5 shows the aschematic adsorption process. The removal efficiency and the adsorption capacity were investigated. The study was conducted using an adsorbent dosage of 10 to 100 mg. The optimal conditions used in this study were shaking at 150 rpm for 60 min at a concentration of 50 mg L^{-1}, a temperature of 25 ± 1 °C, and a pH of 7.0. As shown in Figure 6, the adsorption of the PPNPs was significantly increased up to 80 mg. Furthermore, while increasing the amount of biochar, the percent removal efficiency was increased, gradually decreasing the adsorption capacity.

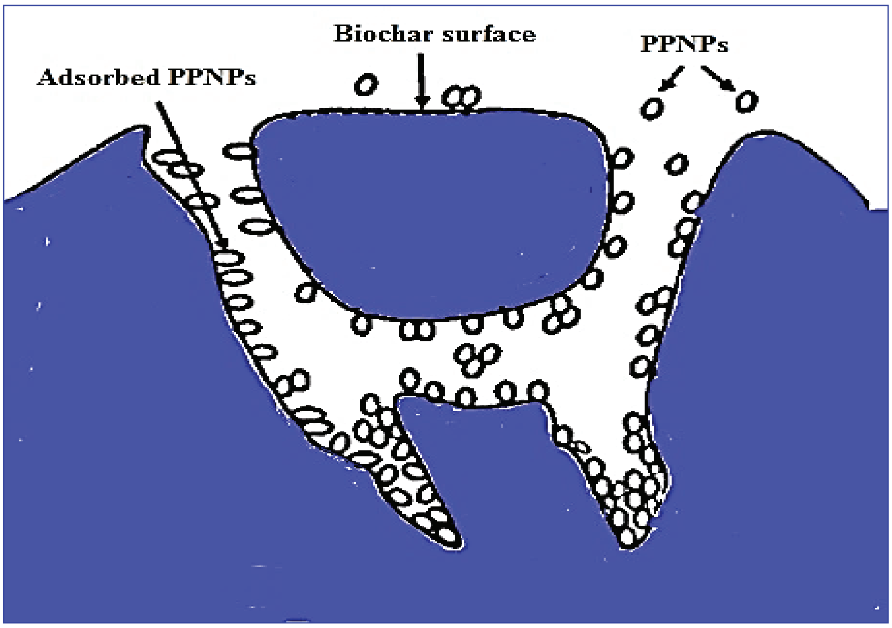

Fig. 5. Schematic adsorption process of PPNPs on biochar

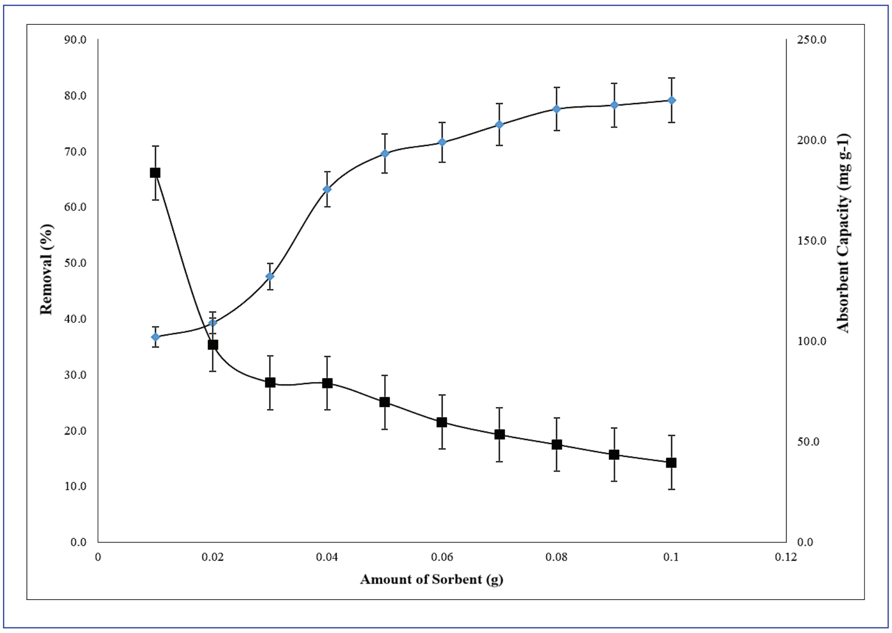

Fig. 6. Influence of adsorbent dosage on the adsorption of PPNPs on biochar[adsorbent dosage = 0.01-0.1 g, initial concentrations = 50 mg. L^{-1}; pH = 7.0, and contact time = 60 min, and T= 25 ±1°C]

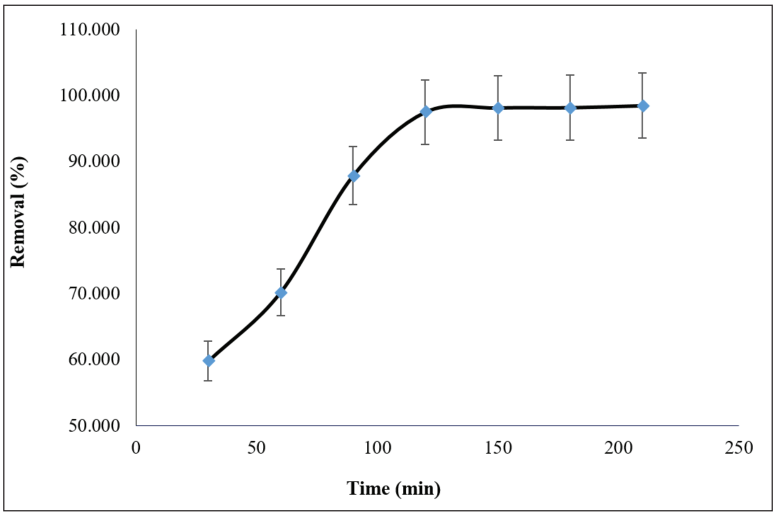

Fig. 7. Effect of contact time on the adsorption of PPNPs [time = 20-210 min., initial concentrations = 50 mg. L^{-1}; pH = 7.0, and T = 25 ±1°C]

3.2.2. Influence contact time

The impact of contact time on the removal efficiency of PPNPs by adsorbent was investigated. The optimal conditions used in this study were, a mass of adsorbent 80 mg of biochar, a temperature of 25 ± 1 °C, and a pH of 7.0. The removal percentages for the PPNPs increased significantly in the early stages. This behavior is related to the abundance of accessible active sites on the adsorbent. The results showed that the PPNPs needed 120 minutes to reach equilibrium which are shown in Figure 7.

3.2.3. Effect of PPNPs concentration

The variation in the initial concentration of the PPNPs impacts the removal percentage by biochar. The initial concentrations of 25 -150 mg L^{-1} were studied. The optimal conditions used in this study were obtained at 150 rpm shaking for 60 min, a mass of adsorbent 80 mg for PPNPs, a temperature of 25 ± 1 °C, and a pH of 7.0. The results of the PPNPs concentration on removal are shown in Figure 8. The results showed a significant increase at the beginning of the adsorption process. The maximum percent removal was investigated at a concentration of 50 mg L^{-1} for the PPNPs. Over time, the saturation of active biochar sites increased, resulting in a slight decrease in the adsorption capacity of biochar[30].

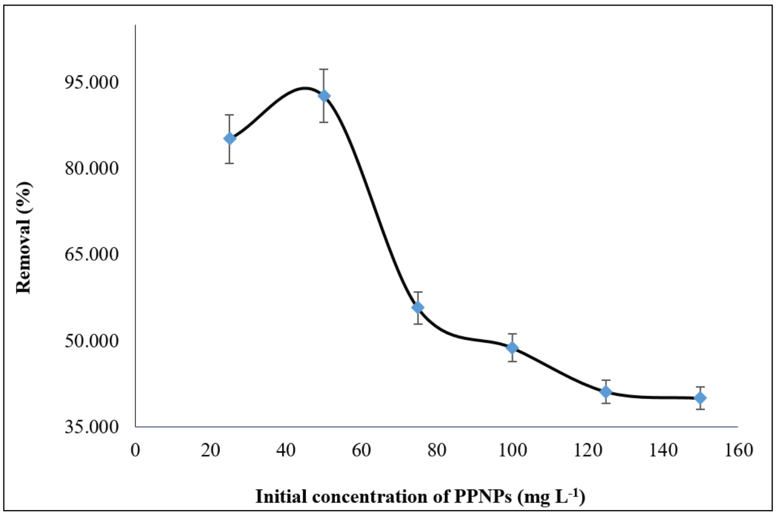

Fig. 8. Effect of initial concentration of PPNPs on the removal efficiency.[pH = 7.0, rpm = 150, and Temperature = 25 ±1°C]

3.2.4. Adsorption kinetic studies

Kinetics is an important step to determine the adsorption mechanism and to understand the biosorption steps that affect the processing speed. As a result of kinetic studies, it is possible to determine the rate of adsorption, and the retention time required for the used adsorbent to perform pollutant removal can be determined. The rate of adsorption is an important parameter in the selection of the most suitable adsorbent in the adsorption process. In determining the adsorption rate and rate constant, pseudo-first-order and pseudo-second-order kinetic models such as particle diffusion are applied to the xperimental data, and the kinetic model that best fits the experimental data is determined. Therefore, adsorption kinetic studies of PPNPs onto biochar were investigated using pseudo-first-order and pseudo-second-order kinetics. The results are summarized in Table 1 and Figure 9. R^2 values determined the kinetic model that best fits the adsorption of PPNPs onto biochar. Considering the reported R^2 values, the adsorption of PPNPs onto biochar followed pseudo-second-order kinetics. It was observed that the experimental data showed a high agreement to pseudo-second-order kinetic models ($R^2 > 0.989$ in all conditions examined for this models), When the model data obtained were evaluated considering all of the experiments.

3.2.5. Adsorption isotherms

Langmuir and Freundlich's isotherms were used to illustrate the mechanism of the adsorption process. The Langmuir and Freundlich isotherms constants for the adsorption of PPNPs on biochar were calculated (Table 2). It was found that the adsorption of PPNPs is a favorable process according to the obtained results for Langmuir isotherm.

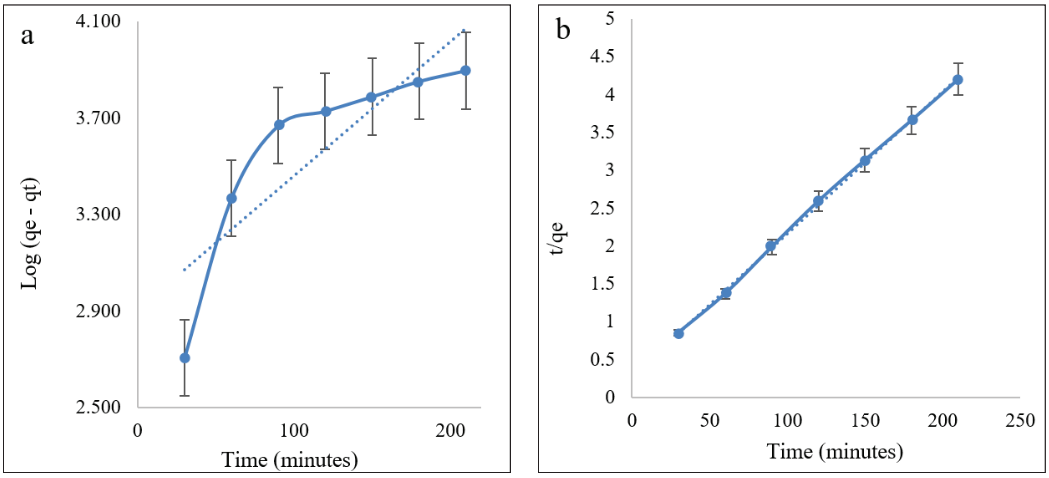

Fig. 9. Kinetic studies of the adsorption of PPNPs on biochar.

a: Psuedo First order **b:** Psuedo second order

Table 1. Adsorption of PPNPs by pseudo-first-order and pseudo-second-order kinetics

	First order kinetics		**Second order kinetics**	
	R^2	K_1 (min^{-1})	R^2	K_1 ($g.mg^{-1}min^{-1}$)
PPNPs	0.8512	$4.598X10^{-3}$	0.9899	$1.65X10^{-2}$

Table 2. The Langmuir and Freundlich isotherms constants of PPNPs adsorption biochar

	Langmuir			**Freundlich**		
	R_L^2	R_L	K_L	R_F^2	K_F	n
PPMPs	0.9019	0.1123	0.4521	0.9803	11.9652	2.7456

4. Conclusion

The adsorption mechanism of PPNPs on biochar derived from date fibers as an adsorbent was investigated. The results obtained from the characterization techniques (FT-IR, XRD, and SEM) confirm the adsorbent characterization. The optimal conditions for removing PPNPs were the amount of adsorbent 80 mg, contact time of 120 min, and initial concentration of 50 mg L^{-1} for the PPNPs. The isotherm data could be obtained according to the Langmuir model. The kinetic data of the PPNPs are modelled by the pseudo-second-order, revealing that the nature of the kinetic adsorption is chemical. The present study shows biochar derived from date fibers to be an effective adsorbent for removing PPNPs from aqueous solutions.

5. Aknowledgement

The authors thanks to Zabol University of Medical Sciences, Isfahan University of Medical Sciences, Birjand University of Medical Sciences, and Shahid Bahonar University of Kerman, Iran.

6. References

[1] Y. Yu, W.Y. Mo, T. Luukkonen, Adsorption behaviour and interaction of organic micropollutants with nano and microplastics–a review, Sci. Total Environ., 797 (2021) 149140. https://doi.org/10.1016/j.scitotenv.2021.149140

[2] F. Wang, M. Zhang, W. Sha, Y. Wang, H. Hao, Y. Dou, Y. Li, Sorption behavior and mechanisms of organic contaminants to nano and microplastics, Molecules, 25 (2020) 1827. https://doi.org/10.3390/molecules25081827

[3] W. J. Shim, S.H. Hong, S.E. Eo, Identification methods in microplastic analysis: a review, Anal. methods, 9 (2017) 1384-1391. https://doi.org/10.1039/C6AY02558G

[4] K. Zhang, A.H. Hamidian, A. Tubić, Y. Zhang, J.K. Fang, C. Wu, P.K. Lam, Understanding plastic degradation and microplastic formation in the environment: A review, Environ. Pollut., 274 (2021) 116554. https://doi.org/10.1016/j.envpol.2021.116554

[5] A.A. Koelmans, P.E. Redondo-Hasselerharm, N.H.M. Nor, V.N. de Ruijter, S.M. Mintenig, M. Kooi, Risk assessment of microplastic particles, Nat. Rev. Mater., 7 (2022) 138-152. https://doi.org/10.1038/s41578-021-00411-y

[6] F. Stock, C. Kochleus, B. Bänsch-Baltruschat, N. Brennholt, G. Reifferscheid, Sampling techniques and preparation methods for microplastic analyses in the aquatic environment–A review, TrAC Trends Anal. Chem., 113 (2019) 84-92.https://doi.org/10.1016/j.trac.2019.01.014

[7] M. Shahraki, M.R. Rezaei Kahkha, J. Piri, A. Sharafi, M. Kaykhaii, Microplastics in atmospheric dust samples of Sistan: sources and distribution, J. Environ. Health Sci. Eng., 20 (2022) 931-936. https://doi.org/10.1007/s40201-022-00833-y

[8] J.A.I. do Sul, M.F. Costa, The present and future of microplastic pollution in the marine environment, Environ. pollut., 185 (2014) 352-364. https://doi.org/10.1016/j.envpol.2013.10.036

[9] A.L. Andrady, Microplastics in the marine environment, Marine Pollut. Bull., 62 (2011) 1596-1605. https://doi.org/10.1016/j.marpolbul.2011.05.030

[10] Y. Zhang, T. Gao, S. Kang, S. Allen, X. Luo, D. Allen, Microplastics in glaciers of the Tibetan Plateau: evidence for the long-range transport of microplastics, Sci. Total Environ., 758 (2021) 143634. https://doi.org/10.1016/j.scitotenv.2020.143634

[11] W. Wang, W. Yuan, Y. Chen, J. Wang, Microplastics in surface waters of dongting lake and hong lake, China, Sci. Total Environ., 633 (2018) 539-545. https://doi.org/10.1016/j.scitotenv.2018.03.211.

[12] C. Jiang, L. Yin, X. Wen, C. Du, L. Wu, Y. Long, Y. Liu, Y. Ma, Q. Yin, Z. Zhou, Microplastics in sediment and surface water of west Dongting Lake and south Dongting Lake: abundance, source and composition, Int. J. Environ. Res. Public Health, 15

(2018) 2164. https://doi.org/10.3390/ijerph15102164

[13] S. Mintenig, M. Löder, S. Primpke, G. Gerdts, Low numbers of microplastics detected in drinking water from ground water sources, Sci. Total Environ., 648 (2019) 631-635. https://doi.org/10.1016/j.scitotenv.2018.08.178

[14] M. Kosuth, S.A. Mason, E.V. Wattenberg, Anthropogenic contamination of tap water, beer, and sea salt, PLOS One, 13 (2018) e0194970. https://doi.org/10.1371/journal.pone.0194970

[15] M. Padervand, E. Lichtfouse, D. Robert, C. Wang, Removal of microplastics from the environment. A review, Environ. Chem. Lett., 18 (2020) 807-828. https://doi.org/10.1007/s10311-020-00983-1

[16] W. Liu, J. Zhang, H. Liu, X. Guo, X. Zhang, X. Yao, Z. Cao, T. Zhang, A review of the removal of microplastics in global wastewater treatment plants: Characteristics and mechanisms, Environ. Int., 146 (2021) 106277. https://doi.org/10.1016/j.envint.2020.106277

[17] M. Shen, B. Song, Y. Zhu, G. Zeng, Y. Zhang, Y. Yang, X. Wen, M. Chen, H. Yi, Removal of microplastics via drinking water treatment: Current knowledge and future directions, Chemosphere, 251 (2020) 126612. https://doi.org/10.1016/j.chemosphere.2020.126612

[18] R. Ahmed, A.K. Hamid, S.A. Krebsbach, J. He, D. Wang, Critical review of microplastics removal from the environment, Chemosphere, 293 (2022) 133557. https://doi.org/10.1016/j.chemosphere.2022.133557

[19] F. Golbabaei, A. Vahid, A. Faghihi Zarandi, A novel nano-palladium embedded on the mesoporous silica nanoparticles for mercury vapor removal from air by the gas field separation consolidation process, Appl. Nanosci., 12 (2022) 1667-1682. https://doi.org/10.1007/s13204-022-02366-0

[20] M. Habibnia, A. Rashidi, A.F. Zarandi, M.D. Mobarake, Simultaneously speciation of mercury in water, human blood and food samples based on pyrrolic and pyridinic nitrogen doped porous, graphene nanostructure, Food Chem., 403 (2023) 134394. https://doi.org/10.1016/j.foodchem.2022.134394

[21] M.K. Abbasabadi, F. Hosseini, Nanographene oxide modified phenyl methanethiol nanomagnetic composite for rapid separation of aluminum in wastewaters, foods, and vegetable samples by microwave dispersive magnetic micro solid-phase extraction, Food Chem., 347 (2021)129042. https://doi.org/10.1016/j.foodchem.2021.129042

[22] N. Esmaeili, J. Rakhtshah, Ultrasound assisted-dispersive-modification solid-phase extraction using task-specific ionic liquid immobilized on multiwall carbon nanotubes for speciation and determination mercury in water samples, Microchem. J., 154 (2020) 104632. https://doi.org/10.1016/j.microc.2020.104632

[23] R. Ashouri, Dynamic and static removal of benzene from air based on task-specific ionic liquid coated on MWCNTs by sorbent tube-headspace solid-phase extraction procedure, Int. J. Environ. Sci. Technol., 18 (2021) 2377-2390. https://doi.org/10.1007/s13762-020-02995-4

[24] J. Rakhtshah, A rapid extraction of toxic styrene from water and wastewater samples based on hydroxyethyl methylimidazolium tetrafluoroborate immobilized on MWCNTs by ultra-assisted dispersive cyclic conjugation-micro-solid phase extraction, Microchem. J., 170 (2021) 106759. https://doi.org/10.1016/j.microc.2021.106759

[25] P. Paydar, A novel method based on functionalized bimodal mesoporous silica nanoparticles for efficient removal of lead aerosols pollution from air by solid-liquid gas-phase extraction, J. Environ. Health Sci. Eng., 18 (2020) 177–188. https://doi.org/10.1007/s40201-020-00450-7

[26] S. Teimoori, An immobilization of aminopropyl trimethoxysilane-phenanthrene carbaldehyde on graphene oxide for toluene extraction and separation in water samples, Chemosphere, 316 (2023) 137800. https://doi.org/10.1016/j.chemosphere.2023.137800

[27] S. Teimoori, A.H. Hassani, M. Panahi, N. Mansouri, Rapid extraction of BTEX in water and milk samples based on functionalized multi-walled carbon nanotubes by dispersive homogenized-micro-solid phase extraction, Food Chem., 421 (2023) 136229. https://doi.org/10.1016/j.foodchem.2023.136229

[28] S. Teimoori, A.H. Hassani, New extraction of toluene from water samples based on nano-carbon structure before determination by gas chromatography, Int. J. Environ. Sci. Technol., 20 (2023) 6589–6608. https://doi.org/10.1007/s13762-023-04906-9

[29] A.H. Tahir, A.H.M. Al-Obaidy, F.H. Mohammed, Biochar from date palm waste, production, characteristics and use in the treatment of pollutants: A Review, IOP Conf. Ser. Mater. Sci. Eng., 373 (2020) 012171. https://doi.org/10.1088/1757-899X/737/1/012171

[30] R. Mao, M. Lang, X. Yu, R. Wu, X. Yang, X. Guo, Aging mechanism of microplastics with UV irradiation and its effects on the adsorption of heavy metals, J. Hazard. Mater., 393 (2020) 122515. https://doi.org/10.1016/j.jhazmat.2020.122515

Anal. Methods Environ. Chem. J. 6 (4) (2023) 76-92

Research Article, Issue 4
Analytical Methods in Environmental Chemistry Journal
Journal home page: www.amecj.com/ir

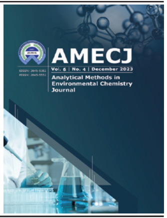

Removal of manganese (II) in water samples by the aeration-filtration process and determination based on 5-Br-PADAP ligand by cathodic stripping voltammetry

Abdoulkadri Ayouba Mahamane*[a,b,c], **Boubié Guel**[b], **and Paul-Louis Fabre**[c]
[a] *Materials, Water, Environment Laboratory, Faculty of Sciences and Techniques/University Abdou Moumouni, BP 10662, Niamey - Niger*
[b] *Laboratory of Materials and Molecular Chemistry, U.F.R –SEA/University Joseph Ki-ZERBO, Ouagadougou 03 BP 7021, Burkina Faso*
[c] *Chemical Engineering Laboratory UMR CNRS 5503 Bât.2R118 – 1 route de Narbonne 31062 Toulouse Cedex09, France*

ARTICLE INFO:
Received 7 Aug 2023
Revised form 24 Oct 2023
Accepted 27 Nov 2023
Available online 28 Dec 2023

Keywords:
Manganese,
Removal,
5-Br-PADAP Ligand,
Aeration-filtration,
Cathodic Stripping Voltammetry,

ABSTRACT

In this study, manganese (Mn II) was determined in aqueous media by an electrochemical method, and its removal was evaluated using the aeration-filtration process (AFP). An electrochemical sensor based on carbon paste (EPC) modified with the 5-Br-PADAP ligand was used to measure Mn (II) in aqueous media. Through the optimization of analytical parameters in cathodic stripping voltammetry (CSV), real boreholes and well water samples could be analyzed for manganese content. The optimum parameters such as preconcentration potential (1100 mV), preconcentration time (240s), 5-Br-PADAP ligand concentration (20 µmol L^{-1}), and electrode rotation speed during pre-concentration (1000 rpm) were studied and optimized. The detection limit (LOD) is estimated at 3×10^{-7} mol L^{-1} with a relative standard deviation (RSD) of 3.36%. The real samples showed that some water points have more concentration than the standard. A simple, effective, inexpensive, and rural-friendly method was used for treating manganese-rich water. Following the aeration phase, the sand and gravel column was filtered to remove manganese (II) from the water. The removal efficiency of Mn was obtained at a rate of 74.8- 84.5% and more than 95% after two hours of aeration and 1 hour at pH 8 for real samples.

1. Introduction

Manganese is a trace element in the environment. Besides being essential for human growth, it also plays an important role in carbohydrate and lipid metabolism and catalyzes certain enzymatic reactions [1]. Due to its antagonistic nature towards calcium, it may also cause irreversible neurological disorders. These disorders generally occur when manganese levels exceed 2 mg L^{-1} [2]. Manganese is mainly found in ores such as pyrolusite (MnO_2) and rhodochrosite ($MnCO_3$). It is widely used in metallurgy (steels, alloys, welds), the electrical industry (electrodes, dry cells), the chemical industry (catalysts, colorants), the glass and ceramic industries, and in fuel production (organometallic additives). Depending on pH, dissolved oxygen, and complexing agents, manganese is found in water in different valences (II, III, and IV), soluble or suspended forms, or complexes. Occasionally,

---

*Corresponding Author: Abdoulkadri Ayouba Mahamane
Email: kadayouba@gmail.com
https://doi.org/10.24200/amecj.v6.i04.313

groundwater contains a level of 1 mg L^{-1}, especially when attacked by water from the support rock in a reducing environment or when certain bacteria are active. Under these conditions, it is often associated with iron, with which it co-precipitates by oxidation. Generally, surface waters contain less than 0.05 mg L^{-1} [1]. Manganese can give water an unpleasant taste. Furthermore, even at the lowest dose (0.02 mg L^{-1}), it can form a black layer (on pipes), making the water unattractive when detached. Even small quantities (0.1 mg L^{-1}) can stain enamel and linen, which is a problem from a domestic standpoint. As a result, it stimulates the growth of siderobacteria (Galllionella) in water treatment plants, disrupting the operation of sand filters and resulting in pipe deposits. It can, however, be used in its heptavalent state as permanganate to eliminate organic matter, giving water an unpleasant taste. The WHO recommends a provisional guideline value of 0.4 mg L^{-1} for water intended for human consumption [1, 3]. Various analytical methods have been used to analyze manganese. The two most used methods are flame atomic absorption spectrometry (F-AAS) and UV-visible spectrophotometer [4]. Implementing these methods is time-consuming, requiring long sample time and pretreatment of samples before determining the element content of the matrix under study [5]. Electrochemical methods are an appealing alternative for detecting manganese traces due to their rapidity, high sensitivity, and selectivity. These methods have the advantage of working with a small sample quantity and without pretreatment of the sample [5]. Anodic stripping voltammetry (ASV) with mercury drop or mercury film electrodes is the most widely used method for determining trace metal concentrations in electrochemistry [6, 7]. Since manganese is poorly soluble in mercury and requires a high overpotential to be deposited on mercury, this method presents some analytical challenges for manganese determination [8]. The potential of the peak associated with manganese deposition on the mercury electrode and the potential of the hydrogen reduction wave are close. Further, manganese determination is difficult due to intermetallic compounds formed with copper [5]. All these factors considerably reduce the sensitivity of the method. Several alternatives have been described in the literature as solutions to these difficulties. Several solid electrodes (graphite, glassy carbon, carbon fiber, platinum, boron-doped diamond, etc.) have been used to measure manganese traces through cathodic stripping voltammetry (CSV) [9, 10] after oxidized Mn (II) to MnO_2 [11]. In addition, it is possible to perform voltammetry using a manganese complex adsorbed on the surface of a mercury or solid electrode after the complex has been pre-concentrated on the electrode surface. Several researchers have used cathodic stripping voltammetry (CSV) of an adsorbed complex to determine various inorganic cations, including metals that do not form amalgams with mercury. As a result, metals such as Fe, Mn, Ni, Co, Al, Se, As, and Ti have been determined in natural waters after complexation of the ligands cation (such as dimethylglyoxime, catechol or oxine), which is followed by adsorption and cathodic stripping. The CSV technique has achieved detection limits of 10^{-12} M [12]. Azo compounds are compounds with the functional group R-N=N-R’ in their structure. The 2-(5’-Bromo-2’-pyridylazo)-5-diethylaminophenol group (5-Br-PADAP) is an azo compound used as a ligand capable of forming complexes with several metal ions. Cathodic stripping voltammetry (CSV) has successfully been used to determine several metal cations, including Mn (II), Cu (II), Fe (III), V(V), Bi (III), Cr (III), Co (II), and Ti (IV) [13, 14]. In this paper, cathodic stripping voltammetry is used for electrochemically determining manganese (II) based on the work of E. Ghoneim *et al.* [13]. Numerous studies have examined manganese removal from water [15-17]. Processes commonly used include chemical oxidation with chlorine derivatives, ozone or permanganate, and biological methods. While it produces good yields, these processes are not feasible in rural areas because of their high cost and toxicity [2]. In this article, the first objective is to develop an electrochemical sensor for manganese (II) determination using 2-(5’-bromo-2’-pyridylazo)-5-diethylaminophenol (5-Br-PADAP) ligand-modified carbon paste. In an aqueous matrix, optimal analytical parameters are established for the electrochemical determination of manganese. As part of a real-life evaluation of the electrochemical sensor, manganese pollution in boreholes and well waters were investigated near Ouagadougou (Burkina Faso). Considering manganese pollution in rural areas of developing countries, the second objective of this article is to propose a simple method for removing manganese from water.

2. Experimental

2.1. Chemicals and solutions

Ultrapure water (milli-Q water) was used for all solutions. Mn^{2+} (10^{-3} mol L^{-1}) solution was prepared by dissolving manganese sulphate (purity > 99.99%, Sigma Aldrich, CAS N.: 10034-96-5) in 0.1 M perchloric acid (trace analysis, Sigma Aldrich, CAS N.: 7601-90-3). A certified manganese standard (1.0 g L^{-1}) (Certipur Merck, CRM 119789) was also used to prepare standard solutions. The supporting electrolyte was a 0.1 mol L^{-1} acetate buffer (pH 4.5) prepared with acetic acid (Normapur ACS 95%, VWR, CAS N.: 64-19-7) and sodium acetate (99.5%, Sigma Aldrich, CAS N.: 127-09-3). The ligand used to complex Mn^{2+} ions is 2-(5’-Bromo-2’-pyridylazo)-5-diethylaminophenol (5-Br-PADAP, 97% Sigma Aldrich, CAS N.: 14337-53-2). 5-Br-PADAP solution is obtained by dissolving the appropriate quantity in pure methanol (99.8% Sigma Aldrich, CAS N.: 67-56-1).

2.2. Carbon paste electrode preparation

The carbon paste electrode used was made by mixing 2.0 g of graphite powder (diameter < 0.1 mm, 99.9995% Alfa Aesar, CAS N.: 7782-42-5) and 0.72 mL paraffin oil (Sigma Aldrich, CAS N.: 8012-95-1) in an agate mortar until a homogeneous paste was obtained. The paste is manually inserted into the cylindrical cavity of the rotating disk electrode’s cylindrical tip. The surface of the tip is then smoothed on clean paper.

2.3. Apparatus

The experimental set-up used for DPCSV (Differential Pulse Cathodic Stripping Voltammetry) and Cyclic Voltammetry (CV) analyses is a PGstat potentiostat-galvanostat model Voltalab 50 (Radiometer, Copenhagen) controlled by a microcomputer running Volta Master software (version 4.0). The dropping mercury electrode (DME) 150 measuring stand comprises a cell (25 mL) containing an EDI 101 rotating disk electrode with carbon paste tip (diameter 3 mm), a silver chloride, Ag/AgCl, 3 mol L^{-1} KCl reference electrode (E_{ref}=0.205 V/ENH. Also, radiometer model TR020), a platinum auxiliary electrode (Radiometer model TM020) and a nitrogen supply for solution bubbling were used. The morphology and chemical composition of the surface-adsorbed complex were obtained using a scanning electron microscope (SEM controlled by a microcomputer running TM-100 software, Hitachi, Japan) coupled to an EDX system (Swift ED-TM software) for chemical analysis of the electrode surfaces.

2.4. Analytical procedure for manganese (II) analysis

The three electrodes are immersed in the electrochemical cell containing the electrolyte. During the study of the ligand alone, the supporting electrolyte consists of 10 mL of acetate buffer solution and 20 µmol L^{-1} of 5-Br-PADAP (10^{-3} mol $L^{-1)}$. For the analysis of the Mn (II)-(5-Br-PADAP) complex, the supporting electrolyte contains 5.0 mL of acetate buffer solution, 20 µmol L^{-1} of 5-Br-PADAP (0.001 M) and 5 mL of the Mn^{2+} ion solution were used. An anodic pre-concentration potential is applied to the electrode under constant rotation of 1000 rpm. The differential pulse cathodic stripping voltammetry is used for recording the voltammogram after 10 seconds of pre-concentration (Fig. 1). A simple standard addition method is used to determine the exact concentration of Mn^{2+} ions in the borehole and well waters.

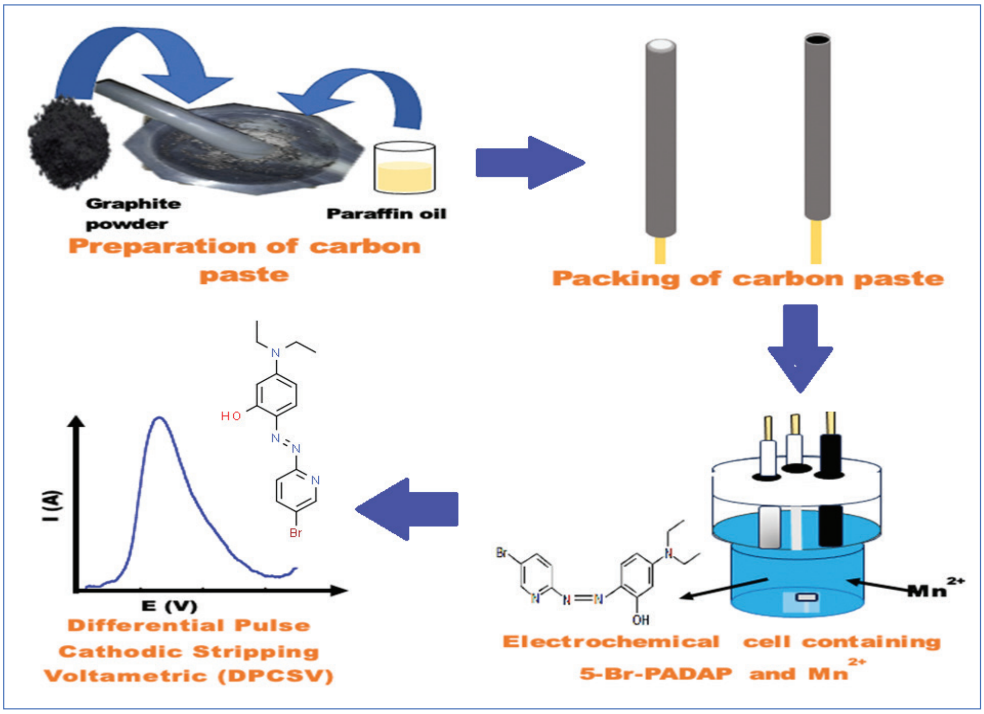

Fig. 1. Schema of analytical procedure

2.5. Real samples of borehole and well waters

The present method is applied to the determination of Mn^{2+} in the borehole and well waters from the locality of Yamtenga, south-east of the city of Ouagadougou, with UTM coordinates: X = 669126, Y = 1363944. Samples were taken at 11 water points (9 boreholes and two wells) every three months for one year.

2.6. Raw materials for manganese (II) removal

Sand samples were collected in the southern part of the town of Bobo-Dioulasso in Burkina Faso from a sand zone extensively exploited by residents. Three (03) sand samples were collected from different sites in this area. In the text, they were referenced to facilitate their identification. Table 1 summarizes the references for the sand samples and the sampling locations. The S_1 and S_3 samples belong to the *Kawara-Sindou* formation, while the S_2 sample belongs to the *Tabalédougou* formation. These geological formations comprise fine, very fine, or coarse sandstone-quartzite. The gravel sample was collected in the commune of Gomboussougou, in the Zoundweogo province of the Center Sud region of Burkina Faso (Table 1). The gravel sample was found in a waterway formed by erosion of alkaline granite. Alkaline granite, clear to mesocratic, has a medium to coarse-grained texture, whether porphyritic or not. In addition to the presence of alkali feldspars and quartz, this rock is also characterized by the presence of alkaline (sodic) ferromagnesian minerals.

2.7. Granulometric characterization of raw materials

Studying a sample's particle size enables us to determine the distribution of grain sizes. One of the

Table 1. Reference names of sand and gravel samples and their geographical coordinates

Sample	Characteristics	GPS coordinates (UTM)	
		X	Y
S_1	Red-brown sand	970 368	946 233 1
S_2	Pink sand	091 369	360 234 1
S_3	White sand (coarse-grained)	373 369	557 234 1
GOM	Fine gravel	633 739	074 246 1

most common methods of determining grain size is to sieve through sieves with decreasing cross-sections. It allows us to distinguish between the "pass," or quantity of product that passes through the mesh, and the "reject," or quantity that remains in the sieve. The sum of pass and reject for a given sieve equals the total sum of the product tested [18].
To determine the particle size of sand, three samples were analyzed. After washing and drying, a 100 g sample was sieved through 7 AFNOR standardized sieves. The mesh sizes in mm are 1, 0.5, 0.4, 0.35, 0.25, 0.20, 0.16, and 0.125. The calculation of the weight percentage of each refusal and that of each pass are given by Equations 1 and 2 [2].

$$\% \text{ Rejection} = (A/B)\times 100 \qquad \text{(Eq. 1)}$$

$$\% \text{ Passing} = ((B-A)/B)\times 100 \qquad \text{(Eq. 2)}$$

With: A, weight of refused material in g and B, initial weight.
These percentages are used to establish the granulometric curve of the sand samples and determine the Coefficient of Uniformity (CU) as Equation 3.

$$CU = d_{60}/d_{10} = d_{40}/d_{90} \qquad \text{(Eq. 3)}$$

Where d_{60} (d_{40}) is the diameter through which 60% of the sand passes (retaining 40% of the sand) and d_{10} (d_{90}) is the diameter through which 10% of the sand passes (including 90% of the sand).
Knowing the CU lets us know whether the sand is homogeneous and, therefore, suitable for filtration. Homogeneity is achieved if $1.2 \leq CU \leq 1.8$ [2]. The diameter through which 10% of the sand can pass is called the effective size, $ES = d_{10}$ [19]. Gravel particle size analysis was also carried out according to the abovementioned procedure. AFNOR standard sieves have mm dimensions (6, 4, 3.15, 2.5, 2, 1.6, 1.25, 1).

2.8. Filter description and analytical procedure for removal tests

To implement the method of aeration followed by filtration, we carried out laboratory-scale tests using a filtration column. The column is shown in Figure 2, with the following characteristics: length 43 cm, outside diameter 4 cm, and inside diameter 3.2 cm. The column is filled with a 10 cm layer of gravel, topped with 20 cm of sand. The sand and gravel are washed thoroughly with water to remove any impurities that may contaminate the treated water. For the manganese removal tests, we intentionally spiked ultrapure water with Mn (II) at 5 mg L^{-1} (an arbitrary concentration corresponding to water with

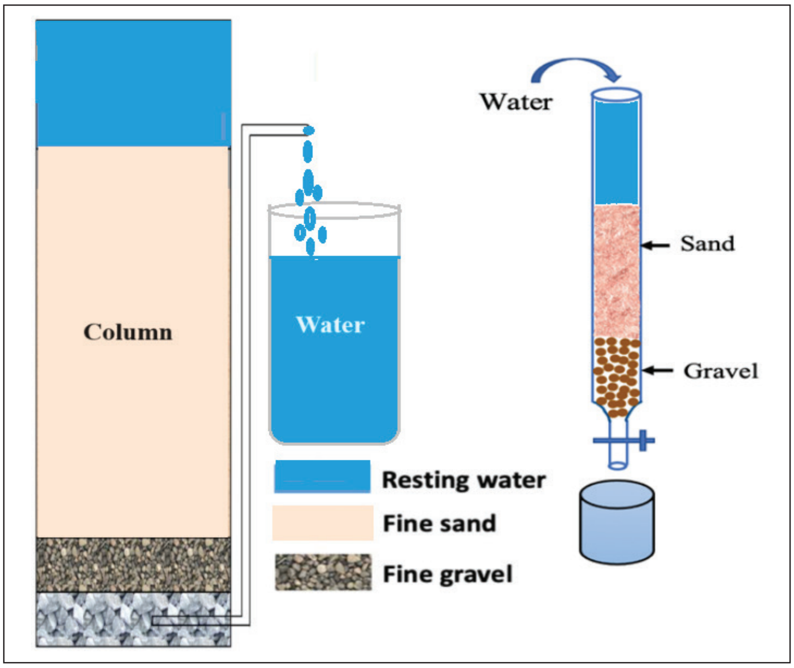

Fig. 2. Filtration column for aeration-filtration

a high Mn (II) content). This water was aerated with atmospheric oxygen for a total of 120 min. The water was passed through the column at time intervals, and the residual Mn (II) concentration was determined. The analysis was conducted at three different pH levels (6, 7, and 8). These three pH values generally cover the pH of groundwater. Concentrated NaOH sodium hydroxide and HCl hydrochloric acid were used to adjust the pH of the water. The method for determining Mn^{2+} ions is described in section 2.4.

3. Results and discussion

3.1. Voltammetric determination of manganese (II)

3.1.1.Cyclic and differential pulse voltammetry

Figure 3a shows the voltammogram recorded in a solution of the supporting electrolyte containing only Mn^{2+} ions. Due to the Results, no anodic or cathodic peaks are recorded with or without pre-concentration potential. Based on the contact of Mn^{2+} ions with the ligand, the voltammogram is shown in Figure 3b. Also, a cathodic sweep from 1.1 V to 0.4 V was performed without pre-concentration potential by a return sweep. In Figure 3b, we obtain an anodic signal, at 0.80 V, but no significant signal exists in the cathodic direction. After pre-concentration at a potential of +1.1 V for 2 min under constant electrode rotation, we record cyclic voltammetry, a cathodic peak at 0.644 V, in addition to an intense anodic peak at 0.84 V (Fig. 3c). The increase in ligand and manganese concentration also leads to an increase in the intensities of the two peaks and. The difference ΔE between the potentials of the anodic and cathodic peaks in the voltammogram of Figure 3c is equal to 0.22 V, reflecting the high degree of irreversibility of the processes involved [20]. In DPCSV, as expected, we obtain an intense, better-resolved cathodic peak (Fig. 4). DPCSV will be used to analyze manganese in wells and boreholes water. Consequently, the accumulation process

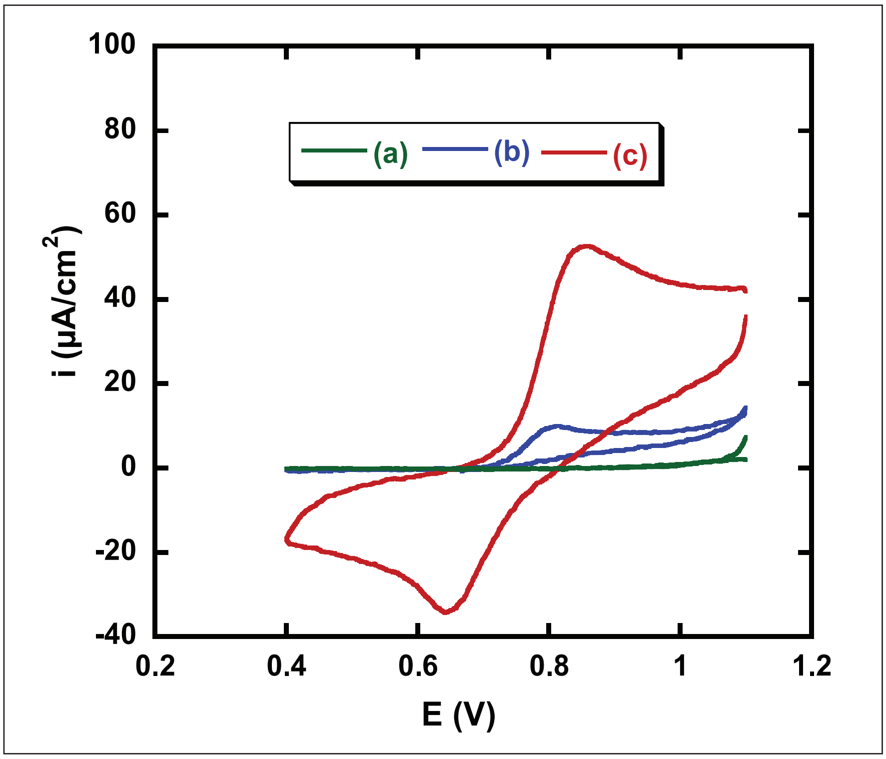

Fig. 3. Cyclic voltammograms at the carbon paste electrode at 25 mV/s: (**a**) in the supporting electrolyte (acetate buffer 0.1 mol.L^{-1} pH 4.5) containing Mn^{2+} ions 4 ×10^{-6} mol.L^{-1} with or without pre-concentration potential; (**b**) in the supporting electrolyte containing Mn^{2+} ions 4×10^{-6} mol.L^{-1} and ligand 5-Br-PADAP 20 µmol.L^{-1} without pre-concentration potential, cathodic then anodic direction (from 1.1 V to 0.4 V); (**c**) same conditions as in (b), except that a pre-concentration potential is imposed (pre-concentration potential: 1.1 V; pre-concentration time: 2 min; electrode rotation: 1000 rpm)

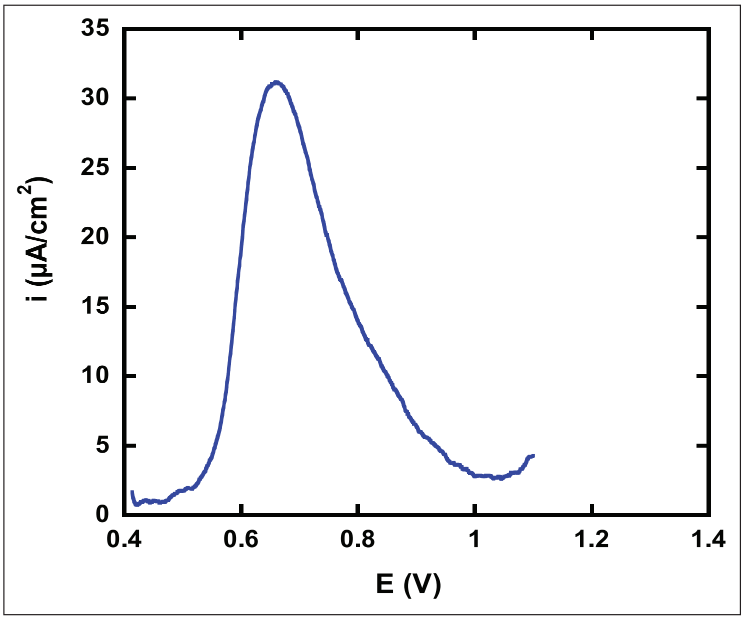

Fig. 4. DPCSV of a standard solution of Mn^{2+} ions 1.5 ×10^{-6} mol.L^{-1} in the supporting electrolyte after addition of 20 µmol.L^{-1} of the 5-Br-PADAP ligand, with pre-electrolysis before voltammogram recording (pre-concentration potential: 1.1 V; pre-concentration time: 2 min; electrode rotation: 1000 rpm)

at positive potential enhances the adsorption of the complex to the electrode surface. This is not a simple accumulation of material in the interfacial zone but a reactive phenomenon leading to specific adsorption on the electrode surface.

3.1.2. Effect of pre-concentration potential

Figure 5 illustrates the variation of peak current with pre-concentration potential. The highest peak current was obtained at a potential of 1100 mV. Therefore, this potential was chosen as the pre-concentration potential.

3.1.3. Effect of pre-concentration time

Cathodic stripping peak current was studied by varying pre-concentration time between 0 and

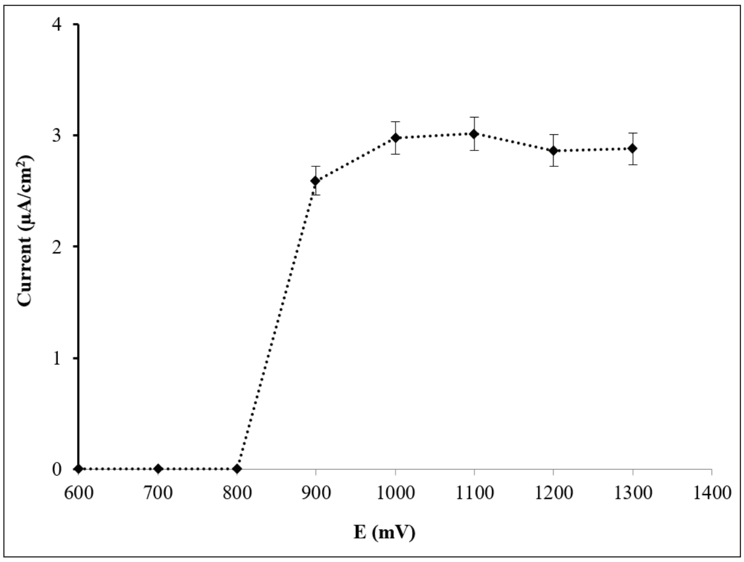

Fig. 5. Effect of pre-concentration potential on reduction peak current (pre-concentration time 2 min, rotation speed 400 rpm, 5-Br-PADAP: 50 µmol L^{-1})

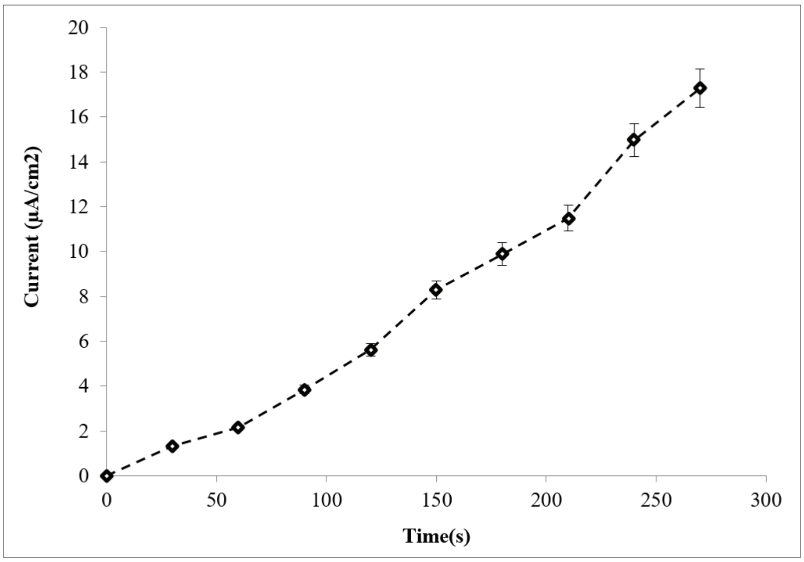

Fig. 6. Effect of pre-concentration time on reduction peak current
(pre-concentration potential 1100 mV, stirring 400 rpm, 5-Br-PADAP: 50 µmol L^{-1}, pulse amplitude 40 mV)

300 seconds. Figure 6 illustrates the increase in current with increasing deposition time. For further analysis, 240 seconds were selected as the pre-concentration time.

3.1.4.Effect of electrode rotation speed

The influence of electrode rotation speed during the pre-concentration step was studied by varying this speed between 0 and 1000 rpm. The results indicate that the redissolution current increases with the rotation speed of the electrode. For the remainder of our work, we used the highest value provided by our speed controller, i.e., 1000 rpm.

3.1.5.Effect of ligand concentration

Various concentrations of 5-Br-PADAP ligand are tested, ranging from 0 to 60 µmol L^{-1}. Figure 7 shows that the redissolution current increases with 5-Br-PADAP concentration, picking at 20 µmol L^{-1} and stabilizing. Therefore, the optimum value for this parameter is 20 µmol L^{-1}.

3.1.6. Morphological study and chemical composition of the electrode surface

The morphology and chemical composition of the

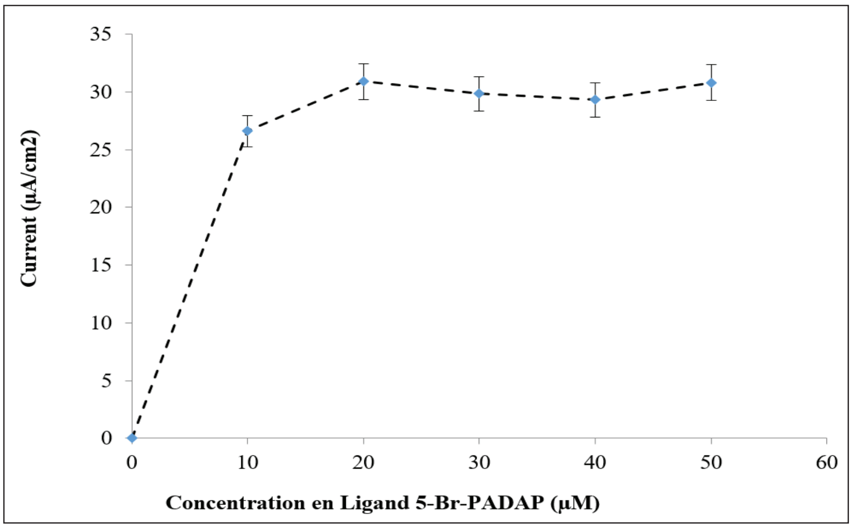

Fig. 7. Effect of 5-Br-PADAP ligand concentration on reduction peak current.
(pre-concentration potential 1100 mV, pre-electrolysis time 4 min, electrode rotation speed 1000 rpm, pulse amplitude 40 mV)

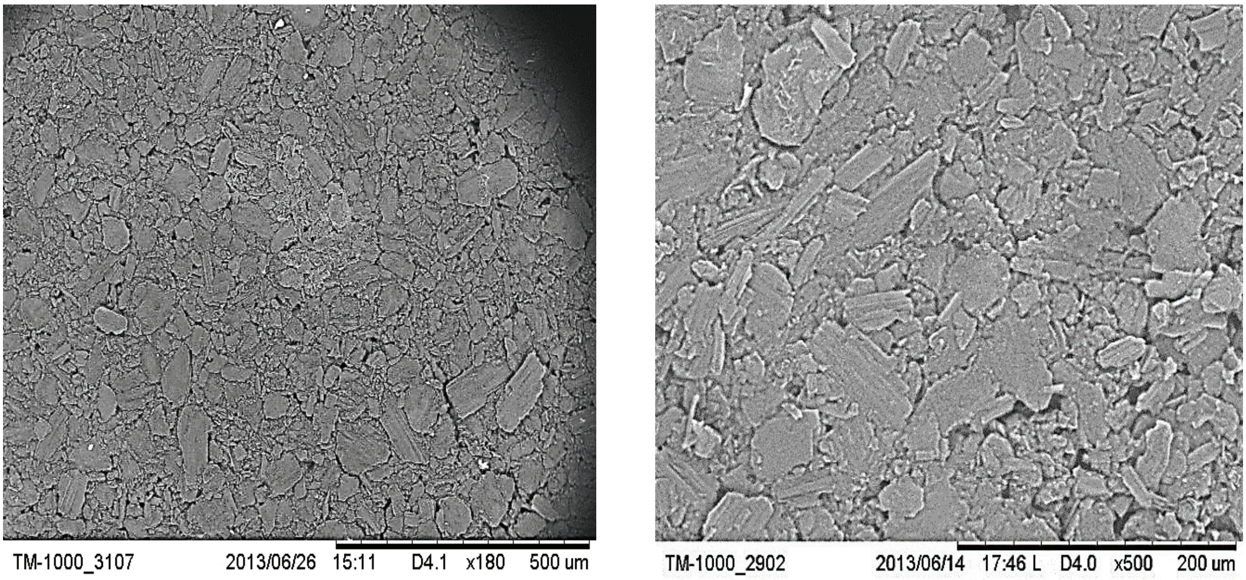

Fig. 8. SEM images at two resolutions of modified carbon paste after deposition of the manganese complex from a solution of the supporting electrolyte (acetate buffer 0.1 mol L^{-1} pH 4.5) containing the ligand 20 µmol L^{-1} and the Mn^{2+} ions 10^{-4} mol L^{-1}, the deposition potential being +1.1 V)

complex on the surface of the carbon paste electrode were established by scanning electron microscopy (SEM) combined with EDX chemical analysis. Figure 8 shows the appearance of the carbon paste electrode at a pre-concentration potential of 1.1 V carried out in a solution of the supporting electrolyte containing Mn^{2+} ions at a concentration of 10^{-4} mol L^{-1}. Different diameter plates were found assembled, identifying a chemically modified surface by a non-homogeneous complex film, i.e. a rough deposit [21]. The EDX spectrum corresponding to the image shows the presence of manganese (100% Mn and no trace of any other metal) in the layer formed on the surface at a potential of 1.1 V.

3.1.7.Analytical application

The modified electrode response towards Mn^{2+} is determined by plotting calibration curves obtained from successive additions of Mn^{2+} ions (Fig. 9). The calibration line has a correlation coefficient of 0.997, which is satisfactory for the concentration range studied. The limit of detection (LOD) is calculated as Equation 4 [22].

$$LOD= (k \times Sy)/a \qquad \text{(Eq. 4)}$$

k is a constant equal to 3, Sy is the residual standard deviation between measurements, and a is the slope of the calibration line. The calculated detection limit, in the concentration range 10^{-6} – 7×10^{-6} mol L^{-1}, is 3×10^{-7} mol L^{-1} (0.016 mg L^{-1}). Then, the standard addition method assays a certified manganese standard at 1 mg L^{-1}. The recovery rate obtained was of the order of 97%. In terms of precision, the i = f(E) curve was recorded n times for a constant Mn^{2+} concentration. For n=5 and $[Mn^{2+}] = 2 \times 10^{-6}$ mol L^{-1}. A standard deviation between measurements of 0.75 was found. The calculated RSD (Relative Standard Deviation) is 3.36%.

Overall, these results are satisfactory and demonstrate that the method is reliable for determining the concentration of Mn^{2+} ions in solution. Therefore, the technique was applied

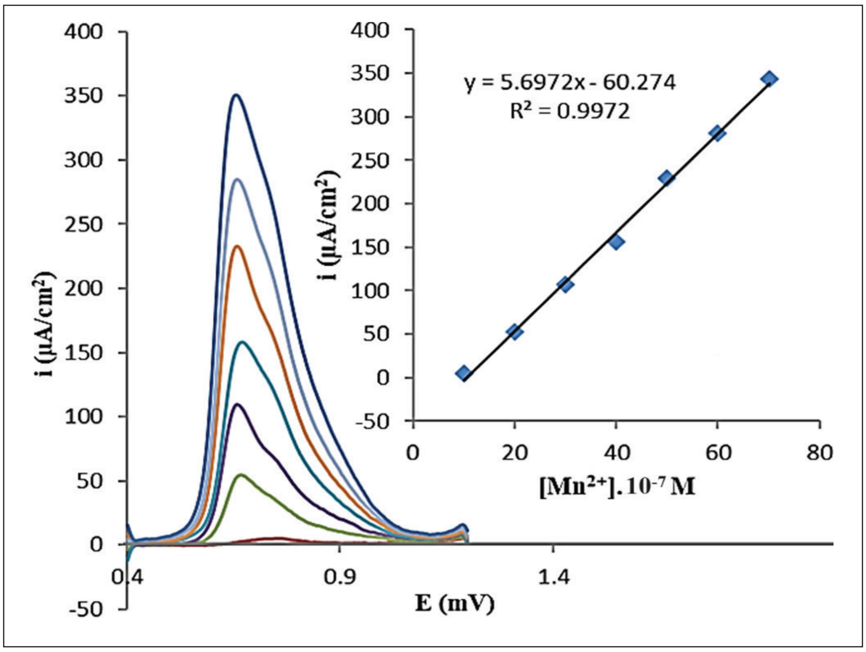

Fig. 9. Curves obtained by DPCSV after successive additions of 10 µL of Mn^{2+} ions 10^{-3} mol.L^{-1} to the supporting electrolyte solution (acetate buffer 0.1 mol L^{-1} pH 4.5) containing Mn^{2+} ions 10^{-6} mol.L^{-1}. The inset in the top right-hand corner shows the calibration line in the concentration range 10^{-6}–7×10^{-6} mol L^{-1}. (pre-concentration potential: 1.1 V; pre-concentration time: 2 min; electrode rotation: 1000 rpm)

to determine Mn^{2+} in boreholes and well water in Yamtenga. Figure 10 shows the results of measurements conducted on real samples. This figure shows the spatio-temporal evolution of manganese (II) content in this area's borehole and well water samples.

According to the analysis, manganese levels in the water ranged between 4.36×10^{-3} and 1.738 mg.L^{-1}. Levels of these contaminants vary from one water point to another and vary according to the sampling

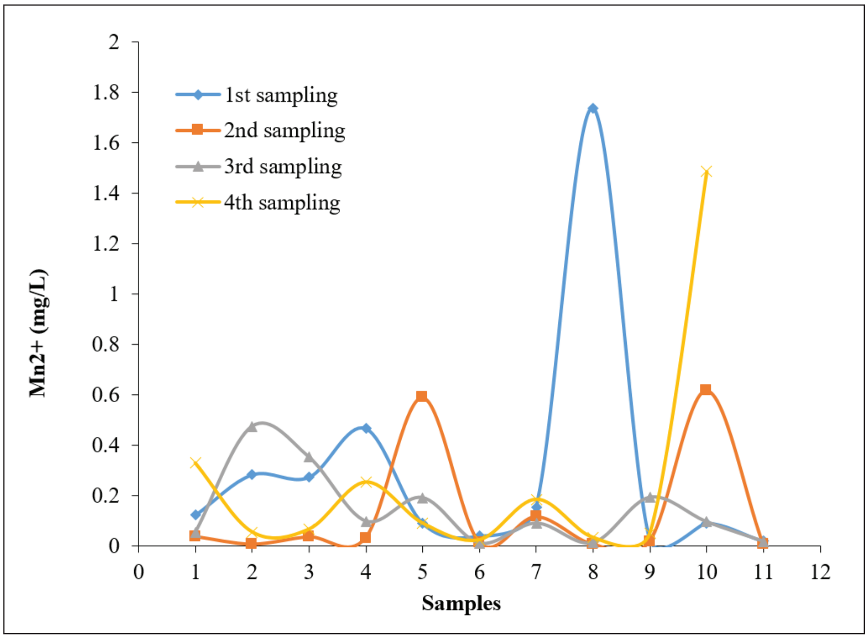

Fig. 10. Spatio-temporal evolution of manganese (II) content in real samples

period. Manganese in water is an organoleptic (metallic taste) and aesthetic nuisance (black color). Consumers can feel the nuisance at concentrations of 0.03 mg L^{-1} (the WHO standard for manganese). Waters with concentrations above the WHO standard are points 2, 4, 5, 8, and 10. As the geological landscape of the Yamtenga area consists of medium-grained gray granite with biotite and rare muscovite, manganese is not a major constituent of the granite type studied in our area, whose dissolution could result in water borehole pollution. A possible explanation for the presence of manganese in groundwater is that the manganese is infiltrated by water from the dam. Since the dam is located near a city, human activity contributes significantly to water pollution in the dam and its tributaries. Consequently, the local population rejects these water sources due to the alteration of their organoleptic characteristics, resulting in complaints about their safety.

3.1.8. Comparison to other methods

To assess the performance of the present method based on the LOD and RSD, it was compared with other methods reported in the literature for Mn (II) determination. The comparison is given in Table 2. Recently, many researchers have worked on determining manganese (II) ions in water, food, and vegetable samples using atomic absorption spectrometry, ultrasound-assisted-dispersive-micro-solid phase extraction, or multi-walled carbon nanotubes [28-31], but the proposed method based on 5-Br-PADAP coupled to DP-CSV and ASV is simple, fast, low cost and accurate/precise results as compared to others.

As a cheap instrument and a simple procedure, our electrochemical method performs relatively well at a low cost and detection limit. As a result, this sensor could be considered a good choice for Mn (II) determination.

3.2. Manganese removal by aeration-filtration

3.2.1. Granulometric analysis

The complete granulometric analysis curves for S_1, S_2, and S_3 are shown in Figure 11.

Table 2. Comparison of experimental results with reported data for Mn (II) determination

Method/ Technique	**LOD**	**RSD**	**Reference**
Rotating carbon paste disk electrode/DP-CSV	4×10^{-9} mol. L^{-1}	3%	[11]
Boron-doped diamond/DP-CSV	7.4×10^{-7} mol. L^{-1}	/	[23]
Bentonite–porphyrin CPE/ASV	1.07×10^{-7} mol. L^{-1}	2.30%	[24]
1-(2-pyridyl azo)− 2-naphthol – CPE/ DP-CSV	6.9×10^{-9} mol. L^{-1}	2.90 to 7.20 %	[25]
Ion-Selective Membrane Electrode/ Potentiometry	8.0×10^{-6} mol. L^{-1}	/	[26]
Silver Nanoparticles/ Colorimetry	0.06 µmol. L^{-1}	/	[27]
Immobilization on chloro-functionalized multi-walled carbon nanotubes	0.12 µg L^{-1}	/	[28]
Ultrasound assisted-dispersive-micro-solid phase extraction	0.007 µg L^{-1}	% 2.3	[29]
Flame atomic absorption spectrometry (FAAS)	0.75 µg L^{-1}	Lower than 7%	[30]
Cloud point extraction and graphite furnace atomic absorption spectrometry	0.020 (ng mL^{-1})	3.5%	[31]
CPE-5-Br-PADAP/DP-CSV	3×10^{-7} mol.L^{-1}	3.36%	This work

DP-CSV: differential pulse cathodic stripping voltammetry
ASV: Anodic Stripping Voltammetry.

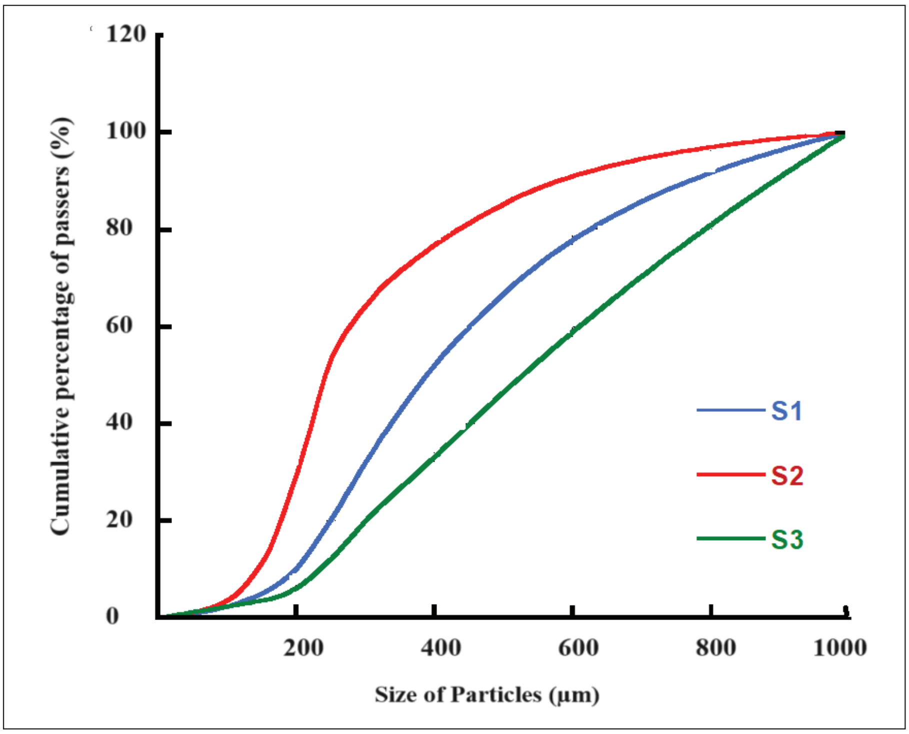

Fig. 11. S_1, S_2 and S_3 granulometric distribution

Table 3. Granulometric parameters and uniformity coefficients for S_1, S_2 and S_3 samples

Parameters	d_{10} (μm)	d_{50} (μm)	d_{60} (μm)	d_{90} (μm)	CU
S_1	200	390	440	840	2.2
S_2	150	240	275	650	1.8
S_3	230	530	625	910	2.7

The main granulometric parameters and the coefficient of uniformity (CU) of the three sand samples were determined based on the granulometric analysis curves. These data are presented in Table 3. Among the three sand samples, S_1 and S_3 have CU values that exceed the range recommended for sand filtration. The S_2 sample falls within the recommended range with a CU value of 1.8. This sand is more homogeneous and more suitable for filtration [2]. So, it will be used for our filtration tests.

The complete granulometric analysis curve for GOM is shown in Figure 12. We extract the gravel sample's main granulometric parameters and its uniformity coefficient from this granulometric curve. The GOM's main granulometric parameters and coefficient of uniformity are shown in Table 4.

3.2.2.Manganese (II) removal tests

The results of manganese (II) removal tests as a function of aeration time and pH are shown in Figure 13. For filtration, the sand used is suitable S_2, and the gravel was GOM.

Manganese removal corresponds to Mn (II) oxidation by atmospheric oxygen. This oxidation is followed by its respective precipitation on the filter as manganese oxide MnO_2. The manganese oxidation reaction is written [32-34].

$$2Mn^{2+} + O_2 + 2H_2O \rightarrow 2MnO_2\downarrow + 4H^+$$
(Eq. 5)

The aeration-filtration process allows a removal rate of manganese, after 2 hours of aeration, of 74.8% at pH 6, 79.3% at pH 7, and 84.5% at pH 8. It should be noted that at pH 8 and for one hour of

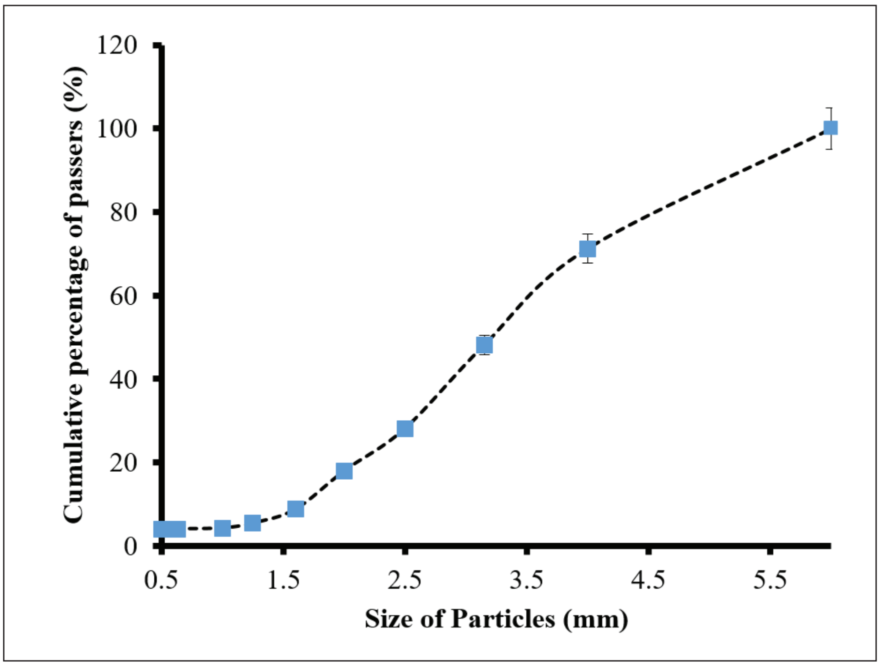

Fig. 12. GOM granulometric distribution

Table 4. The GOM's main granulometric parameters and coefficient of uniformity

Parameters	d_{10} (mm)	d_{50} (mm)	d_{60} (mm)	d_{90} (mm)	CU
GOM	1.65	3.2	3.5	5.25	2.1

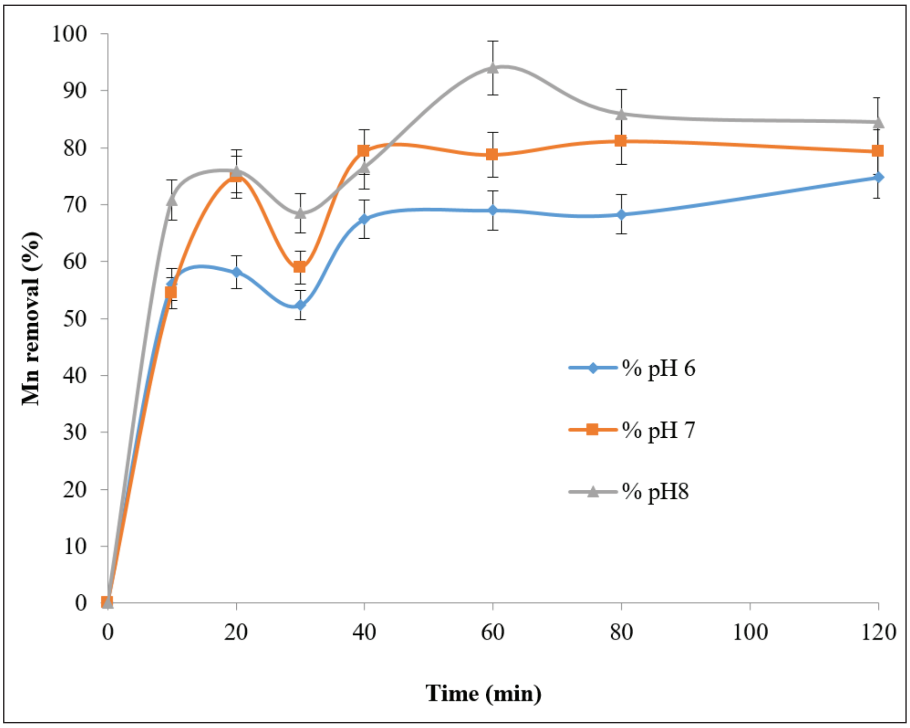

Fig. 13. Evolution of manganese removal rate during aeration-filtration at different pH values

aeration, we obtained a removal rate of 95%. This value decreased and stabilized at 84.5% after 2 hours of aeration. The removal of manganese is highly dependent on the pH of the water [35]. Also, manganese removal increases with pH. Several studies have concluded that manganese cannot be removed with simple aeration using atmospheric oxygen [17]. As a result of successive filtrations on the same sand filter, manganese can precipitate or adsorb onto the manganese oxide formed [2], which justifies the high removal rates. In this study, manganese removal rates are similar to those in the literature. Also, Lanciné et al. used aeration followed by sand filtration to remove iron and manganese from borehole water in rural areas. In this process, 71% of manganese was removed after 1 hour of air aeration [2]. Cheng et al. used aeration, a manganese sand filter, and ultrafiltration for manganese removal from water. By using this process, manganese can be removed from water by 90% [36]. Jeż-Walkowiak and colleagues researched the filtration process on the pilot scale using three different filtration materials. In all of the research cycles, they demonstrated high efficiency in manganese removal and the highest stability of effects with the auto-activated bed (100%); Gabon manganese ore was characterized by high efficiency (90%) in removing manganese from filtrated water; silica sand was represented in the beginning by the lowest Mn removal efficiency (20%) but was observed to increase with time [37]. El-Naggar obtained similar results when he investigated the removal of Mn through the filtration of different types of sand at different depths and during filtration. According to this author, the best results were obtained at a filter material depth of 90 cm, producing a manganese removal rate of 100% [38]. Using aeration and coagulation-flocculation, Ntakiyiruta et al. demonstrated the possibility of removing manganese ions with an efficiency of over 90.34 percent [17]. The removal rates obtained by this method are also comparable to those obtained by biological treatment. Casalini et al. proposed a biological manganese removal process that achieved a 95% removal rate at the filter outlet [39]. The researchers showed that manganese (II) can also be removed from water by nanotechnology processes [40]. El Shahawy et al. removed Mn (II) ions from wastewater using an AgNPs/GO/chitosan nanocomposite material. Their study achieved a high removal rate of 97.9% [40].

4. Conclusion

As part of the present work, we have developed an electrochemical sensor for determining manganese (II) in the presence of the ligand 2-(5'-Bromo-2'-pyridylazo)-5-diethylaminophenol (5-Br-PADAP) on a carbon paste electrode. By optimizing the analytical parameters with cathodic stripping voltammetry (CSV), the sensor has determined the manganese content of water samples taken from wells and boreholes. The manganese content of the water analyzed ranged from 4.36×10^{-3} to 1.738 $mg.L^{-1}$. Therefore, treating water with manganese levels exceeding the WHO standard is necessary. An investigation was conducted in the laboratory to develop a low-cost process for removing manganese from boreholes and well waters, particularly by aeration and filtration. Based on air-oxygen oxidation and then filtration on sand and gravel, the process can be used in rural, suburban, and family environments without strong oxidants, which are generally toxic chemicals. The manganese removal efficiencies achieved in this study (74.8% to 84.5% for two h of aeration, 97% at pH 8, and for one h of aeration) demonstrate the interest in using this process in rural areas, particularly in developing countries with low incomes.

5. Acknowledgment

The authors thanks to the Department of Chemistry, Faculty of Science and Technology, Abdou Moumouni University, Niamey, Niger. The financial support of the International Science Programme [ISP], Uppsala, Sweden is gratefully acknowledged.

6. References

[1] J. Rodier, B. Legube, N. Merlet, B. Regis, Natural waters, wastewater, seawater: Water analysis (L'analyse de l'eau), Dunod, 10th edition, 2016. https://www.dunod.com/sciences-techniques/analyse-eau-eaux-naturelles-eaux-residuaires-eau-mer-0

[2] G.D. Lanciné, A.J. Touchard, K. Bamory, K. Fernand, K. Kouadio, S. Issiaka, Removal of iron and manganese by aeration-filtration of borehole water in rural areas in developing countries, the case of the Tassialé region (southern Côte d'Ivoire), Eur. J. Sci. Res., 19 (2008) 558-567. http://www.eurojournals.com/ejsr.htm

[3] A.A. Mahamane, G. Boubié, Physico-chemical characterizations of groundwater in the locality of Yamtenga (Burkina Faso), Int. J. Biol. Chem. Sci., 9 (2015) 517-533. https://doi.org/10.4314/ijbcs.v9i1.44

[4] R. Mogwasi, M. Eric, N. Obed, Inductively coupled plasma-mass spectrometry versus flame atomic absorption spectrophotometry for the analysis of Fe, Cu, Zn, Mn, and Cr in medicinal plants: a comparison study, Adv. Transl. Med., 2 (2023) 1-15. https://doi.org/10.55976/atm.220231321-15

[5] R.D. Crapnell, E.B. Craig, Electroanalytical overview: The determination of manganese, Sens. Actuators Rep., 4 (2022) 100110. https://doi.org/10.1016/j.snr.2022.100110

[6] S. Sima, S. Cinti, Anodic and cathodic stripping voltammetry for metals sensing, Electrochem., 17 (2023) 55-72. https://doi.org/10.1039/BK9781839169366-00055

[7] Y. Yang, Y. Huang, H. Luo, J. Zao, J. Bi, G. Wu, Ion interference and elimination in electrochemical detection of heavy metals using anodic stripping voltammetry, J. Electrochem. Soc., 170 (2023) 057507. https://doi.org/10.1149/1945-7111/acd1ba

[8] I. Dominguez, M.C. Jesus, D.V. Ignacio, D.M. Juan, S. Radka, S. Petr, S. Vitezslav, Ś. Mateusz, R. M. Ignacio, Electrochemical lossy mode resonance for detection of manganese ions, Sens. Actuators B Chem., 394 (2023) 134446. https://doi.org/10.1016/j.snb.2023.134446

[9] G. Ringgit, S. Shafiquzzaman, S. Surayani L. Mohammad, Synthesized f-MWCNTs/CS/PB for determination of manganese (Mn^{2+}) in drinking water, Monatsh. Chem., 154 (2023) 191-203. https://doi.org/10.1007/s00706-022-03026-3

[10] E. Boselli, Z. Wu, A. Friedman, C.B. Henn, L. Papautsky, Validation of electrochemical sensor for determination of manganese in drinking water, Environ. Sci. Technol., 55 (2021) 7501-7509. https://doi.org/10.1021/acs.est.0c05929

[11] C. Mariame, Y.N. Alfred, B. Drissa, G.M. El Amine, Y.M. Issa, E.R. Mama, Assessment of dissolved manganese (II) pollution in river water by differential pulse cathodic stripping voltammetry: A case study of River Boubo, Côte d'Ivoire, Afr. J. Pure Appl. Chem., 7 (2013) 318-324. https://doi.org/10.5897/AJPAC2013.0516

[12] H.S. El-Desoky, M.I. Iqbal, M.G. Mohamed, Stripping voltammetry method for determination of manganese as complex with oxine at the carbon paste electrode with and without modification with montmorillonite clay, J. Solid State Electrochem., 17 (2013) 3153-3167. https://doi.org/10.1007/s10008-013-2204-2

[13] E. M Ghoneim, Simultaneous determination of Mn (II), Cu (II) and Fe (III) as 2-(5′-bromo-2′-pyridylazo)-5-diethylaminophenol complexes by adsorptive cathodic stripping voltammetry at a carbon paste electrode, Talanta, 82 (2010) 646-652. https://doi.org/10.1016/j.talanta.2010.05.025

[14] A.A. Mahamane, C. Despas, R. Adamou, A. Walcarius, Carbon paste electrode modified with 5-Br-PADAP as a new electrochemical sensor for the detection of inorganic mercury (II), J. Mater. Environ. Sci., 13 (2022) 54-69. http://www.jmaterenvironsci.com

[15] T. Chu, M. Cheng, S. Hou, Y. Yang, Modified graphite paper treated by anionic intercalation

for manganese removal via electrochemical deposition in water treatment, J. Ind. Eng. Chem., 120 (2023) 504-513.https://doi.org/10.1016/j.jiec.2023.01.002

[16] S.M. Safwat, N.Y. Mohamed, M.M. El-Seddik, Performance evaluation and life cycle assessment of electrocoagulation process for manganese removal from wastewater using titanium electrodes. J. Environ. Manage., 328 (2023)116967. https://doi.org/10.1016/j.jenvman.2022.116967

[17] P.Ntakiyiruta,P.C.Mpawenayo,D.Rucakumugufi, P. Bigumandondera, T. Ndikumana, J.L. Vasel, Removal of iron and manganese by aeration and coagulation-flocculation in borehole water from the town of Rumonge (Burundi), J. Mater. Environ. Sci., 14 (2023) 141-152. http://www.jmaterenvironsci.com

[18] K.L. Dishman, Sieving in particle size analysis, Encyclopedia of Analytical Chemistry application, theory, and instrumentation, Wiley publisher, 2006. https://doi.org/10.1002/9780470027318.a1514

[19] P. Charles, Catalytic removal of iron and manganese for the production of drinking water, water technologies drinking water supply, Suez Environnement, 2006. https://www.eurochlore.fr/wp-content/uploads/2016/12/Rapport_06AEP07.pdf

[20] M. Gharous, L. Bounab, F.J. Pereira, M. Choukairi, R. López, A.J. Aller, Electrochemical kinetics and detection of paracetamol by stevensite-modified carbon paste electrode in biological fluids and pharmaceutical formulations, Int. J. Mol. Sci., 24 (2023) 11269. https://doi.org/10.3390/ijms241411269

[21] A.A. Mahamane, B. Guel, P.L. Fabre, Electrochemical behavior of iron (II) at a nafion-1, 10-phenanthroline-modified carbon paste electrode: Assessing the correlation between Preconcentration potential, surface morphology, and impedance measurements, Challenge Adv. Chem. Sci., 2 (2021) 52–71.https://doi.org/10.9734/bpi/cacs/v2/2419F

[22] S. A Leau, C. Lete, C. Matei, S. Lupu, Electrochemical sensing platform based on metal nanoparticles for epinephrine and serotonin, Biosens., 13 (2023) 781. https://doi.org/10.3390/bios13080781

[23] C.M. Welch, C.E. Banks, Š. Komorsky-Lovrić, R.G. Compton, Electroanalysis of trace manganese via cathodic stripping voltammetry: exploration of edge plane pyrolytic graphite electrodes for environmental analysis, Croat. Chem. Acta, 79 (2006) 27–32. https://core.ac.uk/download/pdf/14377079.pdf

[24] B. Rezaei, M. Ghiaci, M.E. Sedaghat, A selective modified bentonite–porphyrin carbon paste electrode for determination of Mn(II) by using anodic stripping voltammetry, Sens. Actuators B, 131 (2008) 439–447. https://doi.org/10.1016/j.snb.2007.12.017

[25] S. B. Khoo, M. K. Soh, Q. Cai, M. R. Khan, S. X. Guo, Differential pulse cathodic stripping voltammetric determination of manganese (II) and manganese (VII) at the 1-(2-pyridylazo)-2-naphthol-modified carbon paste electrode, Electroanalysis, 9 (1997) 45–51. https://doi.org/10.1002/elan.1140090111

[26] M. Aghaie, M. Giahi, M. Zawari, Manganese(II) ion-selective membrane electrode based on N-(2-picolinamido ethyl)-picolinamide as neutral carrier, Bull. Korean Chem. Soc., 31 (2010) 2980–2984. https://doi.org/10.5012/bkcs.2010.31.10.2980

[27] S. Sharma, A. Jaiswal, K.N. Uttam, Synthesis of sensitive and robust lignin capped silver nanoparticles for the determination of cobalt(II), chromium(III), and manganese(II) ions by colorimetry and manganese(II) ions by surface-enhanced raman scattering (SERS) in aqueous media, Anal. Lett., 54 (2021) 2051-2069. https://doi.org/10.1080/00032719.2020.1837855

[28] J. Rakhtshah, M. Dehghani Mobarake, Simultaneously speciation and determination

of manganese (II) and (VII) ions in water, food, and vegetable samples based on immobilization of N-acetylcysteine on multi-walled carbon nanotubes, Food Chem., 389 (2022) 133124. https://doi.org/10.1016/j.foodchem.2022.133124

[29] A.Khaligh,H.Z.Mousavi,A.Rashidi, Ultrasound assisted-dispersive-micro-solid phase extraction based on bulky amino bimodal mesoporous silica nanoparticles for speciation of trace manganese (II)/(VII) ions in water samples, Microchem. J., 124 (2016) 637–645. https://doi.org/10.1016/j.microc.2015.10.008

[30] D. Citak, M. Tuzen, M. Soylak, Speciation of Mn(II), Mn(VII) and total manganese in water and food samples by coprecipitation–atomic absorption spectrometry combination, J. Hazard. Mater., 173 (2010) 773–777.https://doi.org/10.1016/j.jhazmat.2009.09.004

[31] S. Golkhah, H. Zavvar Mousavi, Removal of Pb (II) and Cu (II) Ions from aqueous solutions by cadmium sulfide Nanoparticles, Int. J. Nanosci. Nanotechnol., 13 (2017) 105-117. https://www.ijnnonline.net/article_25609.html

[32] S. Kouzbour, N. El Azher, B. Gourich, F. Gros, C. Vial, Y. Stiriba, Removal of manganese (II) from drinking water by aeration process using an airlift reactor, J. Water Process. Eng., 16 (2017) 233–239.https://doi.org/10.1016/j.jwpe.2017.01.010

[33] L. Schamphelaire, R. Korneel, N. Boon, W. Verstraete, P. Boekx, Minireview: The potential of enhanced manganese redox cycling for sediment oxidation, Geomicrobiol. J., 24 (2007) 547-558.https://doi.org/10.1080/01490450701670137

[34] S. Jerroumi, M. Amarine, B. Gourich, Technological trends in manganese removal from groundwater: A review, J. Water Process. Eng., 56 (2023) 104365. https://doi.org/10.1016/j.jwpe.2023.104365

[35] K. Fialova, M. Motlochova, L. Cermakova, K. Novotna, J. Bacova, T. Rousar, M. Pivokonsky, Removal of manganese by adsorption onto newly synthesized TiO2-based adsorbent during drinking water treatment, Environ. Tech., 44 (2023) 1322-1333. https://doi.org/10.1080/09593330.2021.2000042

[36] L.H. Cheng, Z.Z. Xiong, S. Cai, D.W. Li, X.H. Xu, Aeration-manganese sand filter-ultrafiltration to remove iron and manganese from water: Oxidation effect and fouling behavior of manganese sand coated film, J. Water Process. Eng., 38 (2020) 10162. https://doi.org/10.1016/j.jwpe.2020.101621

[37] J.J. Walkowiak, Z. Dymaczewski, A.S. Janiaczyk, A.B. Nowicka, M. Szybowicz, Efficiency of Mn removal of different filtration materials for groundwater treatment linking chemical and physical properties, Water, 9 (2017) 498. https://doi.org/10.3390/w9070498

[38] H.M. El-Naggar, Development of low-cost technology for the removal of iron and manganese from groundwater in Siwa Oasis, J. Egypt. Public Health Assoc., 85 (2010). 169-188. https://pubmed.ncbi.nlm.nih.gov/21244816/

[39] L.C. Casalini, A. Piazza, F. Masotti, V. A. Pacini, G. Sanguinetti, J. Ottado, N. Gottig, Manganese removal efficiencies and bacterial community profiles in non-bioaugmented and in bioaugmented sand filters exposed to different temperatures, J. Water Process. Eng., 36 (2020) 101261 .https://doi.org/10.1016/j.jwpe.2020.101261

[40] A. El Shahawy, M.F. Mubarak, M. El Shafie, H.M. Abdulla, Adsorption of Mn (II) ions from wastewater using an AgNPs/GO/chitosan nanocomposite material, RSC Adv., 12 (2022) 29385-29398. https://doi.org/10.1039/D2RA04693H

Anal. Methods Environ. Chem. J. 6 (4) (2023) 93-106

Research Article, Issue 4
Analytical Methods in Environmental Chemistry Journal
Journal home page: www.amecj.com/ir

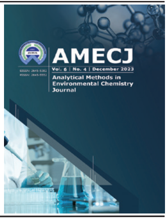

Removal of ethylene bisdithiocarbamate fungicides in wastewater and agricultural runoff by zinc oxide nanoparticles before analysis by HPLC and UV-Vis spectroscopy

Mahadi Danjuma Sani [a, c,*], V.D.N. Kumar Abbaraju [a], N.V.S. Venugopal [b], and Nura Umar Kura[c]
[a] *Department of Environmental Science, GITAM School of Science, GITAM (Deemed to be University), Visakhapatnam, A.P. India*
[b] *Department of Chemistry, GITAM School of Science, GITAM (Deemed to be University), Visakhapatnam, A.P. India*
[c] *Department of Environmental Science, Federal University Dutse, Jigawa State, Nigeria*

ARTICLE INFO:
Received 26 Jul 2023
Revised form 10 Oct 2023
Accepted 19 Nov 2023
Available online 30 Dec 2023

Keywords:
Removal,
Photocatalytic degradation,
Zinc oxide,
Ethylene bisdithiocarbamate,
High-performance liquid chromatography,
UV-Vis spectroscopy

ABSTRACT

This study developed an applied method based on the degradation to remove ethylene bisdithiocarbamate (EBDC) fungicides from wastewater and agricultural runoff by zinc oxide nanoparticles (ZnONPs). The synthesized ZnONPs were characterized using XRD for material crystallinity, scanning electron microscope (SEM) and particle size analysis (PSA) for surface structure, morphology and particle size (nm), respectively. The energy-dispersive X-ray spectroscopy (EDX) spectra confirmed the presence of zinc and showed that the synthesized zinc oxide nanoparticles were pure. Determination of the adsorption and photocatalytic degradation of Mancozeb (MCZ) fungicides based on ZnONPs was performed. Different amounts of ZnONPs were loaded into an MCZ fungicide solution in different concentrations. High-performance liquid chromatography (HPLC) and UV-Vis spectroscopy were used to determine the dithiocarbamate residue and the degradation efficiency of the synthesized particles. The particle size distribution of the synthesized ZnONPs was found to be in the range of 50-95 nm. At optimum conditions, with a ZnONPs dosage of 10 mg, (MCZ) fungicide concentration of 9.37 mg L^{-1}, and a duration of 60 minutes, the degradation efficiency was surpassed at more than 95%. Additionally, the nanoparticles demonstrated excellent reusability and maintained efficient activity for up to three cycles. It is crucial and significant to keep on exploring the intrinsic capabilities of abundant metal oxides like zinc oxide nanoparticles for environmental remediation and other applications.

1. Introduction

Ensuring equilibrium in our ecosystem is vital for the well-being of living and nonliving components. Using chemical pesticides plays a critical role in sustaining food production to meet the needs of a growing global population. However, it simultaneously poses risks to essential living organisms, including humans, and environmental frameworks. The residues of these pesticides were found in water [1], soil [2], food, and living systems [3, 4]. Pesticides are mainly used to destroy pests, living organisms with the same physiology and anatomy as other essential organisms like bees. These pesticides target body systems like the nervous

---

*Corresponding Author: Mahadi Danjuma Sani
Email: msani@gitam.in
https://doi.org/10.24200/amecj.v6.i04.251

system and other crucial systems in organisms, thereby disrupting and inhibiting the normal functioning of the physiology [5, 6]. The extensive and careless application of chemical pesticides on farms and agricultural products with little to zero knowledge of their proper application methods by most farmers brought about the unexpected. As a result, several synthetic chemical pesticides throughout history have found their way into water bodies through runoff, wind action, and many other processes. Studies have shown that most pesticides are persistent and can accumulate in a living system [7]. Dithiocarbamate pesticides like mancozeb (MCZ) are regarded as significant fungicides with applications worldwide by farmers from various countries [8]. Despite the wide application and acceptance of (MCZ) fungicides, it was found to be lethal and detrimental to off-target essential organism and human beings. Mancozeb was found to impart neurotoxicity, damaging mitochondria, and myofibril splitting [9], thyroid disruption [10], changes in glutathione and alterations in essential metal homeostasis [11], adverse effects on steroid production [12], ovarian injury and apoptosis [13], induce alteration in the development of hypothalamic systems that are essential for maturation of neuroendocrine system [14], disrupt mitochondria and bioenergetic activities in the body [15], affect male fertility [16] and induce behavioural deficit [17]. Although (MCZ) is widely accepted and used by farmers in many countries, these and many other reports have proven that the uncontrolled and excessive application of (MCZ) fungicide is a case for alarm. Therefore, there is an urgent and crucial need to devise a means through which the residues of these toxic pesticides can be reduced or degraded in the environment. Researchers employed several techniques to degrade pesticides in agricultural runoff or water in general, including conventional methods. However, the effectiveness, efficiency, and eco-friendliness of some of these techniques became another case of concern. Nanotechnology has brought a whole new view to the world of science, where tiny and unique products with a wide variety of essential properties are used in several sectors, including pharmaceuticals, medicine, agriculture, and environmental remediation. Gebre and Sendeku 2019 define nanotechnology as an interdisciplinary field of research involving nanoparticle synthesis, characterization, and application [18]. The evolving and modern technology consists of manipulating particles to form nanosized materials with various properties different from the parent material or raw materials with features like large surface area, light absorption, and suitable band gap energy that are essential today. The applications of nanoparticles in environmental remediation and cleanup cannot be overemphasized. Nanoparticles are effective photocatalytic agents [19, 20], possess great antimicrobial activity [21], act as biosensors [22], are active in the degradation of pesticides and other organic pollutants [23,24] and sound in the removal of heavy metals [25,26]if the amounts of heavy metals are more than the acceptable amounts (mentioned by WHO. Metal and metal oxide nanoparticles are important in wastewater remediation [27]. Furthermore, functionalized graphene oxide with bismuth and titanium oxide nanoparticles was revealed to effectively remove formaldehyde from the air by photocatalysis [28]. Moreover, xylene vapour was also neutralized in the air following photocatalysis in the presence of UV using bismuth oxide coupled graphene oxide nanomaterial [29]. Studies have shown that these nanoparticles have a special feature that helps in the adsorption, degradation, and removal of pesticides and other contaminants from wastewater [30,31]. Among the metal oxides or magnetic nanoparticles, zinc oxide ZnO was found to possess a large variety of essential properties that are significant in the field of wastewater remediation in addition to its abundance. Studies have reported the application of zinc oxide (NPs) in the degradation and photocatalytic degradation of pollutants and contaminants in the environment like quinclorac [32], polyethylene terephthalate [33], alizarin red dye [34], rhodamine B [35], hospital waste [31], amlodipine besylate [36], methylene blue and eosin yellow dye [37] and methylene blue and methyl orange [30]. Several studies have reported the photocatalytic activity of ZnO (NPs), which was found to be an effective property in wastewater remediation. Moreover, ZnO (NPs) effectively and efficiently degrade toxic and volatile organic vapours (BTEX). Nagaraju et al. studied the efficiency of ZnO in the sensitivity of (BTEX). The investigation focused on the sensitivity and selectivity of toxic volatile organic vapours like benzene, toluene, ethylbenzene, and xylene (BTEX) under room-temperature conditions [38]. The findings revealed that (NPs) possess efficient activity in detecting BTEX, especially Xylene. Another study by [39] demonstrated an efficient visible light photocatalysis of BTEX in an aqueous solution. It was observed that ZnO nanorods were found to degrade more than 80% of the individual (BTEX) components. Therefore, ZnO (NPs) are also efficient in degrading and converting toxic compounds into harmless particles. Despite numerous studies focusing on the use of zinc oxide nanoparticles ZnO (NPs) for the degradation of contaminants in wastewater, there is a noticeable lack of attention given to their efficacy in degrading pesticides present in agricultural runoff. Only a few articles address pesticide degradation, with no known reports addressing dithiocarbamate (such as mancozeb) fungicides.

Consequently, this study aims to investigate the photocatalytic degradation of residues from the ethylene bis-dithiocarbamate mancozeb pesticide. This particular focus arises from the widespread use of mancozeb in agricultural practices and the presence of its residues in agricultural runoff. Furthermore, the research aims to address the potential environmental and health risks associated with mancozeb, given its known lethal and toxic effects on human health.

2. Materials and Methods

2.1. Instrumental, Materials and Reagents

All reagents and chemicals used for this research were of analytical grade with high purity. Zinc nitrate hexahydrate ($Zn(NO_3)_2.6H_2O$, 98%, CAS No.: 10196-18-6), and sodium hydroxide (NaOH, 98%, CAS No.: 1310-73-2) were purchased from Merck Specialties Private Limited, Mumbai, India. Ethylene bisdithiocarbamate fungicide (Mancozeb fungicide, 75% WP) was purchased from a farmers' market in Vishakapatnam, Andhra Pradesh, India. Millipore Pure water (DI water) was used throughout the work. The Powder X-ray diffraction (PXRD) analysis utilized a Brucker D8 advance facility with a coupled two theta/theta scanning type and mode, employing continuous scanning. Scanning Electron Microscopy-Energy Dispersive X-ray Spectroscopy (SEM-EDAX) was performed using a Jeol 6390 LA/OXFORD XMXN instrument with an accelerating voltage ranging from 0.5 to 30 kV, a magnification of 300,000 times, and a tungsten filament. UV-Vis analysis was conducted using a Shimadzu 1800 instrument, while High-Performance Liquid Chromatography (HPLC) analysis employed an Agilent Technologies 1260 Infinity machine equipped with a UV detector, column oven, electric sample valve, and a Phenomenex Zodiac C18 reversed-phase column (5.0 µm, 150 × 4.60 mm, i.d.).

2.2. Synthesis of ZnO Nanoparticle

Zinc oxide nanoparticle ZnO nanoparticle was prepared or synthesized following a simple and friendly co-precipitation/wet chemical method as modified from the work of [40]we synthesized Hexagonal Zinc oxide (ZnO. Figure 1 shows the stepwise procedure of the synthesis.

Zinc nitrate hexahydrate was employed as a precursor, along with sodium hydroxide and starch serving as precipitating/capping and stabilizing agents. A 0.1 M concentration of zinc nitrate hexahydrate was prepared by dissolving 9.468 g of ($Zn(NO_3)_2.6H_2O$) in 500 ml of double DI water/Millipore water. Additionally, 1% starch solution was prepared and dissolved in the zinc nitrate solution, with continuous stirring until a cloudy solution was formed. Subsequently, drops of 0.2 M concentration of sodium hydroxide were added to the solution under constant stirring, leading to the formation of precipitates. The stirring process continued for 3 hours until a white precipitate of zinc hydroxide ($Zn(OH)_2$) was formed. The solution was left to settle for an hour and then centrifuged at 5000 rpm for 10 minutes. The supernatant liquid was discarded, and the obtained particles were oven-dried at 100°C for

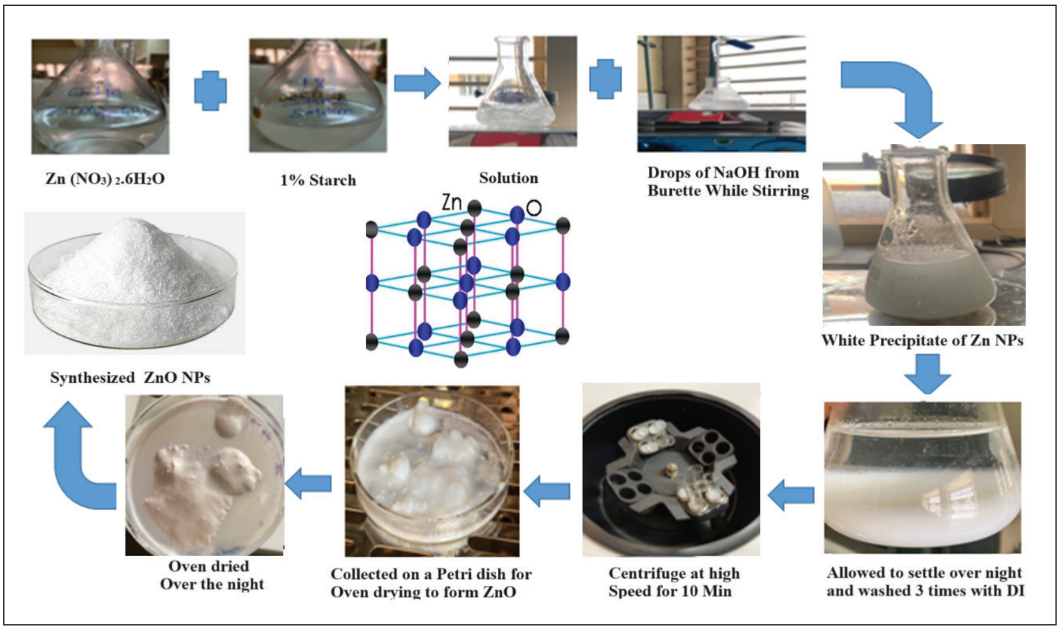

Fig. 1. Synthesis of Zinc oxide Nanoparticles

a few hours to produce the Zn (OH) powder. Later, the powder underwent calcination at 400°C for 3 hours in a muffle furnace to yield ZnO (NPs).

2.3. Characterizations

The synthesized zinc oxide nanoparticles were characterized using X-ray Diffraction (XRD) to determine the crystal structure, crystallite size, and pure phase formation. Scanning Electron Microscopy (SEM) was employed to ascertain the structure and surface morphology of the as-synthesized NPs. Energy Dispersive X-ray Spectroscopy (EDX) was utilized for elemental composition analysis, and particle size analysis was conducted to determine the size of the synthesized nanoparticles.

2.4. Preparation of standard concentrations of Mancozeb Fungicide

The preparation of standard concentrations of the ethylene bis-dithiocarbamate fungicide mancozeb was meticulously carried out in the Environmental Biotechnology Laboratory of GITAM University. Four different concentrations were carefully prepared using Millipore deionized water.

2.5. Adsorption and Photocatalytic Degradation of Mancozeb

This was conducted from 11 pm to 4 pm under natural solar radiation at room temperature to determine the adsorption and photocatalytic activity of ZnO (NPs) on (MCZ) fungicide. Different amounts of (NPs) were loaded into a known concentration of (MCZ) fungicide solution and tagged as; SA, SB,

Table 1. Sample setup containing pesticides and the amounts of loaded nanoparticles

Sample Code	Amount of (NPs)	Initial Concentration before degradation
SA	10 mg	2.0 mg L^{-1}
SB2	5 mg	4.0 mg L^{-1}
SB2	10 mg	4.0 mg L^{-1}
SC1	5 mg	9.4 mg L^{-1}
SC2	10 mg	9.4 mg L^{-1}
SD1	5 mg	15.0 mg L^{-1}
SD2	10 mg	15.0 mg L^{-1}

SC, and SD, respectively (Table 1).

For each batch, the solutions were stirred in the dark for 30 minutes to attain adsorption-desorption equilibrium before exposure to natural solar irradiation at room temperature. After exposure to natural solar irradiation, 10 mL of the solution was sampled every 20 minutes until 120 minutes and then centrifuged at 4000 rpm for 10 minutes to gather the photocatalyst. Each resulting supernatant liquid was collected, labelled, and subjected to UV-visible spectroscopy for absorbance and concentration determination using the Shimadzu 1800 UV spectrophotometer. UV-visible spectroscopy relies on the principles outlined in Beer's Law for quantifying the concentration of a substance in a solution. Beer's Law asserts that the concentration of a substance within a solution is directly proportional to the amount of light absorbed or transmitted through the solution. This technique is frequently employed for gauging the concentration of a substance in a solution, this principle involves measuring the substance's absorbance at a designated wavelength. Also, the UV absorbance of the samples were determined at a wavelength of 190-400 nm. The maximum absorbance ƛmax was obtained at a wavelength of 240 nm. The concentration at time t of each round of the experiment was determined following standard procedure using standard MZC solutions prepared by serial dilution method at ƛmax. The same procedure was applied for the control without (NPs). The effects of time, amount of (NPs), and initial concentration of pesticide were optimized to achieve better results. The final results were exposed to (HPLC) analysis to ascertain the final concentration of the pesticide in the supernatant liquid. HPLC is an important analytical technique/tool for the separation, identification, and quantification of particles in liquid samples. It involves applying high pressure to the mobile phase, allowing for faster and more efficient separations. The same procedure was repeated multiple times after washing the collected/used nanoparticles to study the recoverability and reusability of the (NPs). The degradation efficiency of the zinc oxide nanoparticles was computed using the following formula;

$$\text{Degradation efficiency} = \frac{\text{Co}-\text{Ct}}{\text{Co}} \text{ x } 100$$

Where Co = initial concentration of MCZ in mg L^{-1}
Ct = Concentration at time t (observed concentration in the supernatant) in mg L^{-1}

3. Results and Discussion

3.1. Formation of Zinc oxide Nanoparticle.

Zinc oxide nanoparticle was successfully synthesized through the co-precipitation method using zinc nitrate hexahydrate as a precursor, sodium hydroxide, and starch as precipitating/capping and stabilizing agents. This process follows the possible mechanism of formation of ZnO (NPs) as reported

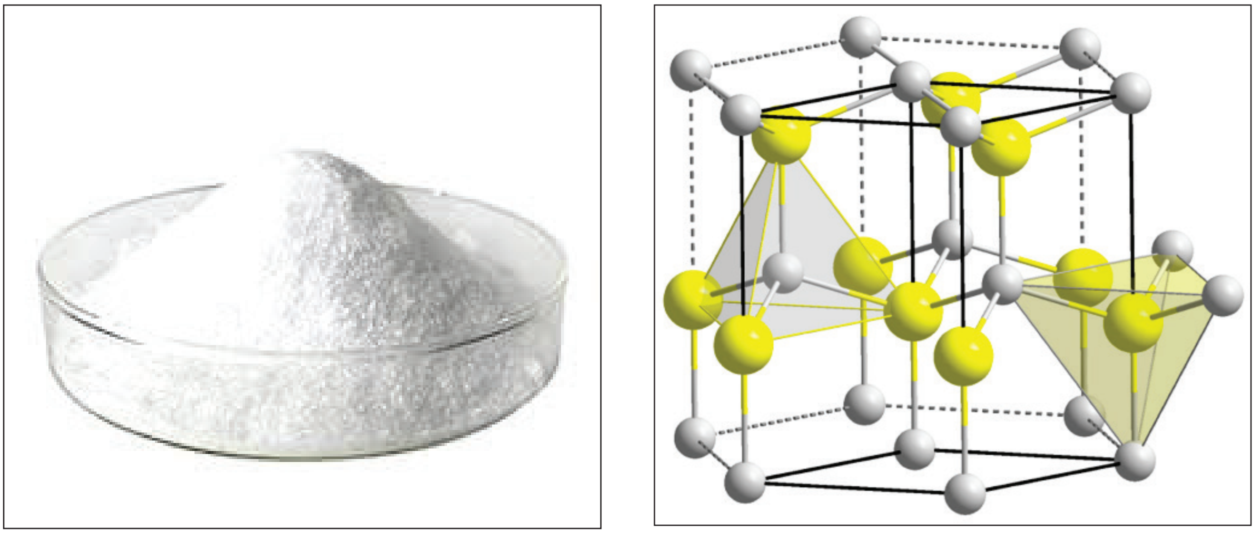

Fig. 2. Zinc oxide Nanoparticle

by [RS 1] which begins with nucleation and growth by diffusion, followed by interparticle growth and ripening. Figure 2 shows the white pow2der zinc oxide nanoparticles synthesized which was later confirmed through characterization by XRD, SEM, and particle analysis.

3.2. Characterization of the Zinc Oxide Nanoparticles

3.2.1.Scanning Electron Microscopy Analysis SEM

The surface morphology and structure of the synthesized zinc oxide nanoparticles were determined using (SEM) analysis. Figure 3 shows the images obtained from (SEM) analysis of the as-synthesized (NPs). It can be observed that the structure and surface morphology of the synthesized (NPs) are presented in different sizes ranging from 1µm to 100 nm. The last image on the bottom right confirms the particle size to be below 100 nm. The sizes of the particles are almost similar as can be observed in Fig. 4 above. The spherical and hexagonal structure of the synthesized particle is in agreement with the findings of [RS2].

3.2.2.Energy Dispersive X-ray Spectroscopy EDX

Energy Dispersive X-ray spectroscopy (EDX) provides the elemental composition of the synthesized nanoparticles with peaks located between 0.5 and 9.0. It can be observed in Figure 4 that the peaks for zinc and oxygen are vividly clear as shown on the spectrum, which can be regarded as the presence of the elements that make up zinc oxide nanoparticles.

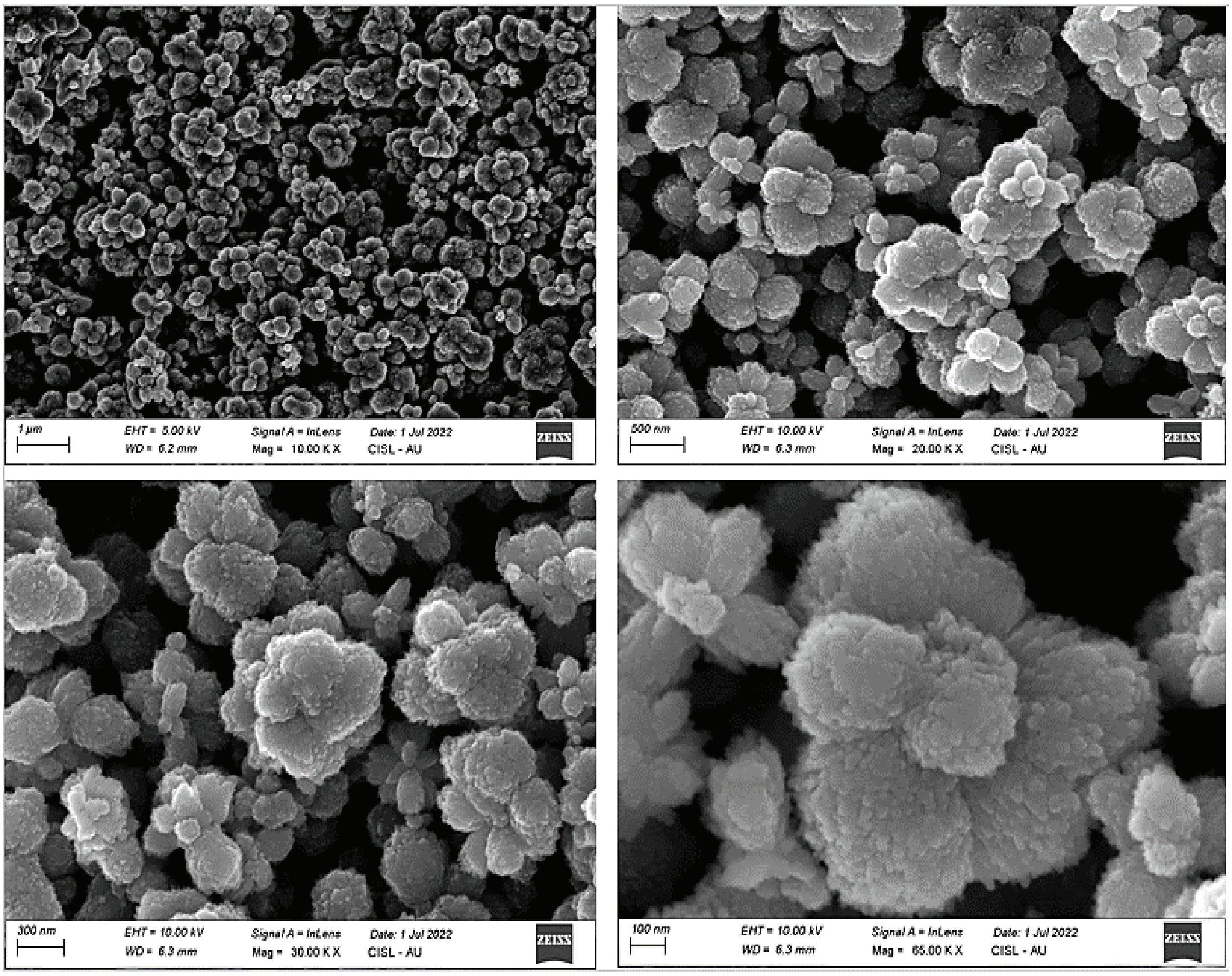

Fig.3. Scanning Electron Microscope Images showing the surface morphology and shape of the synthesized nanoparticles

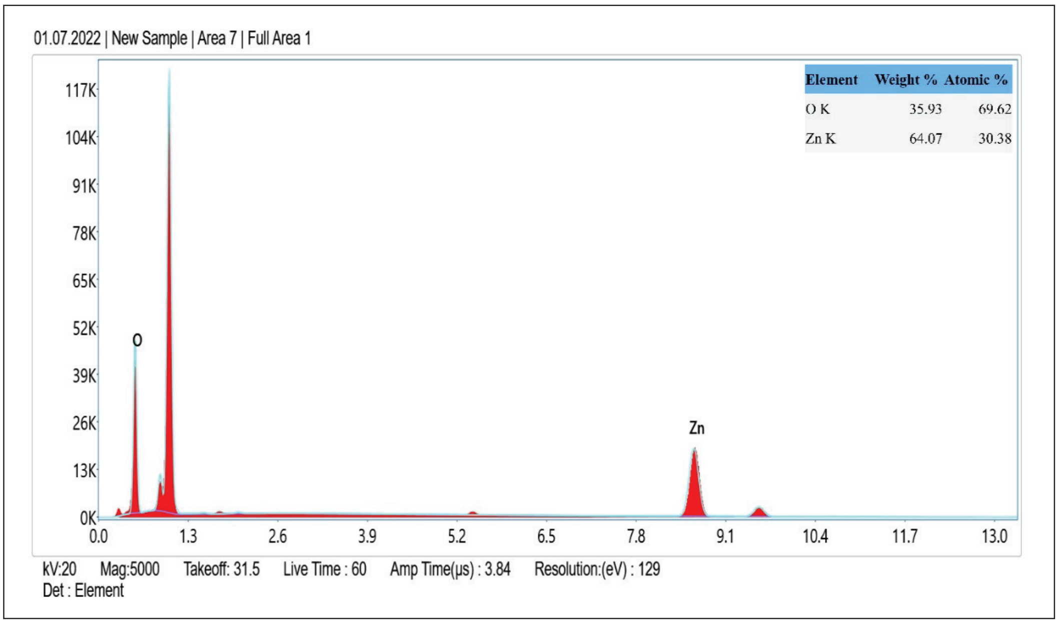

Element	Weight %	Atomic %
O K	35.93	69.62
Zn K	64.07	30.38

Fig. 4. EDX showing the elemental composition of the synthesized nanoparticles

Although other peaks are available in the spectrum which indicates the presence of other particles, zinc and oxygen were found to possess the strongest peaks.

3.2.3.PXRD Analysis

The crystalline structure of the synthesized zinc oxide nanoparticles is provided in Figure 5 below with peaks corresponding to different crystal planes. With special reference to JCPDS card number 89-0510, the diffraction peaks obtained for the synthesized zinc oxide nanoparticles confirm the formation of the hexagonal wurtzite phase of ZnO nanoparticles. The peaks at 31.640°, 34.291°, and 36.083° correspond to (100), (002), and (101) planes of hexagonal crystal patterns of ZnO respectively. The peaks are also in agreement with multiple reported literature [30], [31]. The crystallite size of the particles were at a range of 50-95nm.

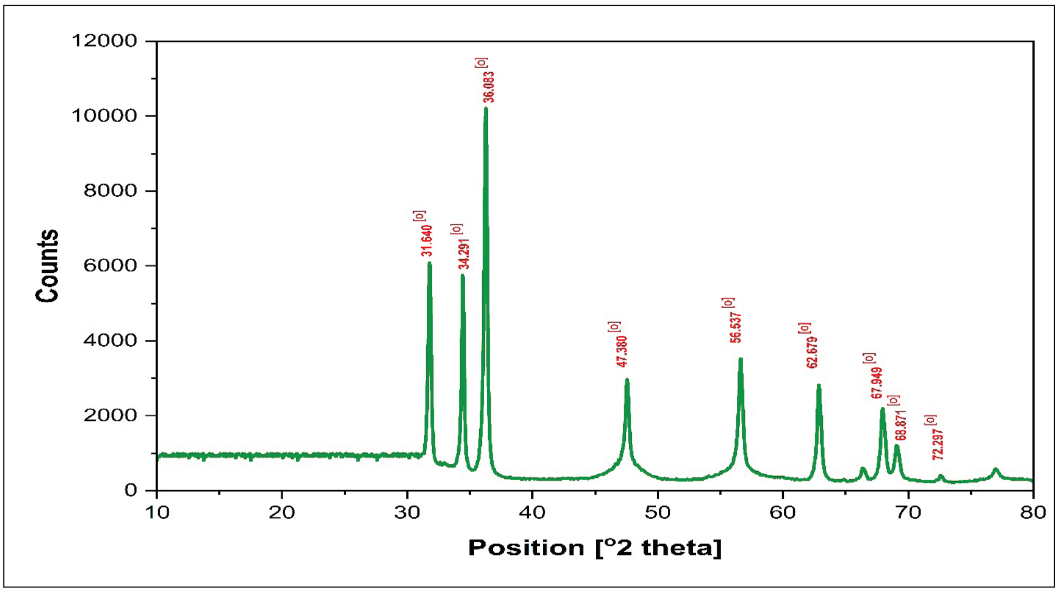

Fig. 5. XRD spectra showing the peaks for the synthesized ZnO NPs

3.3. Photocatalytic activity

Photocatalytic degradation or activity of zinc oxide nanoparticles using ethylene bis-dithiocarbamate fungicides was evaluated. UV-visible spectroscopy and HPLC analysis were used to determine the initial concentration and concentration at time (t). The degradation efficiency of the synthesized particles was determined.

3.3.1. UV-Visible Spectroscopy

Shimadzu UV-1800 spectrophotometer was used in the Environmental Biotechnology Laboratory of the Environmental Science Department, GITAM University. Figure 6 above shows the UV spectrum with absorbance at different time intervals for the sample; SC-2. It can be observed that there is a sharp decrease in the absorbance around the ƛmax between the initial SC-2 concentration and concentration at time t, which is considered a sharp decrease in the concentration of pesticides in the solution. It can be observed that the lowest absorbance was recorded at 60 minutes/1 hour. After optimization for time, initial concentration of pesticide, and the amount of the nanoparticle or photocatalyst, this sample set-up was found to possess the highest activity against the pesticide. The findings revealed in this work agree with multiple findings in literature where pure and doped ZnO (NPs) were reported to significantly decrease the absorbance of multiple pesticides including; quinclorac herbicide [32], imidacloprid pesticide [RS3]we developed a Z-scheme photocatalyst system consisting of PANI/ZnO-CoMoO4 for degradation photocatalytic processes. The structural composition and morphologies of the PANI/ZnO-CoMoO4 nanocomposite were analyzed by FTIR, FESEM-EDS, and XRD techniques. Subsequently, the pesticide-degradation experiments were performed for the degradation of imidacloprid (IM, and lambda-cyhalothrin pesticide [RS4].

3.3.2. HPLC Analysis

High-Performance Liquid Chromatography, also known as High-Pressure Liquid Chromatography, was used for the final quantification of the pesticide concentration. The experiment was conducted at Biofact Research PVT. Limited at Visakhapatnam, Andhra Pradesh. The instrument name is HPLC Agilent 1260 infinity with an instrument code of BFR/EQ/0487. Agilent HPLC (1260 Infinity II) equipped with UV detector, column oven, electric sample valve, Phenomenex Zodiac C18 reversed-phase column (5.0 µm, 150 × 4.60 mm, i.d).

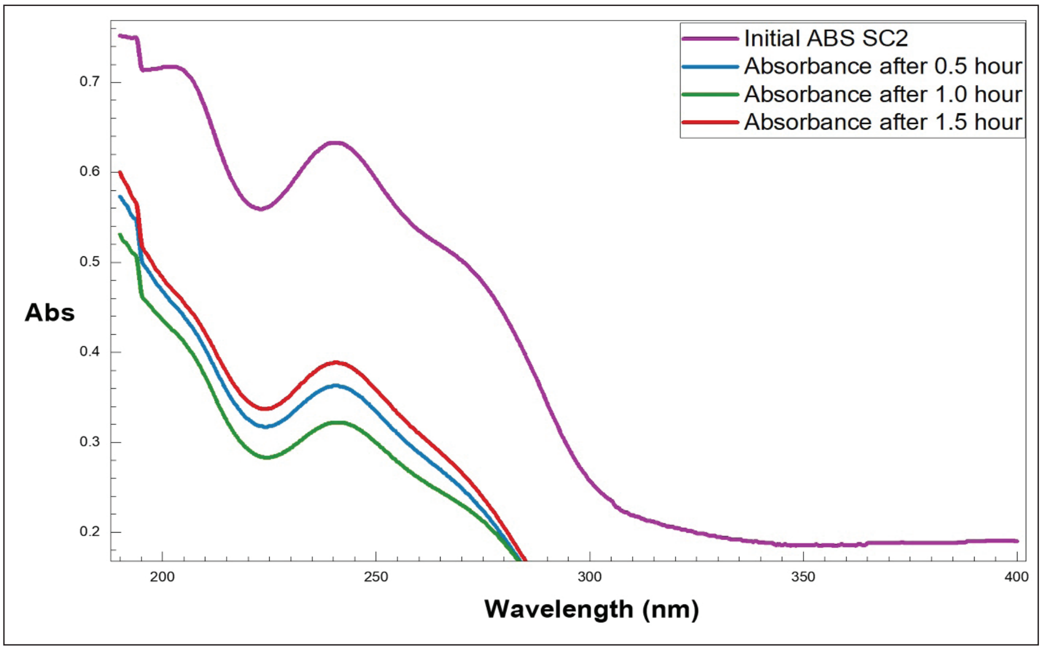

Fig. 6. UV absorbance in the batch photocatalytic experiment of SC2

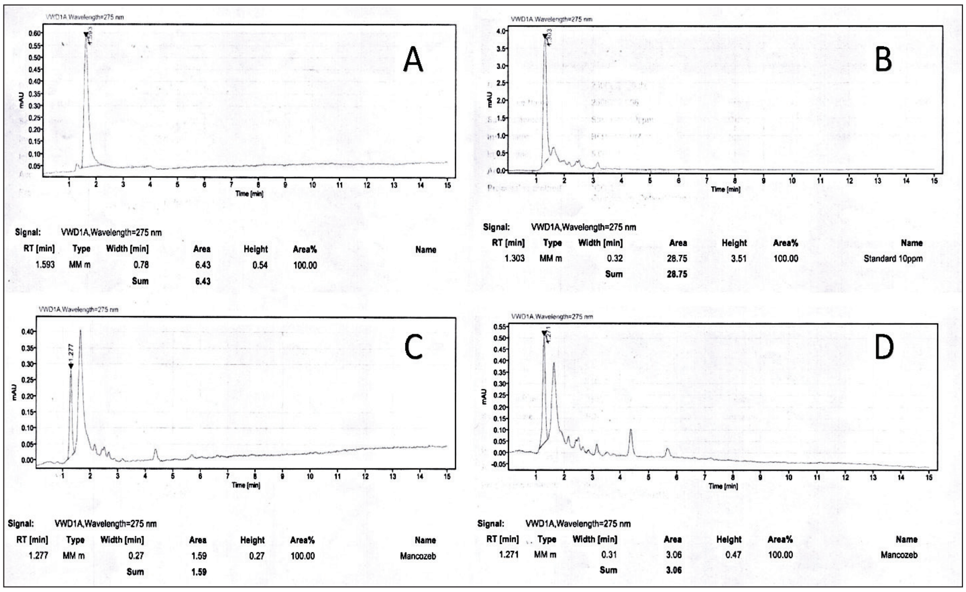

Signal: VWD1A,Wavelength=275 nm

RT [min]	Type	Width [min]	Area	Height	Area%	Name
1.593	MM m	0.78	6.43	0.54	100.00	
		Sum	6.43			

Signal: VWD1A,Wavelength=275 nm

RT [min]	Type	Width [min]	Area	Height	Area%	Name
1.303	MM m	0.32	28.75	3.51	100.00	Standard 10ppm
		Sum	28.75			

Signal: VWD1A,Wavelength=275 nm

RT [min]	Type	Width [min]	Area	Height	Area%	Name
1.277	MM m	0.27	1.59	0.27	100.00	Mancozeb
		Sum	1.59			

Signal: VWD1A,Wavelength=275 nm

RT [min]	Type	Width [min]	Area	Height	Area%	Name
1.271	MM m	0.31	3.06	0.47	100.00	Mancozeb
		Sum	3.06			

Fig. 7. HPLC curves showing; A) blank, B) 10 mg L^{-1} standard, C) SC-2, and D) SD-2

The data were processed by Agilent 2D- LC-solution software. Determination of mancozeb concentration was performed using a mobile phase at a flow rate of 1.0 mL min^{-1}. Ten microliters of the sample were injected, and it was detected at 275 nm under 25 °C. Figure 7 below revealed the HPLC curves of the analysis with the retention time, area, width, and height for each curve. As can be observed from caption B of the figure, the area of 10 mg L^{-1} standards was revealed to be 28.75 whereas, captions C and D show that of SC-2 and SD-2 to be 1.59 and 3.06 respectively. The final concentration at optimum conditions was determined from the HPLC curves.

Also, Table 2 and Figure 8, it can be observed that the effect of the nanoparticles on the degradation of (MCZ) pesticides differs at various concentrations of the pesticides and the amount of zinc oxide nanoparticles used. This is a result of numerous factors which include the initial concentration of the pesticide, the dosage of the photocatalyst, irradiation time and other factors. However, the findings revealed that increasing the dosage of the photocatalyst has shown a greater degradation efficiency. Due to Figure 8, it can be observed that SB-2, SC-2, and SD-2 with a 10 mg dosage of the photocatalyst have shown greater efficiency than their counterparts with the same initial pesticide concentration. Research indicates that elevating the catalyst quantity leads to increased pesticide degradation in the solution, reaching a point where degradation plateaus and/or diminishes, likely attributed to reduced light penetration [RS5] residential, and commercial applications. The release of chlorpyrifos into water and wastewater sources may affect human health because of its chronic toxicity to aquatic organisms. Therefore, its degradation seems necessary. The present study aimed to investigate the photocatalytic efficiency of biochar nanocomposite based on grapefruit skin modified with Fe3O4 and CdS nanoparticles (biochar/CdS-Fe3O4. The initial concentration of the pesticide was also found to affect the degradation efficiency. SC-2 with 9.37 mg L^{-1} pesticides has shown better efficiency than SA and SB samples with lower concentrations and SD samples with higher concentrations. Light penetration is crucial for photocatalysis and increasing pesticide concentration may diminish light penetration and hence the photocatalytic activity. Therefore, the gradual increase in efficiency from SA to SC may be a result of other factors whereas, the decreasing efficiency observed in SD samples may be attributed to lower light penetration. The best degradation efficiency was achieved when 10 mg of NPs dose was applied to 9.37 mg L^{-1} of the (MCZ) solution for an hour.

The degradation efficiency of the pesticide using the synthesized photocataly were presented in Figure 9 and Table 3. The percentage degradation/degradation efficiency as computed is presented in the figure. It can be observed that at optimum conditions, SC-2 was found to possess the highest efficiency followed by SD-2 and SB-2. Moreover, SB-1 with 4 mg L^{-1} initial pesticide concentration and 5.0 mg dosage of the photocatalyst was revealed to possess lower degradation efficiency. The reusability and recoverability of the sample (NPs) were studied after 7 rounds of experiments under optimum conditions. It was revealed that, at optimum conditions, the (NPs) were shown to be active and efficient up to 3 rounds of the degradation experiment which later on began to slightly decline.

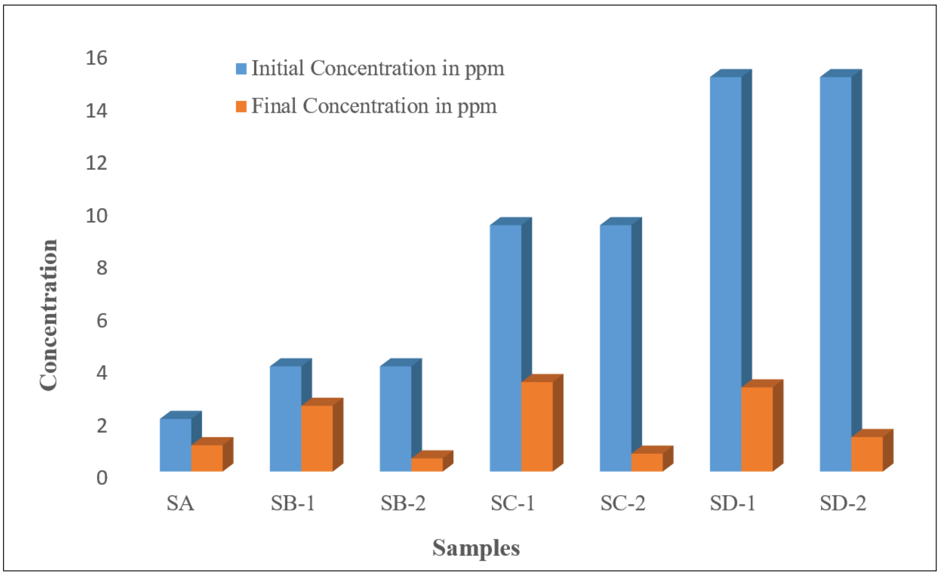

Fig. 8. The initial and final concentrations of MCZ pesticide degradation

Table 2. Initial and final concentrations of mancozeb fungicide as detected by HPLC analysis at an optimal time condition

Sample Code	Amount of NPs	Initial Concentration before degradation	Final Concentration after degradation	Degradation efficiency
SA	10 mg	2.0 mg L^{-1}	1.0 mg L^{-1}	50%
SB2	5 mg	4.0 mg L^{-1}	2.5 mg L^{-1}	44.4%
SB2	10 mg	4.0 mg L^{-1}	0.5 mg L^{-1}	88.8%
SC1	5 mg	9.4 mg L^{-1}	3.4 mg L^{-1}	63.71%
SC2	10 mg	9.4 mg L^{-1}	0.68 mg L^{-1}	92.70%
SD1	5 mg	15.0 mg L^{-1}	3.2 mg L^{-1}	78.66%
SD2	10 mg	15.0 mg L^{-1}	1.31 mg L^{-1}	91.2%

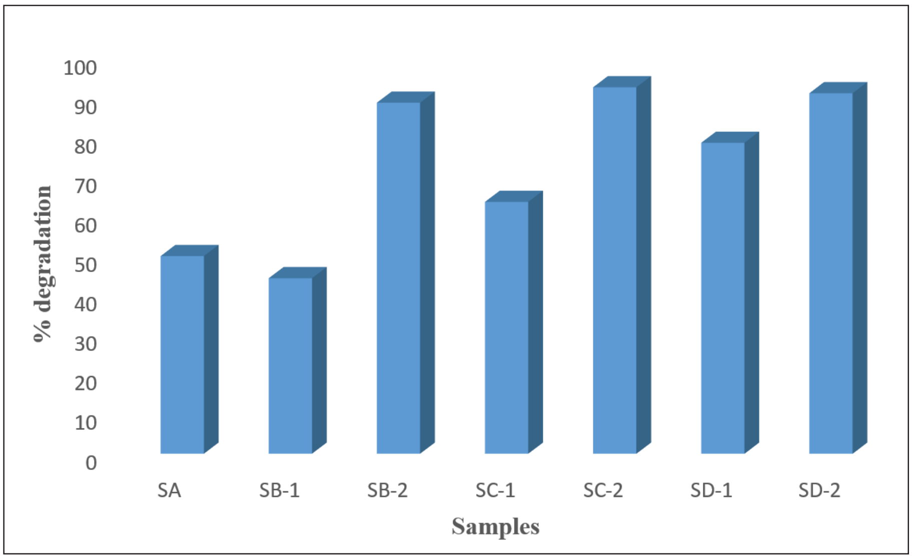

Fig. 9. Degradation efficiency at various experimental conditions for the removal of MCZ

Table 3. Comparison between the current method and the reported electrochemical method in the literature

S/N	Method	degradation %	Source
1	Photocatalytic degradation using NPs	.92%	Current work
2	The electrochemical method under UV	67%	[RS6]

4. Conclusions

In this study, a suitable method was established for the photocatalytic degradation of (MCZ) in wastewater and agricultural runoff using Zinc Oxide Nanoparticles. The (XRD) pattern and (SEM) studies have shown that zinc oxide nanoparticles are Rhombohedral in structure. The (EDAX) spectra confirmed the presence of zinc element and showed that the synthesized zinc oxide nanoparticles were pure. Different amounts of (NPs) were loaded into a preconcentrated (MCZ) fungicide solution of different concentrations. HPLC and UV analysis were used to determine the degradation efficiency of the synthesized particles. The particle size distribution of the synthesized zinc oxide NPs was found to be in the range of 50-95 nm. At optimum conditions of 10 mg NPs dosage, 9.37 mg L^{-1} concentration of (MCZ) fungicide, and 60 minutes, the degradation efficiency was revealed to be above 92%. Moreover, the (NPs) were shown to possess great recoverability and reusability with efficient activity up to 3 rounds. It is crucial and significant to keep on exploring the intrinsic capabilities of abundant metal oxides like zinc oxide nanoparticles for environmental remediation and other applications.

5. Acknowledgement

The authors sincerely thank the School of Science, GITAM (deemed to be a University) for giving support and facilities for completing the research work

6. References

[1] R. Garg, R. Gupta, N. Singh, A. Bansal, Eliminating pesticide quinalphos from surface waters using synthesized GO-ZnO nanoflowers: Characterization, degradation pathways and kinetic study, Chemosphere, 286 (2022) 131837. https://doi.org/10.1016/J.CHEMOSPHERE.2021.131837.

[2] C. M. Martínez-Escudero, I. Garrido, P. Flores, P. Hellín, F. Contreras-López, J. Fenoll, Remediation of triazole, anilinopyrimidine,

strobilurin and neonicotinoid pesticides in polluted soil using ozonation and solarization, J. Environ. Manage., 310 (2022) 114781.https://doi.org/10.1016/J.JENVMAN.2022.114781.

[3] F. Hüesker, R. Lepenies, Why does pesticide pollution in water persist?, Environ. Sci. Policy, 128 (2022)185–193. https://doi.org/10.1016/J.ENVSCI.2021.11.016.

[4] A. Alsendi, A. A. Kareem, M. Havasi, G. Golmohammadi, A study on the toxicity and sublethal concentrations of three insecticides on the population dynamics of green lacewing chrysoperla carnea stephens, Arab J. Plant Prot., 41 (2023) 28-36. https://doi.org/10.22268/AJPP-41.1.028036.

[5] E. Gök, E. Deveci, Histopathological, immunohistochemical and biochemical alterations in liver tissue after fungicide-mancozeb exposures in Wistar albino rats, Acta Cirúrgica Bras., 37 (2022) e370404. https://doi.org/10.1590/ACB370404.

[6] S. Kumar, T. R. Baggi, T. Al-Zughaibi, Forensic toxicological and analytical aspects of carbamate poisoning-A review, J. Forensic Leg. Med., 92 (2022)102450. https://doi.org/10.1016/J.JFLM.2022.102450.

[7] Y. Bai, X. Ruan, J. P. van der Hoek, Residues of organochlorine pesticides (OCPs) in aquatic environment and risk assessment along Shaying River, China, Environ. Geochem. Health, 40 (2018) 2525–2538. https://doi.org/10.1007/S10653-018-0117-9/TABLES/5.

[8] J. S. Aprioku, B. Pharm, A. M. Amamina, A. Nnabuenyi, Mancozeb-induced hepatotoxicity: protective role of curcumin in rat animal model, Toxicol. Res. (Camb), 12 (2023) 107–116. https://doi.org/10.1093/TOXRES/TFAC085.

[9] O. J. Stephenson, L. D. Trombetta, Comparative effects of Mancozeb and Disulfiram-induced striated muscle myopathies in Long-Evans rats, Environ. Toxicol. Pharmacol., 74, (2020) 103300. https://doi.org/10.1016/J.ETAP.2019.103300.

[10] F. Bano, B. Mohanty, Thyroid disrupting pesticides mancozeb and fipronil in mixture caused oxidative damage and genotoxicity in lymphoid organs of mice, Environ. Toxicol. Pharmacol., 79 (2020)103408. https://doi.org/10.1016/J.ETAP.2020.103408.

[11] B. R. Kistinger, D. Hardej, The ethylene bisdithiocarbamate fungicides mancozeb and nabam alter essential metal levels in liver and kidney and glutathione enzyme activity in liver of Sprague-Dawley rats, Environ. Toxicol. Pharmacol., 92 (2022) 103849. https://doi.org/10.1016/J.ETAP.2022.103849.

[12] N. Atmaca, Effects of mancozeb, metalaxyl and tebuconazole on steroid production by bovine luteal cells in vitro, Environ. Toxicol. Pharmacol., 59 (2018) 114–118. https://doi.org/10.1016/J.ETAP.2018.03.009.

[13] J. Bao, Y. Zhang, R. Wen, L. Zhang, X. Wang, Low level of mancozeb exposure affects ovary in mice, Ecotoxicol. Environ. Saf., 239 (2022)113670. https://doi.org/10.1016/J.ECOENV.2022.113670.

[14] Y. Morales-Ovalles, Developmental exposure to mancozeb induced neurochemical and morphological alterations in adult male mouse hypothalamus, Environ. Toxicol. Pharmacol., 64 (2018)139–146. https://doi.org/10.1016/J.ETAP.2018.10.004.

[15] M. A. Saraiva, Mancozeb impairs mitochondrial and bioenergetic activity in Drosophila melanogaster, Heliyon, 7 (2021) e06007. https://doi.org/10.1016/J.HELIYON.2021.E06007.

[16] E. E. Elsharkawy, M. A. El-Nasser, A. A. Bakheet, Mancozeb impaired male fertility in rabbits with trials of glutathione detoxification, Regul. Toxicol. Pharmacol., 105 (2019) 86–98. https://doi.org/10.1016/J.YRTPH.2019.04.012.

[17] A. Harrison Brody, E. Chou, J. M. Gray, N. J. Pokyrwka, K. M. Raley-Susman, Mancozeb-induced behavioral deficits precede structural neural degeneration, Neurotoxicol., 34 (2013) 74–81. https://doi.org/10.1016/J.

NEURO.2012.10.007.

[18] S. H. Gebre, M. G. Sendeku, New frontiers in the biosynthesis of metal oxide nanoparticles and their environmental applications: an overview, SN Appl. Sci., 1 (2019) 1–28. https://doi.org/10.1007/S42452-019-0931-4

[19] E. Hannachi, Synthesis, characterization, and evaluation of the photocatalytic properties of zinc oxide co-doped with lanthanides elements, J. Phys. Chem. Solids, 170 (2022) 110910. https://doi.org/10.1016/J.JPCS.2022.110910.

[20] P. Akhter, Efficient visible light assisted photocatalysis using ZnO/TiO2 nanocomposites, Mol. Catal., 535 (2023) 112896. https://doi.org/10.1016/J.MCAT.2022.112896.

[21] R. M. Abdelhameed, O. M. Darwesh, M. El-Shahat, Titanium-based metal-organic framework capsulated with magnetic nanoparticles: Antimicrobial and photocatalytic degradation of pesticides, Micropor. Mesopor. Mater., 354 (2023)112543.b https://doi.org/10.1016/J.MICROMESO.2023.112543.

[22] L. Zhang, Silicon quantum dots and MOFs hybrid multicolor fluorescent nanosensor for ultrasensitive and visual intelligent sensing of tetracycline, Coll. Surf. A Physicochem. Eng. Asp., 652 (2022) 129853. https://doi.org/10.1016/J.COLSURFA.2022.129853.

[23] M. Samadifar, Y. Yamini, M. M. Khataei, Magnetically solid-phase extraction of diazinon and chlorpyrifos pesticides in vegetables using covalent triazine-based framework incorporated chitosan nanocomposite, J. Food Compos. Anal., 118 (2023) 105158. https://doi.org/10.1016/J.JFCA.2023.105158.

[24] S. Amiri, M. Anbia, Enhanced degradation of diazinon in aqueous solution using C-TiO2/g-C3N4 nanocomposite under visible light: Synthesis, characterization, kinetics, and mechanism studies, Mater. Res. Bull., 16 5(2023)112289. https://doi.org/10.1016/J.materresbull.2023.112289.

[25] M. Arjomandi, H. Shirkhanloo, A Review: Analytical methods for heavy metals determination in environment and human samples, Anal. Methods Environ. Chem. J., 2 (2019) 97–126. https://doi.org/10.24200/amecj.v2.i03.73.

[26] S. Golkhah, H. Zavvar Mousavi, Removal of Pb (II) and Cu (II) Ions from aqueous solutions by cadmium sulfide Nanoparticles, Int. J. Nanosci. Nanotechnol. 13 (2017) 105-117. https://www.ijnnonline.net/article_25609.html

[27] A. Ali, S. Ahmed, Green Synthesis of Metal, Metal Oxide Nanoparticles, and Their Various Applications, Springer Book, pages 1-45, 2018. https://doi.org/10.1007/978-3-319-48281-1_115-1.

[28] M. M. Asl, N. Mansouri, S. A. R. H. S. Mirzahosseini, F. Atabi, Functionalized graphene oxide with bismuth and titanium oxide nanoparticles for efficiently removing formaldehyde from the air by photocatalytic degradation–adsorption process, J. Anal. Test., (2023) 1–15. https://doi.org/10.1007/s41664-023-00272-0

[29] A. Faghihi-Zarandi, J. Rakhtshah, B. Bahrami Yarahmadi, A rapid removal of xylene vapor from environmental air based on bismuth oxide coupled to heterogeneous graphene/ graphene oxide by UV photo-catalectic degradation-adsorption procedure, J. Environ. Chem. Eng., 8 (2020)104193. https://doi.org/10.1016/j.jece.2020.104193

[30] R. R. Wary, S. Baglari, D. Brahma, U. K. Gautam, P. Kalita, M. B. Baruah, Synthesis, characterization, and photocatalytic activity of ZnO nanoparticles using water extract of waste coconut husk, Environ. Sci. Pollut. Res., 29 (2022) 42837–42848. https://doi.org/10.1007/s11356-022-18832-9

[31] A. M. Tatagar, J. I. Moodi, J. C. Abbar, M. A. Phaniband, Photocatalytic activity and anti-microbial application of synthesized Zinc oxide nanoparticles (ZnO Nps) towards

remediation of hospital waste water (HWW), Mater. Today Proc., 49 (2022) 699–702. https://doi.org/10.1016/j.matpr.2021.05.176

[32] V. N. Rao, N. V. S. Venu Gopal, T. B. Patrudu, Zinc oxide nanoparticles catalytic activity for the degradation of quinclorac herbicide residues in water, Bull. Monum., 21(2020)161. http://bulletinmonumental.com/

[33] Y. Li, K. Li, M. Li, M. Ge, Zinc-doped ferrite nanoparticles as magnetic recyclable catalysts for scale-up glycolysis of poly(ethylene terephthalate) wastes, Adv. Powder Technol., 33 (2022)103444. https://doi.org/10.1016/J.APT.2022.103444.

[34] B. Sowjanya, U. Sirisha, A. Suhasini Juttuka, S. Matla, P. King, M. Vangalapati, Synthesis and characterization of zinc oxide nanoparticles: It's application for the removal of alizarin red S dye, Mater. Today Proc., 62 (2022) 3968-3972. https://doi.org/10.1016/j.matpr.2022.04.576

[35] S. Rajendrachari, P. Taslimi, A. C. Karaoglanli, O. Uzun, E. Alp, G. K. Jayaprakash, Photocatalytic degradation of Rhodamine B (RhB) dye in waste water and enzymatic inhibition study using cauliflower shaped ZnO nanoparticles synthesized by a novel One-pot green synthesis method, Arab. J. Chem., 14 (2021)103180. https://doi.org/10.1016/J.ARABJC.2021.103180.

[36] E. Alizadeh, H. Baseri, Catalytic degradation of Amlodipine Besylate using ZnO, Cu doped ZnO, and Fe doped ZnO nanoparticles from an aqueous solution: Investigating the effect of different parameters on degradation efficiency, Solid State Sci., 78 (2018) 86–94. https://doi.org/10.1016/j.solidstatesciences.2018.02.010

[37] K. Rambabu, G. Bharath, F. Banat, P. L. Show, Green synthesis of zinc oxide nanoparticles using Phoenix dactylifera waste as bioreductant for effective dye degradation and antibacterial performance in wastewater treatment, J. Hazard. Mater., 402 (2021) 123560. https://doi.org/10.1016/j.jhazmat.2020.123560.

[38] P. Nagaraju, Y. Vijayakumar, M. V. Ramana Reddy, Room-temperature BTEX sensing characterization of nanostructured ZnO thin films, J. Asian Ceram. Soc., 7 (2019) 141–146. https://doi.org/10.1080/21870764.2019.1579401.

[39] J. Al-Sabahi, T. Bora, M. Al-Abri, J. Dutta, Efficient visible light photocatalysis of benzene, toluene, ethylbenzene and xylene (BTEX) in aqueous solutions using supported zinc oxide nanorods, PLOS One, 12 (2017) e0189276. https://doi.org/10.1371/journal.pone.0189276

[40] S. M. Nampoothiri, V. Chandran, E. M. Mohammed, R. Francis, Preparation and Characterization of Zinc Oxide(ZnO) Nanoparticles via Co-precipitation Method, Int. J. Sci. Res. Pap. Multidiscip. Stud., 5 (2019) 56−61. https://www.isroset.org/pdf_paper_view.php?paper_id=1447&8-IJSRMS-02507.pdf

Note: RS1-RS6 showed in Supplementary Material (ESM)